Photoluminescence Spectroscopy of $Si_{1-x}Ge_x$/Si Heterostructures

by

Lori Lenchyshyn

M.Sc. Simon Fraser University, 1990

B.Sc. University of Waterloo, 1987

Thesis Submitted in Partial Fulfillment of
the Requirements for the Degree of
DOCTOR OF PHILOSOPHY
in the Department of Physics

© Lori C. Lenchyshyn 1993
Simon Fraser University
September 1993

APPROVAL

Name: Lori Lenchyshyn

Degree: Doctor of Philosophy

Thesis Title: Photoluminescence Spectroscopy of $Si_{1-x}Ge_x$/Si Heterostructures

Examining Committee:

Chairman: Dr. E.D. Crozier

Dr. M.L.W. Thewalt
Senior Supervisor

Dr. D. Boal

Dr. J.C. Irwin

Dr. R.F. Frindt

Dr. S. Watkins

Dr. M. Tajima
External Examiner
Institute of Space and Astronautical Science
Sagamihara 229, Japan

Date Approved : September 17, 1993

Title of Thesis/Project/Extended Essay

Photoluminescence Spectroscopy of

$Si_{1-x}Ge_x / Si$ Heterostructures

Author:

(signature)

Lori Lenchyshyn

(name)

Sept 24 /93

(date)

ABSTRACT

The $Si_{1-x}Ge_x$/Si materials system has recently become the subject of intense research because of the potential for applications in Si based electronic and optoelectronic devices. This thesis describes the results of optical characterization of $Si_{1-x}Ge_x$/Si heterostructures obtained by photoluminescence spectroscopy. The focus is on well-resolved band edge photoluminescence from fully strained $Si_{1-x}Ge_x$ layers, which can be attributed to shallow bound excitons at low temperatures or to free excitons above ~10 K. At low excitation density (~ 100 μW cm^{-2}) the bound exciton luminescence decreases in intensity to reveal a highly efficient (external quantum efficiency >10 %) luminescence process, that is a direct consequence of the alloy nature of the $Si_{1-x}Ge_x$. The characteristics of this new photoluminescence band are shown to be consistent with the recombination of excitons localized by the random fluctuations in Ge content in different regions of the $Si_{1-x}Ge_x$.

For thin $Si_{1-x}Ge_x$ layers, quantum well structures are formed and the bound exciton luminescence shifts to higher energy due to the exciton confinement. Good agreement with the predicted confinement energies is obtained for a series of single $Si_{0.8}Ge_{0.2}$ quantum wells with well thicknesses of 83 to 33 Å. The localized exciton process is also observed to be modified since the confinement to the thin quantum well layers limits the excitons to the more abundant shallow alloy localization centers.

By utilizing the bound exciton photoluminescence spectra from more complicated quantum well structures, other aspects of the $Si_{1-x}Ge_x$/Si system can also be studied. The bound exciton recombination energy from stepped quantum well structures provides evidence suggesting type I band alignment for $Si_{1-x}Ge_x$/Si heterojunctions with x $\leq$ 0.35. The luminescence is also used as a signature to indicate tunneling from one $Si_{1-x}Ge_x$ quantum well into another deeper well, through a thin ($\leq$ 90 Å) Si barrier.

ACKNOWLEDGEMENTS

TABLE OF CONTENTS

LIST OF FIGURES

LIST OF TABLES

ABBREVIATIONS

BE   bound exciton

BMEC   bound multi-exciton complex

CDQW   coupled double quantum well

CVD   chemical vapour deposition

FE   free exciton

FWHM   full width half maximum

LA   longitudinal acoustic

LE   localized exciton

LO   longitudinal optic

MBE   molecular beam epitaxy

MQW   multiple quantum well

NP   no-phonon

OPO   optical parametric oscillator

PL   photoluminescence

PLE   photoluminescence excitation spectroscopy

QW   quantum well

RTCVD   rapid thermal chemical vapour deposition

SiGe $Si_{1-x}Ge_x$

SQW   single quantum well

STQW   stepped quantum well

TA   transverse acoustic

TO   transverse optic

Chapter 1.

Introduction to $Si_{1-x}Ge_x$ on Si

1.1. Motivation for this Study

Silicon (Si) is the most important semiconductor material in the electronics industry. While the development of compound semiconductors, made up of elements from Groups II, III, V, and/or VI of the periodic table, has undoubtedly expanded the range of possibilities for devices, as yet Si is still more cost effective for most applications. The low cost of Si devices is due primarily to the simplicity of the Si crystal growth compared to that of the compounds. Elaborate growth techniques are needed for the compound semiconductors because of the different vapour pressures of the constituent materials and in order to control the stoichiometry (see for example Howes and Morgan [85H]). This makes the price of a device grade wafer of the most commonly used compound semiconductor, gallium arsenide (GaAs), over 25 times that of a Si wafer [88L]. Further complications with compound semiconductors arise during device processing due to the material brittleness and the difficulty in growing insulating layers. As well, ion implanation must be used in place of diffusion techniques because of the relatively high temperatures required to drive in dopants. The other common elemental semiconductor, germanium (Ge), is also relatively economical, however it has largely been ignored because its small

1

band gap (0.67 eV in Ge, 1.12 eV in Si) restricts it to devices operating at low temperatures. However, by combining Si and Ge in an alloy and/or layered structures we can create a new materials system with new properties and possible applications. Since it is generally accepted that the prohibitively high cost of GaAs device fabrication will always restrict it to specialized applications, the hope is that these new Si based materials can address some of the physical limitations inherent to the Si technology.

One of these limitations is speed. The greater speed in GaAs devices arises from a smaller electron effective mass and consequently a peak average electron velocity several times higher than in Si. Since the peak speed is achieved at lower applied electric fields, GaAs devices operate with less power. The larger GaAs band gap (1.42 eV) also allows for operation at higher temperatures because of reduced thermal generation of carriers, although this is limited somewhat by the relatively low thermal conductivity. These properties are intrinsic to the material itself, being manifestations of the GaAs band structure, and as such cannot be rivaled by Si simply by adding Ge atoms to the lattice. However, what we can do is try to improve the Si device speed by adopting some of the heterostructure techniques that have been used extensively in the GaAs system.

The ability to grow perfect crystal structures made up of different semiconductor materials (i.e. heterostructures) is one of the most powerful features of GaAs technology. Great improvements in the performance of bipolar transistors, field effect transistors, laser diodes, detectors, etc. have been realized through the use of heterostructures. GaAs has lent itself more easily than Si to such devices because a whole family of semiconductors made up of III-V compounds are available, including alloys such as $GaAs_{1-x}P_x$ and $Ga_{1-x}Al_xAs$. GaAlAs/GaAs has been most extensively utilized since significant changes can be made in the band gap by varying the Al content, with little effect on the lattice constant. The large (4 %) lattice mismatch between Si and Ge on the other hand makes the crystal growth more challenging. Despite this difficulty, bipolar transistors using $Si_{1-x}Ge_x$ bases have been fabricated that have nearly twice the speed of conventional Si

devices [90P]. As well, low temperature electron mobilities have been increased by two orders of magnitude (to 1.7×10^5 cm^2/Vs, [92Sc]) and hole mobilities by an order of magnitude (to 3640 cm^2/Vs, [92Sd]) by using modulation doping in $Si_{1-x}Ge_x$/Si structures.

Another disadvantage of Si is the inability to fabricate optoelectronic devices. This arises because it has an indirect band gap, so that absorption and emission processes must involve the participation of momentum conserving phonons to account for the difference in wave-vector between the band-edge holes and electrons. Such processes are inherently less efficient than in direct gap materials such as GaAs. The present Si optoelectronic technology is in fact based on GaAs/Si hybrids. Theoretical predictions [74G, 88S] of a direct band gap in Si/Ge superlattices has therefore prompted much of the research in this area. In addition to the fundamental problem of low optical efficiency, the integration of optical and electronic devices has been hampered by the lack of good quality Si based epitaxy. However, recent reports of strained $Si_{1-x}Ge_x$ alloys on Si have shown an improvement in the optical properties of this materials system. In fact, $Si_{1-x}Ge_x$/Si superlattices have recently been used to make discrete photodiodes with sensitivity at wavelengths (1.3 μm) compatible with modern fiber-optic communications [86Ta].

While many exciting advances have been made in the past few years, the full potential of this new Si-based technology has not yet been realized in practise. The intent of this study is therefore to better understand the underlying physics of these structures. Experimental results of optical characterization by photoluminescence spectroscopy are reported here for strained $Si_{1-x}Ge_x$ alloy layers grown on <100> Si substrates.

This chapter continues with an introduction to strained $Si_{1-x}Ge_x$ on Si and semiconductor heterostructures, while Chapters 2 and 3 set the groundwork for understanding the photoluminescence experiments. The results begin in Chapter 4, with an investigation of the photoluminescence features characteristic of a simple strained $Si_{1-x}Ge_x$ layer. As the $Si_{1-x}Ge_x$ layer thickness is decreased the abrupt change in

3

potential at the interface with the Si plays an increasingly important role. Chapter 5 explores the consequences of the differing band structures of the $Si_{1-x}Ge_x$ and the Si substrate on the photoluminescence spectra.

1.2. Band Gap of Strained $Si_{1-x}Ge_x$

Si and Ge are indirect gap materials, with band structures as shown in Figure 1.1. In Si there are six equivalent conduction band minima located along the <100> directions in reciprocal lattice space, about 85% of the way to the first Brillouin zone boundary (conventionally labelled X). The constant energy surfaces at these valleys are ellipsoids oriented along the <100> directions, with longitudinal and transverse electron effective masses of $m_L \sim 1.0\ m_0$ and $m_T \sim 0.2\ m_0$, respectively, where m_0 is the free electron mass. In Ge the conduction band minima lie at the zone boundary in the <111> directions (i.e. at the L point in reciprocal lattice space). The constant energy surfaces are composed of eight half ellipsoids, or translating four of these half ellipsoids by a reciprocal lattice vector we get four full ellipsoids. These ellipsoids are oriented along the <111> directions and with electron effective masses of $m_L \sim 1.6\ m_0$ and $m_T \sim 0.08\ m_0$. Both materials have degenerate valence band maxima at the Brillouin zone center (Γ point) which are approximately spherically symmetric. The band having lesser curvature is referred to as the heavy hole band ($m_{hh} \sim 0.49\ m_0$ in Si, 0.28 m_0 in Ge) and the other as the light hole band ($m_{lh} \sim 0.16\ m_0$ in Si, 0.044 m_0 in Ge).

A third valence band lying to lower energy is split from the other two by the spin-orbit coupling and is known as the split-off band. Spin-orbit coupling arises from the interaction of the electron spin with the atomic nucleus through the magnetic moment of the electron in its orbit. It is proportional to the spin magnetic moment and to the magnetic field felt by the electron due to its relative motion in the electric field of the

Germanium

Silicon

indirect gap 0.67 eV

Γ_6

direct gap 0.80 eV

Γ_8

Δ_0

heavy

light

split-off Γ_7

L Γ X

[111] k= [000] [100]

direct gap 2.5 eV

indirect gap 1.12 eV

heavy

Δ_0

light split-off

L Γ X

[111] k= [000] [100]

[111]

[$\bar{1}\bar{1}\bar{1}$]

Brillouin Zone

[001]

[0$\bar{1}$0]
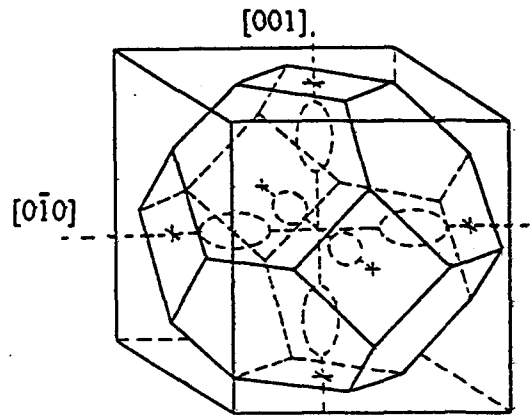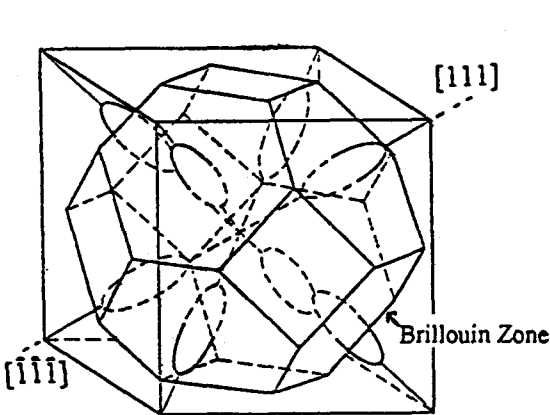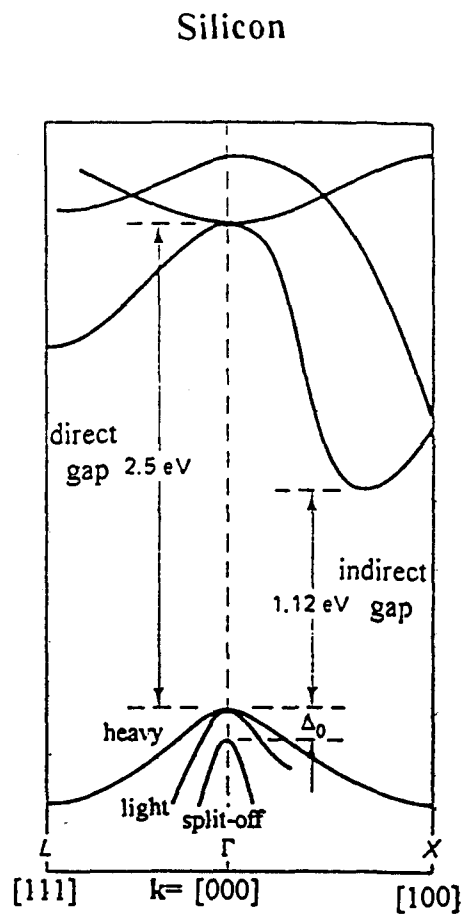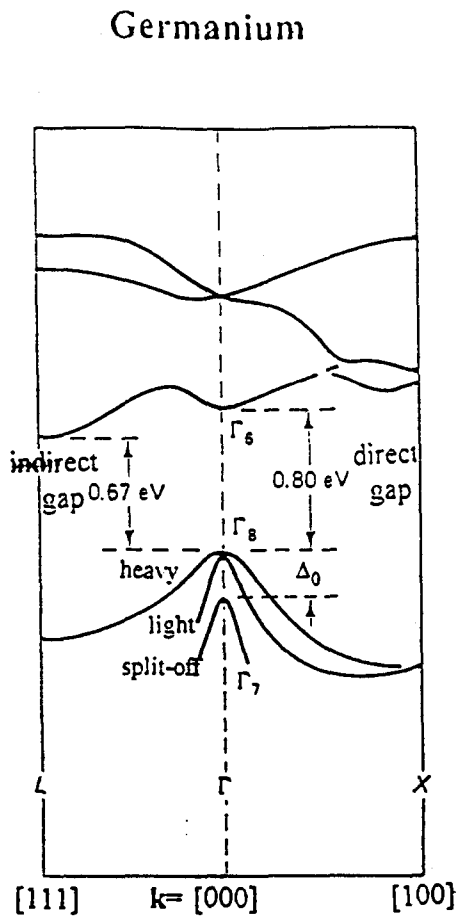
Figure 1.1 Energy bands (top) and constant energy surfaces near the conduction band minima (bottom) for Si and Ge. In Si there are six degenerate conduction band minima, which are in the [100] directions in k-space. In Ge the conduction band is four-fold degenerate with minima in the [111] directions. In both materials, the valence band maxima are located at the zone center with heavy hole, light hole and split-off bands as indicated. Both materials are indirect gap semiconductors.

nucleus (i.e. **v** x ∇U, where ∇U is the electric field). The name "spin-orbit coupling" is used because the energy of the electron is affected by the combination of its spin magnetic moment and its orbital motion. The spin-orbit splitting is larger for Ge (i.e. Δ_0 = 0.29 eV) than for Si (i.e. Δ_0 = 0.04 eV), where Δ_0 is the difference in energy between the maximum of the split-off band and the heavy/light hole valence band maxima.

In both the Si and Ge lattices each atom bonds covalently to four neighbouring atoms forming a regular tetrahedron or a diamond crystal structure. The $Si_{1-x}Ge_x$ alloy consists simply of Ge atoms randomly distributed throughout the lattice on Si sites to form a continuous series of disordered alloys from Ge fraction x=0 to 1. Although SiGe (for brevity the alloy fractions, 1-x and x, have been dropped) lacks the perfect translational symmetry of pure Ge or Si crystals, many of its properties can still be understood by applying band structure concepts, with the compositonal disorder treated as a perturbation. The result of the alloying is a dependence of the band energies on composition and a smearing of the band edges due to the random variation in the crystal potential [78B, 69A]. Part of the smearing of the band edges is manifested in a density of states tail which extends into the forbidden gap and can give rise to localized electronic states. Such localized states are the subject of sections 4.3 and 5.3. The SiGe band gap varies roughly linearly with Ge fraction, except for an abrupt changeover from Si-like to Ge-like band structure at x = 0.85. The changeover corresponds to the Ge fraction for which the L conduction band minima, discussed above, fall below those near the X point in the Brillouin zone. Figure 1.2 shows the result of a comprehensive study [89Wb] which used photoluminescence spectroscopy to determine the bulk SiGe band gap as a function of Ge fraction. Note that as discussed in Chapter 2, such measurements yield the so-called "excitonic band gap", which is shifted to lower energy than the actual band gap by the free exciton binding energy (4 meV in Ge, 15 meV in Si).

The Ge lattice constant (a_0 = 5.657 Å) is about 4% larger than that of Si (a_0 = 5.431 Å), while for the relaxed alloy the lattice constant varies approximately linearly with
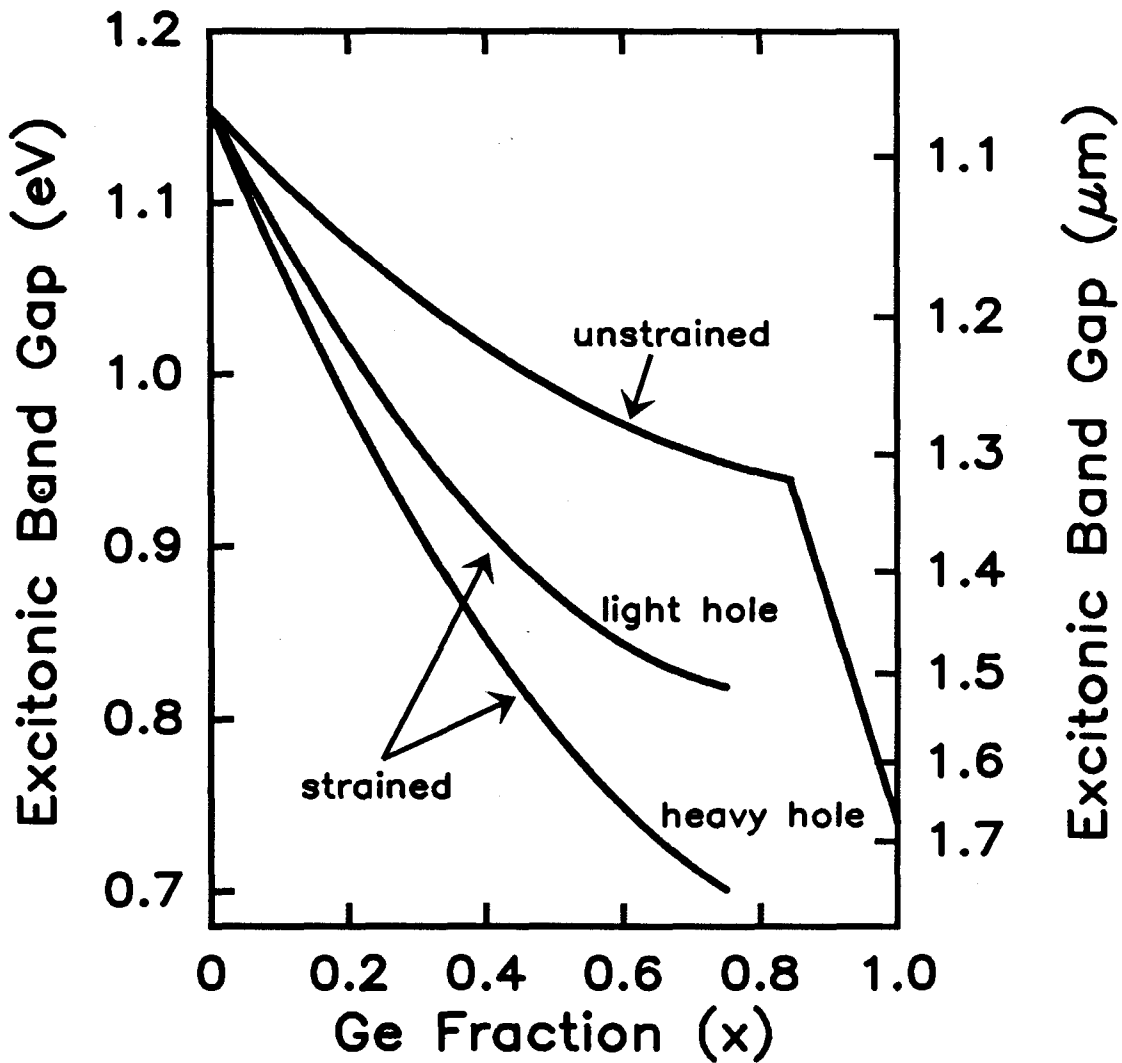
Figure 1.2 Excitonic band gap energy as a function of Ge fraction (x) for unstrained and strained $Si_{1-x}Ge_x$ at 4.2 K. The unstrained curve is the fit obtained by Weber and Alonso [89Wb] in their PL study. The strained curves were calculated using the deformation potential theory described by Lang *et al.* [85L]. The strain lifts the valence band degeneracy so that the smallest energy gap corresponds to the heavy hole band edge.

x between the pure Si and pure Ge values. This lattice mismatch introduces strain in the layers when growing them epitaxially on substrates of a different composition (i.e. Ge fraction). Epitaxial growth refers to the layer by layer deposition of one crystalline material on a similar one, preserving the in-plane crystal structure of the substrate. As described below, the substrate material is crucial in designing devices since it determines the strain, which ultimately affects the band structure of the epitaxial layers.

Above some x-dependent critical thickness, dislocations are introduced and the epitaxial layers relax to the lattice constant of the bulk alloy. Under certain growth conditions this critical thickness has been found to actually exceed that predicted by mechanical equilibrium by as much as an order of magnitude. This is thought to arise from a kinetic barrier to dislocation formation. Agreement between the theory and experiment can be obtained instead by an energy balance approach [85Pa]. Such films are therefore metastable, and can relax when annealed above the initial growth temperature. The ability to grow strained layers in excess of the equilibrium critical thickness is especially important in the Si/Ge system since the large lattice mismatch results in very small equilibrium critical thicknesses. For example the critical thickness of pure Ge on Si is only about 5 monolayers [89P]. In such cases, strain symmetrization is sometimes used to prevent the formation of dislocations. In this technique a thick, relaxed buffer layer of intermediate lattice constant (i.e. Ge fraction) is grown on the substrate before the Si/Ge device, so that the alternating epitaxial layers of the device take up opposing strains and the overall structure is stable to any thickness (see for example the review by Kasper and Schäffler [91K]).

This thesis describes experiments on strained Si rich ($x < 0.5$) SiGe alloys grown epitaxially on <100> Si substrates, and the discussion is henceforth limited to this regime. In this case the lattice mismatch is accommodated by the SiGe in a tetragonal distortion which consists of a biaxial compression in the plane of the SiGe/Si interface and a dilation in the growth direction. This is equivalent to a hydrostatic compression plus a uniaxial

8

dilation in the growth direction. The strain in the Si substrate is assumed to be zero since it is usually substantially thicker than the epitaxial SiGe layers. The effect of the strain on the SiGe band gap can be described approximately using a phenomenological approach known as deformation potential theory [85L]. The deformation potentials are empirically determined fitting parameters such that the strain Hamiltonian gives the correct dependence of the band gap and the band splittings on an externally applied uniaxial or hydrostatic stress. For SiGe a linear interpolation between the well known Si and Ge deformation potential values can be used. However in applying this theory to strain caused by lattice mismatch these values will be approximate, since nonlinear effects are expected from the much higher strain present in the heterostructure layers in comparison to typical stress experiments.

The band gap of the strained alloy can be broken down into contributions from four terms i) the unstrained SiGe band gap, ii) changes in the band gap due to compression (the hydrostatic terms), iii) uniaxial splittings of the conduction band edges, and iv) uniaxial splittings of the valence band edges. For Si rich alloys, the hydrostatic terms cause a small decrease in the indirect band gap energy. The uniaxial strain causes the four conduction band valleys in the growth plane to shift to lower energy, while the other two perpendicular valleys shift to higher electron energy. The conduction band minima are therefore fourfold degenerate in the strained alloy. The uniaxial strain also couples the heavy and light hole bands with the split-off band, causing the degeneracy of the light and heavy hole bands at the zone center to be lifted. The heavy hole band is pushed up into the gap so that it becomes the lowest (hole) energy valence band edge. This is shown in Figure 1.2, where the strained SiGe band gaps associated with the heavy and light hole valence band edges were calculated following the deformation potential calculations described above (Lang *et al.* [85L]) and using the bulk SiGe band gap values of Weber and Alonso [89Wb]. Note that the strain dramatically lowers the band gap, making it possible to attain the 1.3 μm range commonly used in communications, with a more dilute

alloy composition. Similar theoretical curves were calculated several years ago by Lang *et al.* [85L] and were found to agreed roughly with their photocurrent spectroscopy results. However the photocurrent spectroscopy technique depends on fitting the observed data, of absorption coefficient as a function of incident photon energy, to the expected energy dependence in order to extract the band gap (usually $\alpha \sim (E-E_g)^2$ is assumed). In Chapter 4 of this work the the strained alloy is studied using PL spectroscopy, which gives a more direct measure of the band gap energy.

1.3. Heterojunctions

In growing an epitaxial layer on a different semiconductor material, not only can we introduce strain which changes the epitaxial layer's band structure, but we also produce discontinuities in the conduction and/or valence bands at the interface. This is known as a heterojunction, with the band discontinuities usually depicted schematically in the growth direction (conventionally labelled the z direction) as in Figure 1.3. While the idea of making transistors and diodes using p-n junctions of two different materials originated in the 1950's, early attempts resulted in interfaces of high dislocation density (see for example the discussion by Wang [89Wc]). Interest was revived in the early 70's with Esaki's Nobel prize winning study of resonant tunneling [74E], as well as the successful fabrication of double heterostructure lasers. Since then sophisticated growth techniques such as molecular beam epitaxy and metal-organic chemical vapour deposition have been developed, which make it possible to control the growth of the layers on a monolayer scale. While such techniques have traditionally been the domain of only the III-V or II-VI semiconductor systems, recent advances have been made in epilayer growth in the SiGe/Si system.

Growth direction (z)

substrate   epitaxial layer

conduction
band Δ Ec

Type I Heterojunction

Δ Ev

valence
band

conduction
band Δ Ec

Type II Heterojunction

Δ Ev

valence
band
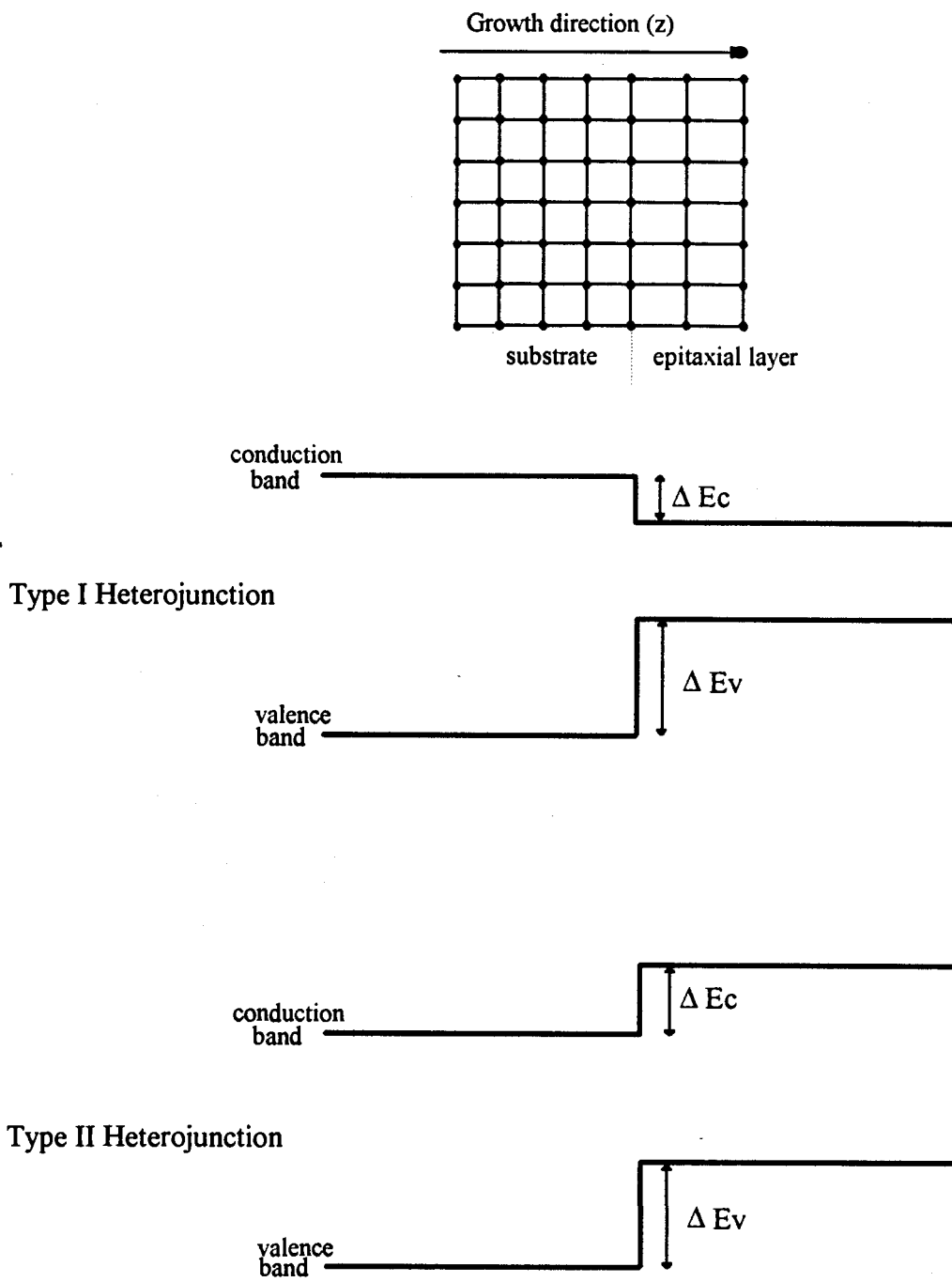
Figure 1.3 Schematic depiction of epitaxial growth (top) and band structure for

Type I (center) and Type II (bottom) heterojunctions.

11

The ability to make good heterojunction interfaces allows for many new degrees of freedom in device design. Most electronic device textbooks (see for example [89Wc, 81S]) discuss the advantages of modifying conventional devices, such as field effect transitors, bipolar transistors, light emitting diodes, lasers or detectors, to incorporate heterostructures. There has also been the invention of completely new devices, such as the resonant tunneling diode. In addition to the practical aspects of such research, many interesting avenues in the realm of quantum mechanics and materials physics have been pursued.

To design such heterostructure devices it is important to know not only the difference in band gap between the epitaxial layer and the substrate ($\Delta E_g = \Delta E_c + \Delta E_v$), but also the individual conduction (ΔE_c) and the valence band (ΔE_v) offsets. The terms type I and type II are traditionally used to describe the band offsets at the heterostructure interface. In a type I interface the conduction and valence band extrema of one material are nested inside the other as shown in Figure 1.3 (center). In type II heterostructures the band edges are staggered so that electrons favour one material while holes favour the other (Figure 1.3, bottom). This spatial separation of carriers has significant implications in how the heterostructure device functions.

While the measured band gap of strained SiGe on Si has been found to agree quite well with the theoretical curve shown in Figure 1.2 (see Lang *et al.* [85L] or section 4.2 of this work), the individual band discontinuities are not as clearly established. The deformation potential theory gives us information about the strain induced splittings of the bands and the overall shrinkage of the SiGe band gap with increasing x, however it cannot be used to determine the energies of the individual conduction and valence band edges in the SiGe relative to those in the Si. For example, the hydrostatic strain causes the indirect band gap to shrink, but how much of this shrinkage occurs due to the valence band and how much to the conduction band is not known. The difficulty lies in finding a common reference level for each semiconductor, even before forming the interface between them.

The best theoretical approach seems to be that of Van de Walle and Martin [86V], who used *ab initio* pseudopotentials to first determine the average Si and Ge potentials, which then serve as reference levels for band structure calculations. For strained SiGe on <100> Si, they found that most of the band offset occurs in the valence band. There is an approximately linear increase in the heavy hole band energy (i.e. a decrease in hole energy) with increasing Ge fraction up to an offset of 0.84 eV at x = 1. The conduction band discontinuity is slightly (< 50 meV) negative in the SiGe relative to the Si up to a Ge fraction of about 0.65, after which it increases to a positive offset of 0.28 eV at x=1. Unfortunately, there is a large uncertainty in these calculations (± 100 meV) which, because it exceeds the calculated conduction band offset for the Si rich alloys, prevents a prediction of type I or type II behaviour.

The problem is compounded by the notorious difficulty in confirming band discontinuities experimentally (see for example Wang [89Wc]). The first indication of a small (or positive) conduction band offset in SiGe/Si came from People and Bean [85Pb] since they were able to observe 2D hole gases but not 2D electron gases in SiGe/Si superlattice structures. Using X-ray photoelectron spectroscopy Ni *et al.* [87N] obtained a type I alignment with a conduction band offset of less than 30 meV for Si rich alloys, but again the uncertainty was high (60 meV). Nauka [92Nc] also found type I, with an offset of a few meV ± 10 meV, however the offsets were extracted in a rather indirect way from admittance measurements on transistor structures. Very recently, Morar *et al.* [93M] described an electron energy loss method which they claim has an error in the band offsets of ≤ 15 meV for x ≤ 0.3. Unfortunately, the technique requires examining the SiGe and Si samples separately so it can only treat the case of unstrained SiGe directly. The strained SiGe offsets must then be inferred using deformation potential theory. The problem of band offsets is examined further in Chapter 5, in a unique experiment which utilizes photoluminescence measurements of stepped quantum well structures designed by our collaborators J.C. Sturm and X. Xiao at Princeton University [93Sa].

1.4. Quantum Wells

Quantum wells are formed when a thin layer of one semiconductor material is sandwiched between two barrier layers. The band offsets at the two interfaces produce a potential well which confines the carriers, so that they occupy discrete energy levels rather than continuous bands (see Figure 1.4). Confining the carriers further in two or in all three directions leads to quantum wires and quantum dots, respectively. These structures are practical realizations of the standard 'particle in a box' problem of introductory quantum mechanics. In fact we can often get surprisingly good predictions of the energy levels using a simple square well approach.

The total wave function of a carrier confined in a single quantum well (SQW) is the product of the usual in-plane wave function of the bulk material (i.e. a Bloch function) and a wave function in the epi-layer growth direction. The wave function in the growth direction is traditionally found using the envelope function scheme (see Bastard and Brum [86B]). First we assume a solution of the form:

$$\psi(z) = \sum_j \phi(z) \, u_{j0} \qquad (1.1)$$

where $\phi(z)$ is a slowly varying envelope function and u_{j0} is the part of the jth zone center band-edge Bloch function describing the periodic potential of the bulk crystal. Because the materials making up the heterostructure usually have similar band structures, the differences in the u_{j0} of the barrier and the well are neglected. While this assumption leads, as discussed below, to some difficulty in treating the boundary conditions, it simplifies the overall problem considerably. With this approach all of the information about the heterostructure interface is contained in the envelope function.

Note that the form of the solution (eq. 1.1) is the same as that used in the effective mass theory conventionally applied to a perturbation in an otherwise perfect lattice, such as an impurity. The assumption of a weak perturbing potential, which is valid in the usual

14

applications of effective mass theory, is not actually appropriate to heterostructure potentials. Despite this apparent inconsistency, the envelope function scheme is adopted here since it has been found by many researchers to work quite well in practice. For further discussion on the validity of the envelope function technique see Burt [92B].

To find a solution for the quantum well eigenfunction we need to determine the appropriate form of the Hamiltonian that it must satisfy. We can do this by first writing the Hamiltonian on either side of the interface i.e. in the bulk semiconductors. The physically relevant electronic states lie close to the band extrema so to a first approximation we expect quadratic dispersion curves and the Hamiltonian can be written using the effective mass tensor. This is sometimes referred to as the $\mathbf{k} \cdot \mathbf{p}$ method since the form for the effective mass tensor is found by treating the $\mathbf{k} \cdot \mathbf{p}$ terms, that arise in the

$m_w = 0.26 m_0 \qquad m_b = 0.278 m_0$
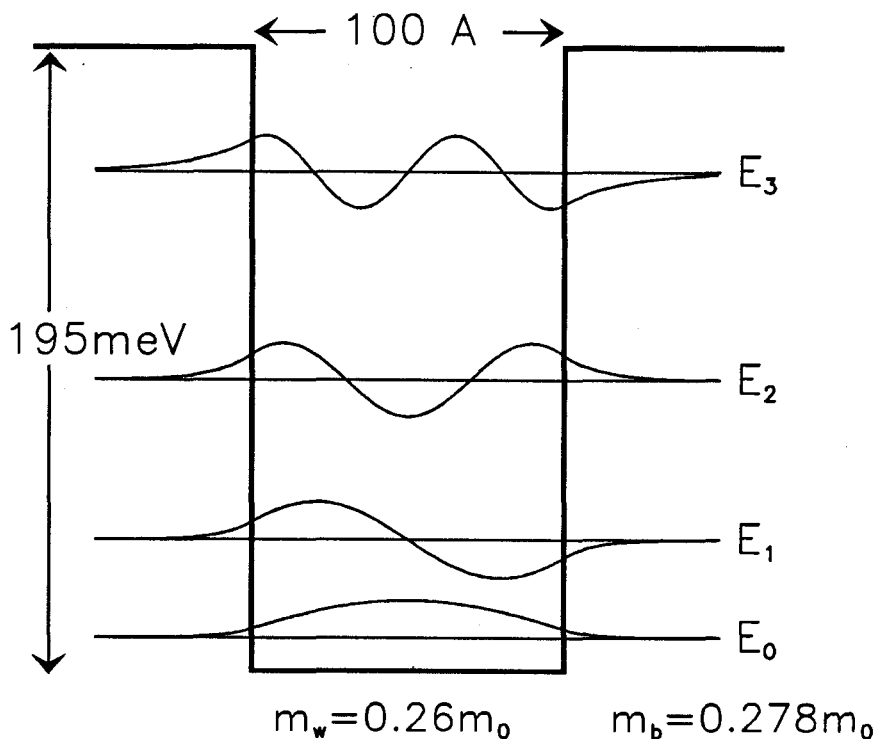
Figure 1.4 Envelope functions (real parts only) for a carrier in a single quantum well, from the single band Schrödinger equation (eq. 1.3). The calculations were carried out for a 100 Å well width, with the well depth and effective mass parameters corresponding to a heavy hole in a $Si_{0.8}Ge_{0.2}$ well with Si barriers (see Chapter 5).

Hamiltonian for non-extrema k, using perturbation theory (see for example [55L, 93Sb]). Note that the **k·p** terms are not linked with any physically real potential (other than the crystal potential), but are just a result of substituting **p**=-i∇, and the Bloch functions, u_{jk} $e^{ik·r}$ into the one electron Schrödinger equation. The resulting approximate energy eigenvalues are then written in terms of the known energy eigenvalues and **p** matrix elements for the band extrema (usually **k**=0):

$$E_{nk} = E_{n0} + \frac{\hbar^2 k^2}{2\,m_0} + \frac{\hbar^2}{m_0^2} \sum_{j \neq m} \frac{\left| \mathbf{k} \cdot \langle j0 | \mathbf{p} | m0 \rangle \right|^2}{E_{j0} - E_{m0}} \tag{1.2}$$

Summing over <u>all</u> the band edges for each value of k then gives the correct energy eigenvalues (recall that we are still dealing with just bulk Hamiltonians). However, for practical reasons the sum is restricted to the eight most important bands, the conduction band, the split off band, and the heavy and light hole valence bands. The bulk Hamiltonian for each material then consists of an 8x8 matrix and correspondingly the sum over j in the equation for the quantum well wave function (equation 1.1) is restricted to the same eight periodic functions.

By truncating the wave function from an infinite number of bands to only eight we obviously lose some information. The chosen bands are sometimes 'coupled' to those which were discarded, so that solving each of these truncated bulk Hamiltonians leads to the incorrect dispersion relations. Notice that this 'coupling' is again just a consequence of the method chosen to approximate the shapes of the energy bands in the vicinity of the extrema (i.e. equation 1.2). The correct band non-parabolicity can be accounted for by renormalizing the elements of the truncated matrix to account for the bands which were neglected. The matrix elements of the Hamiltonian are written as second order polynomials in k, with the coefficients treated as fitting parameters needed to reproduce the correct dispersion relations [55L]. Care must be taken in using these coefficients since different versions exist even for the same material, depending on whether all eight bands

16

are included in the truncated Hamiltonian. The form of the bulk Hamiltonians appropriate for Si, Ge, and SiGe are given in the Appendix.

These same Hamiltonians are then used to describe piecewise the equation to be satisfied by the wave function in the barrier and well regions of the quantum well, with the addition of a potential difference at the interfaces to account for the band offsets (see the Appendix for how to do this for SiGe quantum wells). Solving the Hamiltonian, subject to the usual decay for $z \rightarrow \pm \infty$ and the boundary conditions at the interfaces as described below, then leads to the desired wave functions and eigenenergies. If the bands are coupled (i.e. the matrices have non-diagonal elements) then solving this eigenvalue problem can be a formidable task (see for example [86B]). If the bands are not coupled and are approximately parabolic, then the problem for each de-coupled band simply reduces to the one dimensional time independent Schrödinger equation:

$$-\frac{\hbar^2}{2\,m^*(z)}\frac{d^2\phi_n}{dz^2} + V(z)\,\phi_n = E_n\,\phi_n \qquad (1.3)$$

where E_n is the energy eigenvalue of the nth eigenstate relative to the band edge, $m^*(z)$ is the z-dependent effective mass of the carrier and the potential difference at the interface is given by $V(z)$. Even and odd symmetry envelope functions, as shown in Figure 1.4, then have eigenenergies given by solutions to the familiar transcendental equations:

$$\tan\left[\frac{k_w\,L}{2}\right] = \frac{m_w\,k_b}{m_b\,k_w} \quad \text{(even)} \qquad \cot\left[\frac{k_w\,L}{2}\right] = -\frac{m_w\,k_b}{m_b\,k_w} \quad \text{(odd)} \qquad (1.4)$$

with wave vectors,

$$k_w = \sqrt{\frac{2\,m_w\,E_n}{\hbar^2}} \qquad\qquad k_b = \sqrt{\frac{2\,m_b\,(V-E_n)}{\hbar^2}} \qquad (1.5)$$

where the energies have been expressed relative to the bottom of the well, the well width is L, the band offset is V, and the carrier effective masses in the well and barrier layers are m_w and m_b, respectively.

These equations were derived by applying the usual boundary condition of continuity of the envelope function ϕ_n at the well-barrier interfaces (and hence continuity of the wave function, assuming the u_{j0} are constant across the interfaces). However, an important subtlety arises because of the different bulk band structures in the well and barrier regions. In order to conserve probability current we need to modify the usual boundary condition on the slope of ϕ_n, to instead be continuous in $1/m^*\ d\phi_n/dz$ [86B]. This leads to the effective mass factors (m_w and m_b) in equations (1.4). The resulting approximate wave functions therefore have a sharp kink at the well/barrier interface. While a soft kink in the wave function is expected, this sharp kink is an artifact of our assumption of identical u_{j0} on either side of the interface. For further discussion on how this comes about see Burt [92B]. The kink is not obvious in Figure 1.4 since the effective heavy hole masses in the z-direction in the well ($0.26\ m_0$) and barrier ($0.278\ m_0$) regions are very similar. These masses correspond to the situation expected for a $Si_{0.8}Ge_{0.2}$ quantum well in Si (see Chapter 5), demonstrating that in physically realizable systems the effect is in fact a small one. The energy eigenvalues found using the envelope function technique with the boundary conditions described above, are usually in reasonable agreement with experimental observations. In Chapter 5, the envelope function scheme is used to calculate the energy eigenvalues for single SiGe quantum wells, and the results are found to compare well to the observations by PL spectrocopy.

1.5. Superlattices and Multiple Quantum Wells

Interesting new properties can also be produced by alternating many layers of each semiconductor material to make a one dimensional periodic structure. This structure is known as a superlattice when there is significant leakage of the electronic wave functions across the barrier regions. Typically barrier layers of less than ~ 10 monolayers in thickness are necessary. The term multiple quantum well (MQW) is used when the barrier layers are too thick to allow communication between adjacent quantum wells. The coupling between wells in the superlattice causes the discrete energy levels, described in the previous section, to split. In the limit of many coupled wells the splitting in energy levels gives rise to continuous bands known as mini-bands. These energy mini-bands can be calculated to a first approximation using a Kronig-Penney analysis, where instead of a lattice with periodicity given by the lattice constant of the material, the period is that of the superlattice structure. The band structure of the bulk material arises from imposing the periodic potential of the crystal on free electrons, resulting in Bloch electrons which behave with some effective mass, m^*. In the superlattice, a further periodic potential is applied to these Bloch electrons so that within the electronic bands of the bulk we have the substructure of the mini-bands.

Strained layer superlattices made up of alternating layers of elemental (not alloy) Si and Ge have been proposed as a means of producing a direct band gap in a Si-based technology. The basic idea is to produce a structure with a period that subdivides the Brillouin zone by five, so that the X point conduction band minima normally located at 4/5 the distance to the zone edge are folded back to the Brillouin zone center [74G, 88S]. Because the Si unit cell consists of 2 atoms, the shortest atomic layer superlattice period that gives the required zone-folding is 10 atomic layers. Most experiments have concentrated on a structure consisting of 4 monolayers of Ge alternated with 6 mono-layers of Si. However, the early experimental claims of observation of the predicted direct

gap were a source of controversy. There is now wide spread acceptance that these initial reports of photoluminescence attributed to the direct gap [90Z, 89O] were in fact due to either dislocations or to processes originating in the SiGe buffer on which the Si/Ge superlattice was grown [90N, 90S]. A more comprehensive study was reported very recently by Olajos *et al.* [92O] in which the Si-Ge superlattices were first characterized by absorption, which gave more convincing evidence that the peaks observed in the photoluminescence and electroluminescence spectra were in fact due to band to band transitions and not to some deep dislocation related center. A strong photoluminescence peak (at 760 meV) was seen from a strain symmetrized Si_5Ge_5 superlattice roughly in agreement with their theoretical prediction of the zone folded direct gap. This peak was shown to be absent in a reference sample consisting of the buffer layer alone and also disappeared when the superlattice was carefully etched away. As well, better quality epitaxy resulted in layers with dislocation densities an order of magnitude less than the earlier studies. However, these experiments have yet to demonstrate the increased quantum efficiency expected for a direct gap transition.

The coupling between adjacent wells in such superlattices occurs because the electronic wave functions leak through the thin barriers. We can also study the case of tunneling of carriers through a single thin barrier separating two regions of lower potential. Tunneling is one of the most elegant demonstrations of quantum mechanics. In classical physics a particle cannot escape a region of low potential unless it acquires sufficient energy to overcome the barrier. In contrast, in quantum mechanics a carrier occupying an eigenstate with energy less than the barrier height has some probability of being found on the other side if the barrier is finite in thickness. Resonant tunneling diodes are based on two such barriers on either side of a quantum well. When a potential is applied across the device so as to align the Fermi level with what is normally a bound eigenstate of the quantum well, then carriers can tunnel through both barriers to reach the other side. When the Fermi level does not correspond to such an eigenstate then the

tunneling probability is substantially lower. At the resonance energy the tunneling

probability through the two barriers is actually higher than through a single barrier. This

surprising result is a consequence of the wave nature of the electron. The dependence of

the tunneling current on the applied voltage in this structure produces a region of negative

differential resistance which is used to make amplifiers and oscillators.

Another interesting structure is the coupled double quantum well (CDQW),

consisting of two identical quantum wells coupled together by a thin barrier (see Figure

1.5). The bound eigenstates can be found by solving the Schrödinger equation (eq 1.3),

with the appropriate substitution of $V(z)$ for the two well case, along with the additional

boundary conditions. Each discrete energy level splits into two, corresponding to

symmetric and anti-symmetric solutions, as shown by the envelope functions in Figure 1.5.

A particle in one of these bound states has equal probability of being found in either of the

two wells. The energy splitting between the symmetric and antisymmetric solutions
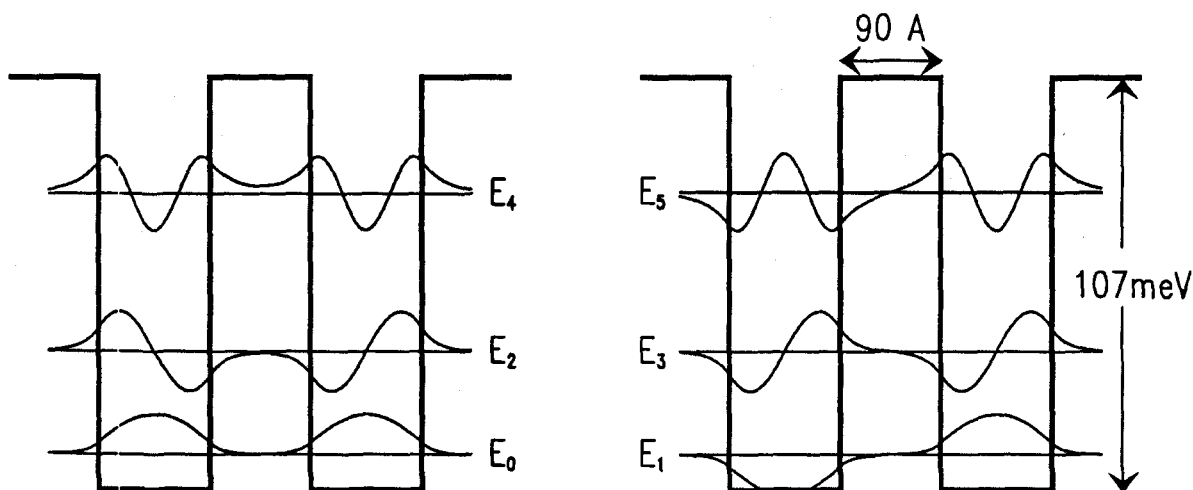
Figure 1.5 Envelope functions (real parts only) for coupled double quantum wells. Each energy level of the isolated wells splits into two corresponding to symmetric, E_0, E_2, E_4 and anti-symmetric, E_1, E_3, E_5 solutions. Calculations correspond to 100 Å well widths, 90 Å barriers, with the well depths and effective mass parameters for heavy holes in $Si_{0.87}Ge_{0.13}$ quantum wells with Si barriers (see Chapter 5).

depends on the strength of the coupling between the wells, with a return to the isolated well eigenstates (i.e. zero splitting) in the limit of infinite barriers. Alternatively, if we considered a flux of particles incident from one well, then the probability of tunneling to the other well depends exponentially on the barrier thickness.

The calculated envelope functions in Figure 1.5 correspond to heavy hole states of two 100 Å $Si_{0.87}Ge_{0.13}$ quantum wells coupled by a 90 Å Si barrier. The carrier effective mass was assumed to be about 0.28 m_0 for reasons discussed in Chapter 5. The relatively thick (90 Å) barrier leads to splittings of only 3.2 μeV, 32 μeV and 3.9 meV between the symmetric (E_0, E_2, and E_4) and anti-symmetric (E_1, E_3, and E_5) solutions, respectively. The largest splitting (3.9 meV) is observed for the highest excited bound states (E_4 and E_5) since the higher energy states of the isolated wells extend furthest into the barriers and therefore are the most strongly coupled in the CDQW structure.

Now consider the case of two wells which have different well depth and/or thickness, known as asymmetric coupled double quantum wells (see Figure 1.6). Again, we can solve the Schrödinger equation and arrive at a new set of eigenstates which are perturbed from those of the isolated wells due to the coupling. In practise, this is a significantly more complicated problem than the symmetric CDQW discussed above, since we need to solve for eight coefficients to describe ϕ, compared to five such coefficients in the symmetric case. If the eigenenergies of the two wells when isolated from each other are very different, the probability of an electron being in one well can now be much greater than in the other (see Figure 1.6). In asymmetric coupled quantum wells the coupling depends not only on the barrier width, but also on the difference in energy of the eigenstates of the two isolated wells. We can understand how this comes about by considering the phase of $\phi(z)$ for some particular energy (i.e. wavelength). If the wavelength of one of the isolated well eigenstates is such that $\phi(z)$ is near a maximum at the barrier/well interface of the other well, then the peak magnitude of the wave function within this second well must be very small in order to to satisfy the boundary conditions of
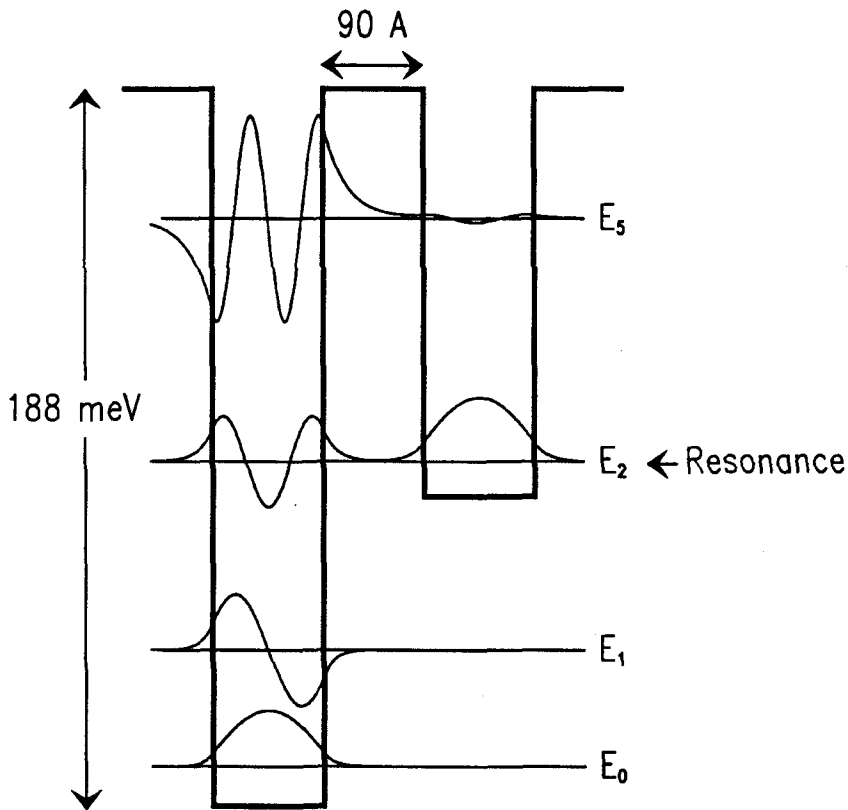
Figure 1.6 Envelope functions (real parts only) for asymmetric coupled quantum wells. There is a high probability of being in either well only with resonance between levels of the isolated wells (see level E_2). Calculations correspond to 100 Å well widths and a 90 Å Si barrier, with the well depths and effective mass parameters for heavy hole states of a $Si_{0.87}Ge_{0.13}$ well coupled to a $Si_{0.75}Ge_{0.25}$ well (see Chapter 5).

continuity of ϕ and its derivative with the exponential decay inside the barrier. If two of the isolated well energy levels coincidentally line up then we have resonance conditions and the probability of being in either well is again high (ϕ_2 in Figure 1.6). Again this means that a flux of carriers initially in one well can resonantly tunnel to the other. If on the other hand we have non-resonant conditions then tunneling can still occur through some assisting process, such as impurity or phonon scattering, however the tunneling probability is much lower. This will be discussed further in Chapter 5., where experimental evidence of carrier tunneling in a SiGe/Si asymmetric coupled quantum well structure is presented.

Chapter 2.

Introduction to Photoluminescence

2.1. Silicon and Germanium

Photoluminescence (PL) is the light emitted from a material following optical excitation. The excitation is usually provided by a laser with wavelength above the band gap, which creates a large number of free carriers. These free carriers do not usually recombine immediately, but rather can lose energy nonradiatively by emitting phonons until reaching the conduction and valence band edges. At low temperatures the energy is further lowered by the electron-hole pairs binding together through Coulomb interaction to form excitons. These excitons are known as free excitons (FE) since they migrate through the crystal, with kinetic energy given by the Maxwell-Boltzmann distribution. Often this migration leads to interaction with an impurity or defect which can result in the exciton recombining nonradiatively. When the free excitons do recombine radiatively the radiation emitted is characteristic of the material:

$$h\nu = E_g - E_x - E_{ph} + K.E. \qquad (2.1)$$

where E_g is the band gap, E_x is the energy binding the electron and hole together, E_{ph} is the energy of a momentum-conserving phonon, and K.E. is the kinetic energy term. FE recombination therefore results in a characteristic PL lineshape consisting of a sharp low

energy edge corresponding to an exciton with zero center of mass momentum and a Maxwell-Boltmann tail to high energy.

In the presence of impurities or defects the FE can lower its energy by binding to an impurity or defect center to form a bound exciton (BE). This localization eliminates the kinetic energy distribution found for FE and therefore BE recombination leads to a narrow PL emission line. In Si and Ge the BE localization energy is approximately one tenth the impurity ionization energy for shallow donors and acceptors. Both materials therefore obey the empirical relation known as Hayne's rule [60H], in which the localization energy varies linearly with ionization energy. Note that because the BE localization energy is much smaller than the impurity ionization energy, at temperatures where BE localization is significant there is no thermal ionization of the impurities. The ionization energies of the shallow acceptors and donors in Si and Ge can be predicted by using the effective mass approximation. The impurity potential is considered as a perturbation in the perfect periodic potential of the crystal. The result is a series of hydrogenic impurity levels scaled by the carrier effective mass and the dielectric constant of the host lattice. The energy levels in Ge are shallower than those in Si by about a factor of four due to the larger dielectric constant and smaller effective masses. All acceptors or all donors in a given material are predicted by the effective mass model to have the same ionization energy.

However, the short-range potential in the vicinity of different impurities does in reality vary, and this is found to manifest itself in the lowest lying energy levels (i.e. most tightly bound carriers) in deviations from the hydrogenic values known as central cell corrections. It is these differences imposed by the central impurity cell that fortuitously gives us different ionization energies (and exciton localization energies) for different impurities and therefore allows us to identify recombination of excitons bound to different impurities in the PL spectrum. The most common substitutional impurities in Si and Ge are the donors phosphorus and arsenic, and the acceptor boron. In addition complexes made up of oxygen and/or carbon are often present. For a review of shallow impurities in

25

Si and Ge see Ramdas and Rodriguez [81R]. PL spectroscopy offers sensitivity to impurity concentrations as low as 10^{11} cm^{-3} , several orders of magnitude better than more conventional techniques such as SIMS (secondary ion mass spectroscopy) or electrical characterization. In addition PL is non-destructive and does not require elaborate sample preparation, such as the deposition of electrical contacts. However, quantitative determination of impurity content is quite difficult using PL, since it requires calibration between the individual impurity concentrations and the strength of the related BE peak relative to the FE.

If the exciton generation rate is high, more than one exciton can bind to each impurity to form bound multi-exciton complexes (BMECs). When an electron and hole contained in one of these complexes annihilate, the emitted PL is typically shifted relative to the principal BE transition by an amount characteristic of the impurity and the number of excitons bound to it. Following extensive debate on the origin of a series of peaks observed in Si under high excitation, the BMEC model was found to be correct [82T]. This acceptance was largely due to the success of Kirczenow's shell model [77K] in describing the major transitions and the behaviour of the PL peaks under external perturbation such as stress or magnetic field. For an extensive discussion of BE and BMEC recombination in Si see the review by Thewalt [82T]. Under conditions of very high excitation and/or in ultra-high purity material the electron-hole pairs can also condense to form an electron-hole droplet or electron-hole plasma (see for example the review by Rice [77R]).

Phonons usually participate in the band-edge PL transitions in indirect band gap materials, such as Si and Ge, because of the difference in k-values between the hole and the electron. The phonon accounts for the difference in crystal momentum between the nearly negligible amount carried away by the emitted photon and the overall crystal momentum of the recombining electron-hole pair. For example recombination of a band-edge electron-hole pair in Si results in an approximately 1.1 eV photon, which has a

corresponding wave vector of $k=10^5$ cm^{-1}, compared to the difference in k values of the electron and hole of $k = 0.85 (2\pi/a_0) = 10^8$ cm^{-1}. The phonon takes up this difference in momentum but also carries away some energy (at low temperature only phonon <u>emission</u> is significant). The participation of the phonon therefore reduces the energy of the emitted photon by an amount given by the phonon dispersion at the appropriate value of k (i.e. up to about 58 meV in Si). This results in a series of phonon replicas of the PL transitions shifted to lower energy by the corresponding transverse acoustic (TA), transverse optic (TO), longitudinal acoustic (LA) or longitudinal optic (LO) phonon energies. These phonon dispersion curves are well known for both Si and Ge (see for example Sze [81S]).

In the case of the BE, the impurity central cell potential can couple to the exciton so that a no-phonon transition is often observed in addition to the phonon replicas. The relative strength of the no-phonon peak to its phonon replicas is related to the spreading of either the electron or hole wave functions in k-space, since more spreading corresponds to a larger overlap of the electron and hole wavefunctions.

2.2. Unstrained Si$_{1-x}$Ge$_x$ Alloys

While the SiGe alloy has not been as extensively investigated as elemental Si and Ge, a number of PL studies have been reported. The earliest studies concentrated on Ge-rich alloys (see for example [73G] or [74B]), with a more recent paper by Mitchard and McGill [82M] dealing with Si-rich material, and finally a comprehensive study across the entire compositional range by Weber and Alonso [89Wb]. Note that this section deals entirely with bulk (i.e. unstrained) SiGe grown by traditional Czochralski or float zoning techniques. The remainder of the thesis will describe our own results on SiGe grown epitaxially on Si (i.e. strained).

Like Si and Ge, SiGe is an indirect gap material, so the PL spectra should be dominated by momentum conserving phonon replicas. However, in alloys the momentum conservation rules are relaxed even for FE, since the statistical distribution of Si and Ge atoms can act as scattering centers. In other words the Ge atoms are thought of as isoelectronic (of the same valency) impurities in the Si lattice. Potentials created by regions of high or low Ge fraction repel or attract excitons and result in an enhancement of no-phonon transitions. In fact, in bulk alloys a very strong no-phonon FE transition was observed [89Wb, 82M], in contrast to pure Si and Ge where it is extremely weak.

The phonon modes expected in SiGe alloys were examined by Barker [68B] using a simple 1-D model which treated first and second nearest neighbours to be linked by simple central force springs. The alloy nature was accounted for by weighting the restoring force acting on a particular atom by the probability of a like or unlike atom for the nearest neighbour. The transverse optic mode split into three distinct modes consisting of Si atoms moving (Si-Si), both Ge and Si vibrating (Si-Ge), and mostly Ge vibrating (Ge-Ge). In contrast, solutions for the transverse acoustic mode showed a gradual transition from the mode of pure Si to pure Ge with increasing Ge fraction.

The three TO and one TA modes were observed in the BE PL spectra of bulk SiGe by Weber and Alonso [89Wb]. The TO energies are approximately constant, with only a slight change (about 3 meV) observed at Ge composition x=0.85 arising from the need for phonons of different symmetries at the changeover in the electronic state from Si-like to Ge-like. The TA energy varies approximately linearly with x. The intensities of the three TO PL peaks were found to be proportional to the number of pairs of appropriate atoms predicted by a random distribution in the alloy:

$$\frac{I^{TO}_{Ge-Ge}}{I^{TO}_{Ge-Si}} = \frac{x}{2(1-x)} \qquad\qquad \frac{I^{TO}_{Si-Si}}{I^{TO}_{Ge-Si}} = \frac{1-x}{2x} \qquad (2.2)$$

An LA mode was also observed in the Ge-rich material. This is not suprising since coupling to TO phonons is strongest in Si, while in Ge the LA replica is favoured.

However, the overall strength of the phonon replicas compared to the no-phonon peak was considerably reduced in the Ge-rich alloys.

Another consequence of the alloy nature of the SiGe is broadening of the optical transitions, with the observed BE peaks having a typical full width half maximum (FWHM) > 4 meV [89Wb, 82M]. This contrasts BE in pure Si or Ge for which lines are usually less than 0.1 meV wide. The broadening observed in the SiGe luminescence can be accounted for by fluctuations in Ge concentration in the vicinity of the impurity which binds the exciton. In other words the luminescence energy varies from place to place in the alloy, depending on the proportion of Ge atoms in each region. This luminescence energy is made up of three terms, the host band gap, the FE binding energy, and the energy binding the exciton to the impurity. The FE binding energy would be expected to vary between 14.7 meV for pure Si and 4.2 meV for pure Ge. Similarily typical BE binding energies in Si are 4 to 10 meV, while being about an order of magnitude smaller in Ge. There is a much larger change in energy associated with the band gap, with E_g = 1170 meV in Si and 650 meV in Ge. We therefore neglect the relatively small fluctuations in FE and BE binding energies and simply consider the band gap variations. Assuming a random distribution of Ge atoms in the lattice, the PL linewidth (ΔE_{PL}) is then appproximately 2.36 times the standard deviation in the band gap energy due to the fluctuations in x within the exciton volume (see for example [89Wb]):

$$\Delta E_{PL} = 2.36 \frac{dE_g}{dx} \sqrt{\frac{x(1-x)}{\frac{4}{3}\pi a_B^3 N}} \qquad (2.3)$$

where a_B is the exciton Bohr radius, N is the density of lattice sites in the alloy, and dE_g/dx can be taken from the observed PL peak energies (Figure 1.2). Using this expression with the Bohr radius as a fitting parameter, Weber and Alonso [89Wb] found that a_B = 38Å for x < 0.85 and 110 Å for x > 0.85 gives BE linewidths which are in agreement with their observed values (4 to 7 meV) as a function of x. These values for the Bohr radius correspond well to what is expected for shallow bound states in Si or Ge.

29

The broad linewidth in the SiGe precludes the chemical identification of individual shallow impurity BE peaks. Given the observed BE separation from the FE peak in the PL of about 3-6 meV, which was in agreement with the binding energy of 5 meV obtained from the BE intensity as a function of temperature, possible exciton binding centers are boron, phosphorus or arsenic [89Wb].

One of the most significant results of the bulk SiGe PL studies of Weber and Alonso [89Wb] was the use of the PL transition energies to determine the excitonic band gap as a function of x (Figure 1.2). The excitonic band gap refers to the FE recombination energy (see equation 2.1), therefore it is shifted to lower energy relative to the actual band gap by the FE binding energy. Since the impurity concentration was too high to detect a FE line in many samples, the excitonic band gap was approximated by using a BE binding energy scaled linearly between Si (~5meV) and Ge (~ 1 meV) [89Wb].

As well as the BE and FE PL, a broad feature (and its phonon replica) was observed in the bulk SiGe PL spectra about 5 meV below the BE line, but only under conditions of high excitation [89Wb, 82M]. This emergence only at high power and spectral position relative to the BE is similar to the observation of the BMECs typically seen in Si and Ge. In the case of the SiGe alloy however, detailed studies are impeded by the alloy broadening which is thought to result in the observed broad band rather than resolved individual BMEC peaks. In fact in most cases the BE and the BMEC band were not even resolved, but rather the BE simply appeared to broaden and shift to lower energy at high excitation levels [89Wb].

An additional luminescence band, labelled the L-band, was observed in some samples which appears to be unique to the SiGe alloy. This broad luminescence band occurs roughly 20 meV below the FE no-phonon transition and is found to exhibit an unusually large shift (up to 45 meV) to lower energy with increasing temperature. The linewidth is equally puzzling in that it decreases and the band becomes more symmetric with increasing temperature, until about 40 K at which the line again broadens [89Wb].

Because of its presence only in an indium doped sample, Mitchard and McGill [82M] incorrectly identified this PL band with indium BE PL. Weber and Alonso [89Wb] later showed that the L-band was in fact observed in the absence of indium impurities, but only at high temperatures or under conditions of high power where laser heating of the sample was likely. Some association with dislocations was suggested by the observation of the largest temperature dependent L-band shift in a sample with a large number of dislocations. The L-band was interpreted by Weber and Alonso [89Wb] as a high-density electron hole plasma created in potential wells formed by large Si-Ge alloy fluctuations. They further proposed that the connection between the L-band and the dislocations might originate from the strong likelihood of dislocations being present in the vicinity of these potential wells.

The particular experimental techniques used to collect our photoluminescence spectra for strained SiGe on Si (Chapters 4 and 5) are described in the next chapter. As well, a brief description of epitaxial SiGe growth techniques is given.

Chapter 3.

Experimental Techniques

3.1. Fourier Transform Photoluminescence Spectroscopy

The components of a basic PL spectroscopy set-up consist of a source to excite the sample, a dewar to keep the sample cold, and an instrument to measure the emitted PL as a function of wavelength. The exact nature of each of these components is tailored wherever possible to suit the particular PL features of interest. The SiGe luminescence falls between the Si and Ge band gap energies. In particular, the focus of this study is Si-rich alloy layers, for which the luminescence energies are roughly between 800 and 1170 meV or 1.55 to 1.06 μm. The SiGe PL spectra were taken using the method of Fourier transform PL spectroscopy, which is briefly summarized in this section. The next section describes the PL experiments which required use of dispersive methods, specifically time-resolved spectroscopy and photoluminescence excitation spectroscopy. More details on the experimental techniques can be found in the Ph.D. theses of previous students [92Nb, 86S].

The advantages of using an interferometer instead of a dispersive instrument for PL studies are well known (see for example Nissen [92Nb] or Thewalt *et al.* [90Ta] and references therein). The most relevant benefits are the multiplex advantage and the throughput advantage. The multiplex advantage comes about because in interferometry

the detector simultaneously samples all of the optical signal, compared to dispersive techniques where only one spectral channel is sampled at a given time. When the signal to noise is limited by detector noise, the multiplex advantage results in an improvement of $\sqrt{N}$, where N is the number of resolution elements in the spectrum. Detector noise is not a problem for relatively strong signals or when using a low background noise detector such as a photomultiplier tube (see section 3.2). However, in the case of the SiGe PL, the signals are fairly weak and usually fall outside the range of photomultiplier tubes, so that the multiplex advantage is important. Even though the resolution required for the SiGe spectra is relatively low ($\sim$ 0.5 meV), the multiplex advantage results in a predicted improvement in signal to noise over dispersive methods of roughly 10 times for a SiGe spectral range of 65 meV. The throughput advantage arises because the width of the entrance slit of a dispersive spectrometer must be two or three orders of magnitude smaller than the diameter of the aperture used in an interferometer, in order to obtain the same high spectral resolution. For example, a typical SiGe spectrum with resolution of 0.5 meV requires a slit width of roughly 500 μm on our spectrometer set-up compared to an aperture of 7 mm diameter on the interferometer. Assuming that the spectrometer slit is illuminated over 1 cm in height, this translates to a collection area roughly 7 times larger for the interferometer. As well there is another factor of four advantage for the interferometer since it has f4 optics versus f8 for the spectrometer.

Other advantages of interferometry are the broad spectral capabilities, high spectral accuracy, and ability to switch between very high and very low resolution without re-configuring the apparatus. The fact that one can quickly take a spectrum over a very large range of wavelengths is especially convenient in this study since the SiGe features shift significantly with Ge fraction and quantum confinement effects.

The Fourier transform PL spectroscopy is performed on a BOMEM DA8.02 Fourier transform interferometer [BM]. As shown in Figure 3.1, it has essentially the same configuration as a classic Michelson interferometer. The luminescence is collected and
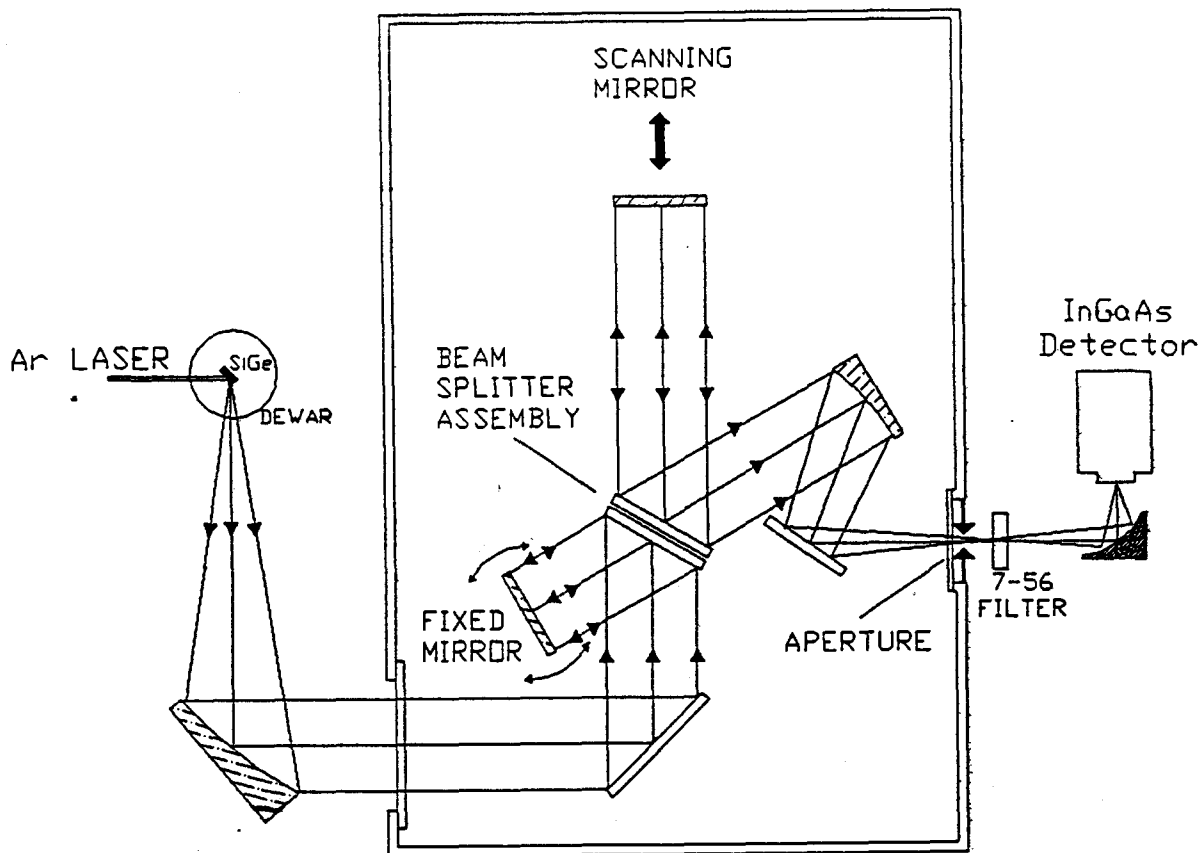
Figure 3.1 Schematic of the BOMEM Fourier transform PL spectroscopy set-up. The most unique feature of the BOMEM is the dynamic alignment of the moving and fixed mirrors, which facilitates use at near infrared wavelengths. For the SiGe work an InGaAs detector, and either a quartz or a CaF$_2$ beamsplitter were used.

collimated by an off-axis parabaloid mirror which directs it into the interferometer through a 4 inch quartz window. The PL signal is then split so that the transmitted beam follows the path of the moving mirror and the reflected beam is directed onto the fixed mirror. For SiGe PL a beamsplitter with either a quartz or Ca_2F substrate is used. The quartz beamsplitter is best for SiGe samples with shallow PL since it is slightly more efficient than the Ca_2F for wavelengths less than about 1.15 µm. For deeper SiGe features the Ca_2F beamsplitter is more suitable since the quartz has a strong absorption band near 1.3 µm. After the two beams recombine at the beamsplitter, the resulting interferogram is directed out of the interferometer via a Ca_2F window and onto the detector.

For the spectra described in this study, the inteferogram was detected by an InGaAs photovoltaic detector (Epitaxx model ETX 1000 TV). The detector is mounted in a liquid nitrogen cooled cryostat, along with a dual channel J-FET pre-amplifier and 100 MΩ feedback resistor that couple it to another pre-amplifier (Cincinnati Electronics model EEH-100). This signal is then further amplified (Ithaco model 1210 amplifier) and finally fed into the BOMEM electronics. The scattered light from the PL excitation source (i.e. an Ar laser, see below), which is much more intense than the PL signal itself, is rejected with a coloured glass filter (Corning 7-56) placed in front of the detector.

There are two unique features of the BOMEM interferometer that make it ideal for semiconductor PL studies. The first is the real-time numerical filtering which enables very fast collection of the interferogram and subsequent calculation of the Fourier transform. The second feature is dynamic alignment of the mirrors, which is crucial in performing high resolution spectroscopy in the near infrared region. The fixed mirror must remain parallel, to within a fraction of the wavelength of the light under study, to the moving mirror as it is scanned. While this is relatively easy in the mid to far-infrared ($\lambda \geq 10$ µm), where interferometers have been employed routinely for some time, at wavelengths of typical semiconductor luminescence (~1 µm) the technology must be much more sophisticated. The BOMEM accomplishes this by dynamically aligning the mirrors as the

moving mirror is scanned. The dynamic alignment system uses the laser beam from a single mode He-Ne laser which is expanded to a 1 inch diameter and directed onto the beamsplitter. The resulting He-Ne interferogram is monitored by an array of photodiodes. When the mirrors are misaligned then the reflected beam from the moving mirror recombines at the beamsplitter with a reflected beam from the fixed mirror that originated from a different part of the He-Ne beam cross-section. This results in multiple interference fringes. Alignment of the mirrors is indicated by a single interference fringe over the width of the He-Ne beam. The signal from the photodiode array is used to control two servo motors, which adjust the angle of the 'fixed' mirror so as to maintain the single He-Ne interference fringe during the entire scan.

The SiGe luminescence was generated by an argon ion laser which optically excites the sample. It provides blue (488 nm) and/or green (514.5 nm) light which is well above the band gap in Si and Ge and therefore generates a large number of electron-hole pairs. Excitation power densities in the range of a few μW cm^{-2} to tens of W cm^{-2} were obtained by diffusing or focusing the laser beam and using neutral density filters, as necessary. For spot sizes greater than 1 cm^2 the power densities were measured directly using a pyroelectric radiometer (Molectron PR-200). For smaller spot sizes (i.e. higher power densities) the active area of the radiometer is not entirely covered and so only power and not power density can be measured. For the undiffused laser beam we therefore switched to a Newport Si diode detector which also measures power but is more convenient to use than the radiometer.

The PL spectra were collected with the SiGe sample maintained at low temperature, so that the only source of excitation is the laser beam. At higher temperatures the PL features are either broadened by the thermal energy or the excitons, which are only weakly bound together, completely dissociate. The samples were typically immersed in boiling (4.2 K) liquid helium. Temperatures as low as 1.8 K were obtained using a mechanical pump to lower the pressure above the liquid to below the He lambda point. Use of

superfluid helium also reduces scattering of the excitation laser beam usually encountered in boiling He. This was especially critical in the localized exciton studies described in sections 4.3.and 5.3., where careful control of the power density reaching the sample was needed. For the temperature studies, the samples were attached to a large piece of Si using thermal compound and placed in a flowing He gas Super Varitemp dewar. The Si block provided good thermal contact between the thin SiGe sample and the temperature sensor via the helium gas. The temperature was detected and controlled using a Si diode sensor and a heater mounted on the sample holder.

Normally only relative intensities of PL features in a spectrum are necessary to characterize a semiconductor material. However as described in Chapter 4, measurement of the external quantum efficiency of a unique PL process was one of the most important pieces of evidence in understanding the SiGe PL. The quantum efficiency is simply the ratio of the number of photons emitted by the sample versus the number of photons absorbed. Quantum efficiency can be measured using an integrating sphere which removes any directional dependence of the emission to give a representative value of emitted flux. The emission source (in this case a SiGe sample) is simply placed inside a hollow sphere and the emitted signal is measured via a small port which is not under direct illumination by the source. The most important aspect of the sphere is the inside surface, which is coated with a special white paint that provides a high reflectivity that is independent of wavelength (in the region of interest) and is diffusely reflecting. The sphere and detector are usually calibrated by measuring the signal at the collection port from a source of known intensity. While integrating spheres are commercially available and are routinely used at room temperature, these spheres are inappropriate for use at 4.2 K. One problem is that integrating spheres are not usually manufactured small enough to fit into the dewar tail, which is only 2 inches in diameter. More importantly, the diffusely reflecting white paint is likely to flake off at liquid He temperatures.

We therefore designed a small integrating sphere which was milled out of two halves

of a piece of aluminum stock that fit into the dewar tail. The inside surface of the sphere was coated with gold which provides a high reflectivity at the wavelength of the SiGe PL. The diffusely reflecting surface was created simply by sand-blasting the sphere to give a roughened surface and then evaporating the thin layer of gold on top. The sample was mounted at the back of the integrating sphere, as shown in Figure 3.2 .The laser excitation entered through a small hole perpendicular to a port through which only the diffusely reflected PL signal was collected by the interferometer. The intensity of light escaping the sphere and instrumental response were then calibrated by shining incoherent light of a known power density, having approximately the same wavelength as the PL (1.3 µm), into the excitation hole and collecting the signal in the same manner. With the sample mounted at a small angle, the light is reflected in such a way that it is trapped inside the sphere and therefore acts as a good reference source. Both the laser and reference light intensity were determined before being directed into the sphere using the pyroelectric radiometer. The measurements were also corrected for an estimated sample reflectivity at the wavelength of the excitation (488 nm) of 0.62.
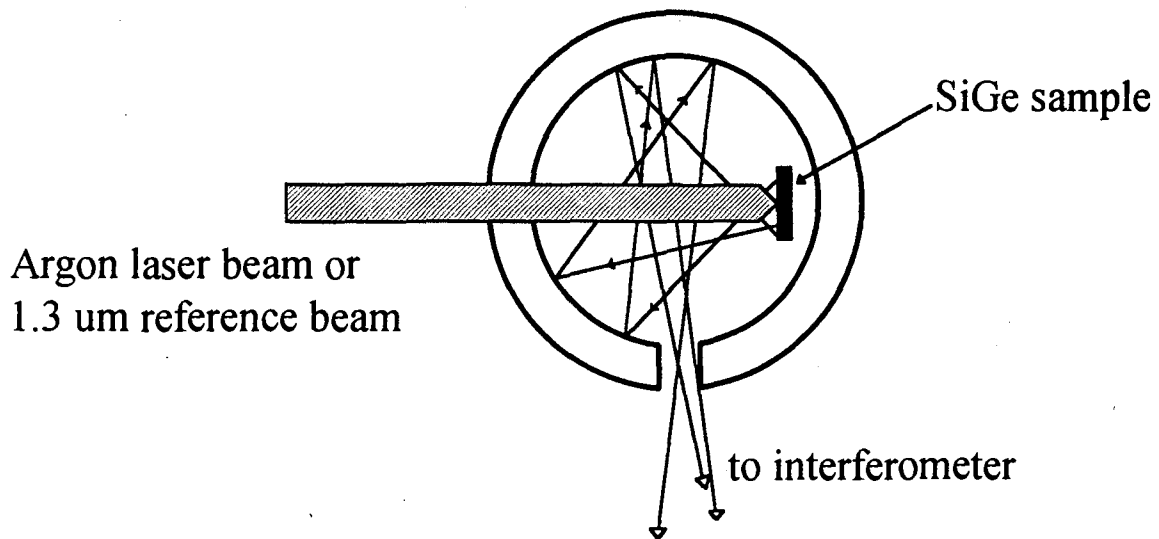
Figure 3.2 Cross-sectional view of the integrating sphere. The inside of the sphere has a gold-coated diffusely reflecting surface.

3.2. Time-Resolved and Photoluminescence Excitation Spectroscopies

Additional information about the recombining species in the PL spectra can be obtained by studying the decay in the PL signal after the excitation source is turned off. It is very difficult to carry out time-resolved PL measurements on an interferometer since it is the PL signal as a function of the position of the moving mirror, and hence scan time, that gives us the spectral information. If the frequency of modulation of the signal by the scanning of the mirror is fast (for this work it was typically a few kHz) on the time scale of the PL decay, in principle it is still possible to obtain the decay time. However, most PL processes are too short lived for this to work and it is necessary to turn to a dispersive apparatus to do time-resolved measurements.

For this study the SiGe luminescence was dispersed by a double spectrometer and detected with a photomultiplier tube (Varian VPM159A3). The photomultiplier tube is better suited to the dispersive set-up than the analog InGaAs detector used on the interferometer because we can take advantage of the capability of photon counting. The high gain of the photomultiplier tube means that single photons can produce output pulses large enough to be counted individually. Using photon counting the signal to noise can be improved over techniques which simply integrate the signal intensity over time. This is because, by setting upper and lower limits on the pulse height acceptable for a single photon count, current caused by noise can be rejected. In addition, variations in pulse height due to small differences in gain have no effect on photon counts. The ability to do photon counting is necessary to detect even moderate PL signals on a dispersive set-up because of the disadvantages (discussed in the previous section) in comparison to interferometry.

The Varian tube can detect wavelengths ranging from 0.4 to 1.22 µm (1020-3100 meV) and therefore is suitable for most Si no-phonon and phonon replica PL. However,

this is not sufficient to cover all of the SiGe samples since the PL features extended to wavelengths as high as 1.55 μm (800 meV). Unfortunately at the present time there is no detector commercially available which covers this wavelength region with enough sensitivity, and therefore we are simply limited in the spectra for which time-resolved information can be obtained.

The excitation source must be pulsed with a period long enough to allow the PL signal of interest to decay between each pulse. The continuous wave Ar laser was used, but with the Ar laser light reaching the sample pulsed by an acousto-optic modulator. The acousto-optic modulator works by setting up a refractive index grating in a crystal due to a sound wave generated by an RF-driven piezoelectric transducer. The laser beam is split by this grating into two beams, one at the Bragg angle and the other undeflected from the incident beam. The Bragg-deflected beam is directed onto the sample through a pin-hole, which is positioned to reject the undeflected beam. When the RF signal is 'off', no component of the laser beam is Bragg deflected and therefore no excitation reaches the sample. The electronics used to detect the start and stop of each laser pulse and to bin the photon counts into the appropriate time windows has been discussed in detail by Steiner [86S] and will not be covered here.

Photoluminescence excitation spectroscopy (PLE) was also performed using a dispersive spectrometer. In PLE the excitation light is scanned in wavelength while the PL signal is monitored at a fixed wavelength. Since there is no way of continuously monitoring only one wavelength, the interferometer is not well suited to PLE. As well, it is very difficult to filter the light so as to reject the excitation source but pass the PL signal. The idea behind PLE is to resonantly create excitons at some excited energy level and then detect the PL signal due to the recombination of excitons at a related lower energy level. By doing this we can probe the excited states which are normally unoccupied at low temperatures or thermally broadened at higher temperatures. PLE is a very important tool in direct gap semiconductors, although it is much more difficult to use

in indirect gap materials, such as Si, Ge and SiGe, because the absorption is very weak. The problem is compounded by the lack of a good tunable excitation source above 1 μm. The best choice is an optical parametric oscillator (OPO) which covers the appropriate wavelength range, although it can be somewhat tedious to obtain a stable output. The OPO operates by converting a visible beam into two infrared beams using a non-linear crystal ($LiNbO_3$). The tuning occurs by tuning the visible pump beam which is generated from a dye laser pumped by a Cu-vapour laser. For the SiGe PLE work, the OPO was tuned from 1.05 to 1.3 μm, for which the typical average OPO output power was 30-50 mW. The PL signal was passed though the dispersive spectrometer and monitored at a wavelength slightly higher than the excitation, using either the photomultiplier tube described above or for very strong signals the InGaAs detector. For more details on the OPO system see the paper by Thewalt and Beckett [88T].

3.3. Crystal Growth

As is often the case, collaboration with other research groups has been essential in these studies. Although the facilities at SFU provide state of the art optical characterization of semiconductor materials, we are lacking in crystal growth capabilities. We were fortunate in obtaining samples from Dr. Jim Sturm and his graduate students at Princeton University, and Drs. J.-P. Noël and Derek Houghton at the National Research Council Canada. Since growth of $Si_{1-x}Ge_x$ with good optical characteristics has only recently been attained, the techniques are briefly outlined below.

Jim Sturm uses a method which combines rapid thermal processing and chemical vapour deposition (RTCVD). To date all samples have been grown on <100> Si substrates first subjected to a high temperature (1000 °C) hydrogen clean and growth of a

silicon buffer layer. The growth chamber consists of a quartz tube with a load lock for changing the wafers, which are suspended by quartz pins. The rapid thermal aspect of this set-up is provided by a bank of twelve 6 kW tungsten-halogen lamps located outside the quartz tube that can ramp the temperature at a rate of about 20-30 °C/sec. The SiGe CVD occurs by the decomposition of mixtures of dichlorosilane/hydrogen and germane/hydrogen gases at the hot (625 °C) wafer surface, resulting in the deposition of Si and Ge atoms, respectively. The nominal SiGe growth rate is about 80 Å/min. The Si layers are grown at a rate of about 30 Å/min, with the dichlorosilane/hydrogen carrier gas mixture and the wafer at 700 °C.

In between the growth of each SiGe or Si layer, the wafer temperature is directly switched from 625 to 700 °C (or vise-versa) at a ramp rate of 20 K/sec, and a total of 10-15 sec allowed for temperature stabilization and complete gas purging between each layer. The lower growth temperature for the SiGe layers arises from a fortuitous catalytic reaction of germane on silicon in the CVD growth [91Sb]. The ability to quickly ramp between optimum crystal growth temperatures for different layers is one advantage of RTCVD over conventional CVD [91Sb]. However, the temperature is not used to control the growth start and stop. Better quality layers are obtained using fast switching of the process gases, with only pure hydrogen flow during temperature ramps. Using this technique the interface control is quite good, transmission electron micrographs revealed an upper limit in interface abruptness of about 10 Å [91Sb].

Accurate control of the sample temperature during growth is essential to the success of the RTCVD. A method was developed by Jim Sturm to perform the measurements *in situ* based on the optical absorption of the Si substrate at 1.3 and 1.55 µm [91Sb]. At these wavelengths the absorption coefficients are almost exponential functions of temperature, so that the light transmitted provides a measure of the wafer temperature within a few °C. The growth of the thin SiGe layers has little effect on the transmission.

The research group at the National Research Council Canada uses the growth technique of molecular beam epitaxy (MBE), as described by Noël *et al.* [92Na] and references therein. For a review on Si-based MBE see the book edited by Kasper and Bean [88K]. In MBE a semiconductor film is grown by directing beams of atomic or molecular species onto a heated substrate under conditions of ultra-high vacuum (typically a base pressure of 10^{-9} mbar). The technique is basically a sophisticated form of vacuum evaporation. For SiGe MBE, the evaporation sources usually consist of solid Si and Ge which are carefully cleaned and etched before introduction into the chamber. The Si substrate is also cleaned and either oxide or hydrogen passivated. The passivation layer is then removed inside the chamber by heating to 600-900 °C before the growth starts. The growth rate is typically 1 Å/s, depending on the Ge flux. Because both Si and Ge have relatively low vapour pressures, the Si and Ge fluxes must be produced by electron beam evaporation. The need for electron beam evaporation complicates the growth because of the generation of secondary and reflected electrons, ionized species, and radiation.

One of the advantages of MBE over CVD techniques is the possibility of using a much lower growth temperature (~ 350 °C versus ~700 °C), which results in more abrupt interfaces between different layers. As well the growth is easily controlled by shutters on the Ge and Si sources. One problem is that doping of Si and SiGe by MBE has been found to be very difficult because the dopant atoms do not stick well to the surface. Another disadvantage is the relatively high cost of an MBE system. The MBE growth requires maintaining ultra-high vacuum conditions, as well as very careful cleaning of the evaporation sources and the substrates. It remains to be seen whether the advantages of MBE SiGe growth over CVD will be enough to compensate for the added sophistication, especially in a production environment. However, at present both techniques are being actively investigated. This thesis concentrates on RTCVD layers since band-edge PL from the MBE material was only achieved in the past year, while observations were made for the CVD material some two years earlier.

Chapter 4.

Results for Strained $Si_{1-x}Ge_x$

4.1. Introduction

Although well resolved band-edge PL was reported for unstrained SiGe some time ago [89Wb, 82M, 74B, 73G], we made the first observation of such PL for fully strained epitaxial SiGe in 1990 [91Sa]. Just prior to our study band-edge PL was reported for epitaxial SiGe, but only for samples with a very small Ge fraction (x=0.04) which may have been partially relaxed or for layers of higher Ge content that were completely relaxed [90Tb]. The deliberate introduction of deep level recombination centers also led to luminescence from strained SiGe [90M], however this technique gave little information about the energy gap or perfection of the SiGe layers. Although our first observations [91Sa] were made on thin SiGe layers in which quantum confinement effects were significant, this chapter concentrates on those features of the PL that are characteristic of the strained SiGe alloy layer itself. The consequences of the band offsets at the interface with the Si are then dealt with in Chapter 5.

Well resolved band-edge PL is now routinely observed for fully strained $Si_{1-x}Ge_x$ layers grown on Si by either chemical vapour deposition techniques (see for example Robbins et al. [92R], Vescan et al. [92V], Zollner et al. [92Z], or Dutartre et al. [91D]) or by molecular beam epitaxy (see for example Kennedy et al. [93K], Arbet-Engels et al.

[92A], Spitzer *et al.* [92Sa], Steiner *et al.* [92Sb], Terashima *et al.* [92T], or Usami *et al.* [92U]). The MBE SiGe was found, by our collaborators at the National Research Council [90N] and later by others [93G, 92D, 92Sa, 92Sb, 91T, 90H], to differ from that grown by CVD in that a broad deep PL band is often observed. The presence of this deep band is found to lead to very weak or absent near band-edge features. The MBE spectra are therefore treated here in a separate section (4.4), while the remainder of this chapter deals only with the PL from the RTCVD layers. Note that all of the SiGe samples used in this study have thin (100-200 Å) Si caps.

4.2. Free and Bound Exciton Photoluminescence

Figure 4.1 shows a typical PL spectrum for strained SiGe on Si. The features indicated in the low energy region are due to a 200 Å thick layer of RTCVD $Si_{0.8}Ge_{0.2}$. In addition to a no-phonon (NP) SiGe transition, we observe phonon-assisted transitions involving transverse acoustic (TA) phonons and three transverse optical (TO) replicas for Si-Si, Si-Ge, and Ge-Ge modes. The phonon energies, TA= 17.8 ± 0.5 meV, Si-Si_{TO}= 58.5 ± 0.5 meV, Si-Ge_{TO}= 50 ± 1 meV, and Ge-Ge_{TO}= 35 ± 1.5 meV, are in excellent agreement with the bulk SiGe results of Weber and Alonso [89Wb] described in section 2.2. The large arrows in Figure 4.1 indicate the Si and the $Si_{0.8}Ge_{0.2}$ band gap energies, where the strained SiGe band gap is determined from the PL data as outlined below.

The SiGe/Si PL spectrum also contains features originating from the Si substrate. This is not surprising because the visible Ar excitation should easily penetrate the relatively thin epitaxial layer(absorption coefficient ~1 μm) and so is mostly absorbed in the substrate. The substrate PL transitions correspond to well known Si BE and BMEC no-phonon transitions, with TA phonon replicas, TO phonon replicas, and two phonon
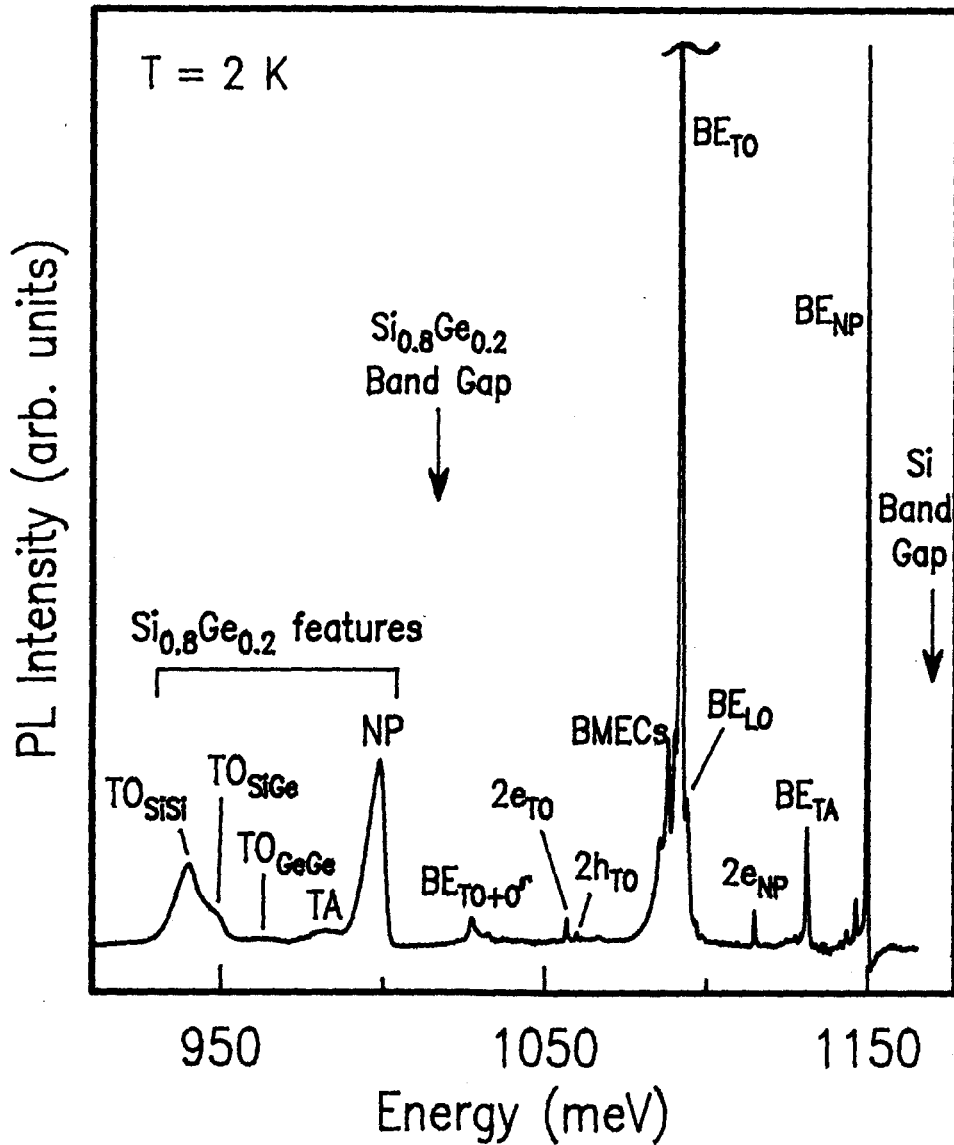
Figure 4.1 PL spectrum showing SiGe (x=0.2) and Si transitions at 2 K. The broad SiGe NP peak at 998 meV is accompanied by a TA replica and the Si-Si, Si-Ge, and Ge-Ge TO replicas to lower energy. BE and BMEC PL associated with phosphorus and boron impurities in the Si substrate is also observed. The arrows indicate the Si and SiGe band gaps, where the SiGe value was approximated as discussed in the text. The full height of the Si BE_{TO} (about 10x the Si BE_{NP} height) is not shown.

TO+O$^\Gamma$ (zone center) replicas. In this particular sample we observed BE luminescence due to both phosphorus and boron substitutional impurities. In addition to these principal Si BE transitions, the spectrum contains the corresponding two hole (2h) and two electron satellites (2e). These satellites occur when the electron and hole of the BE recombine, leaving the neutral donor or acceptor in an excited state. Since PL spectra of Si are dominated by shallow BE luminescence at liquid-He temperatures, even for very low donor or acceptor concentrations (>10^{13} cm^{-3}), it is expected that the same will be true for high quality SiGe. At low temperatures, BE luminescence dominates the PL spectra of the previous studies of bulk, relaxed alloys [89Wb,82M], as well as the spectra of the low Ge fraction (x= 0.04, 0.15) epitaxial layers grown by Terashima *et al.* [90Tb].

Although the SiGe layer is extremely thin, it gives a signal having integrated intensity comparable with that of the much thicker substrate. This may result from migration of free excitons originally generated in the substrate to the lower band gap region of the SiGe layer before recombination. In bulk SiGe the diffusion of excitons to the regions of lower band gap was also thought to occur, because no shift in the PL lines was observed despite scanning the excitation beam over regions having varying Ge composition [89Wb]. The integrated intensities of the SiGe PL signals detected in this study are typically greater at 4.2 K than that of the Si even for a single 100 Å SiGe layer. Increasing the number of SiGe layers or their thickness seems to have little effect on this signal intensity. This is consistent with the expectation that, unless the overall SiGe thickness is increased significantly, most of the excitation will still pass through the epitaxial layers and continue to be predominantly absorbed in the substrate as before. This is discussed further in the section on the SiGe/Si tunneling structures (section 5.5)

Evidence of the shallow-BE origin of the SiGe transitions is obtained by a careful study of the PL with increasing temperature. Because typical shallow BE binding energies are of the order of a few meV in Si [82T] and bulk SiGe [89Wb,82M], the FE line is difficult to resolve from the alloy broadened BE line in the SiGe. Figure 4.2 shows our

47

best results with resolved BE and FE peaks clearly discernable in the NP region at 16 K. These spectra were taken from a sample consisting of a 100 Å Si $_{0.8}$Ge$_{0.2}$ layer, with Ge concentration on either side linearly graded over 500 Å from 13% to the Si substrate and 150 Å Si cap. Similar results were obtained with other SiGe samples [91S], although the peaks were not as clearly resolved as in this particular sample. Below about 10 K the spectra are relatively independent of temperature, but at roughly 12 K the FE peak starts to become obvious, and it dominates the spectrum by 20 K. This is characteristic of unbinding of the excitons from the shallow impurities as they acquire thermal energy from the lattice, with a subsequent decrease in the SiGe BE and increase in the SiGe FE signal. As well, the bound excitons in the Si dissociate from the impurities at higher temperatures so that more free excitons find their way from the substrate to the SiGe regions. The Si signal therefore drops, while the SiGe (BE+FE) PL is found to typically increase by a factor of nearly five between 4.2 K and 77 K. The SiGe PL is observed at temperatures of up to 170 K for x=0.25.

The SiGe FE peak has the characteristic asymmetrical Maxwell-Boltzman line shape at high temperatures. The crosses in Figure 4.2 are the best fit to the 25 K data obtained by using a Maxwell-Boltzmann function:

$$I(E) \approx (E - E_{gx})^{\frac{1}{2}} e^{-\frac{E-E_{gx}}{kT}} \tag{4.1}$$

which was convolved with a Lorentzian lineshape to account for the broader linewidths observed in the alloy (see discussion below on the alloy broadened BE linewidths). The $(E-E_{gx})^{1/2}$ pre-factor accounts for the energy dependence of the density of states relative the zero momentum FE (i.e. the excitonic band gap, E_{gx}). The fit shown in Figure 4.2 corresponds to a temperature of 25.1 K and a FE edge of 938.6 meV. From the position of the BE at 5 K (934.7 meV) the BE binding energy is therefore 3.9 meV, in good agreement with shallow-BE binding energies in Si and in bulk SiGe alloys [82M].

48
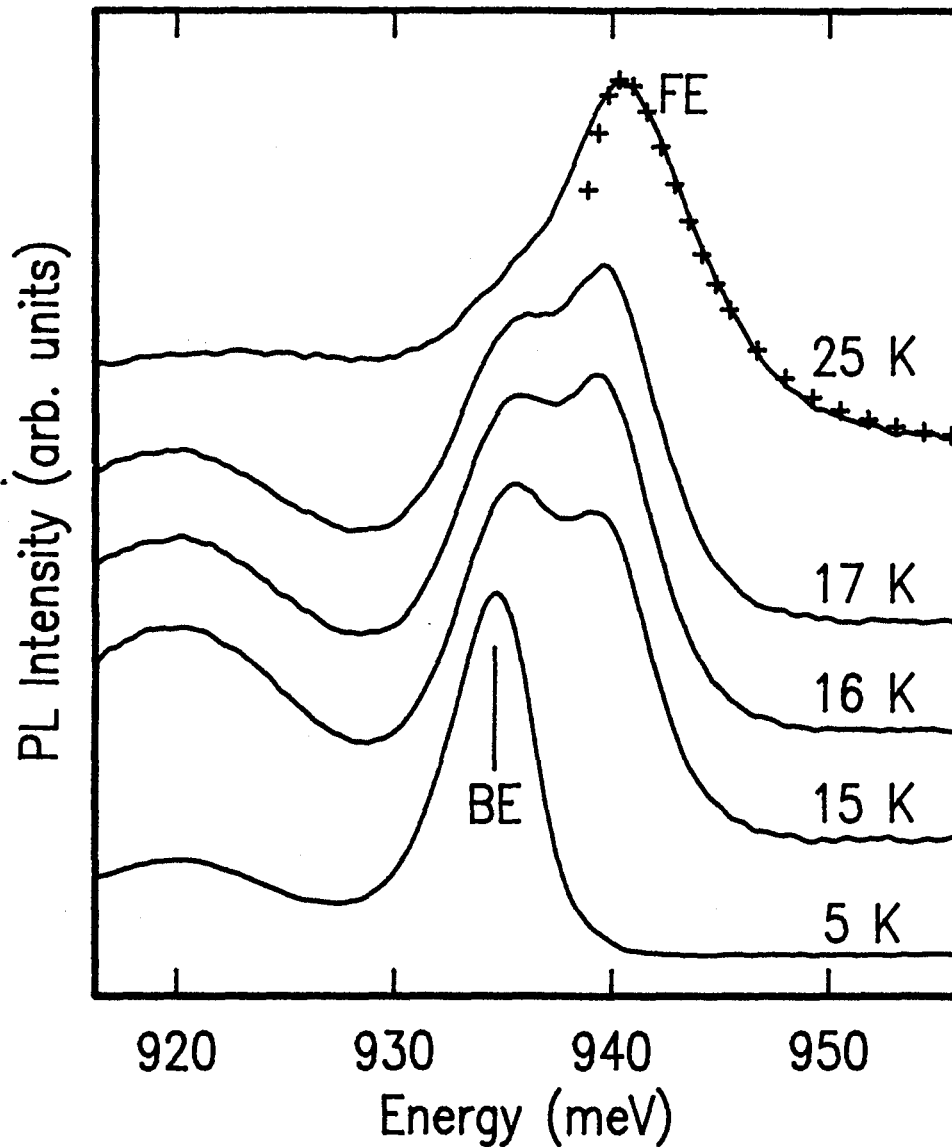
Figure 4.2 NP PL peak for a 100 Å $Si_{0.75}Ge_{0.25}$ layer with Ge content graded to the Si substrate and cap, as described in the text. The PL evolves from BE luminescence at low temperature (5 K) to FE luminescence at high temperature (25 K), with both the FE and BE peaks apparent at 15-17 K. The crosses show the best fit to the expected asymmetrical Maxwell-Boltzmann line shape for the FE. The PL spectra were taken under identical excitation conditions and were scaled to give equal peak intensities.

Resolved FE/BE features in SiGe with peak separations of 4 meV, 3.5 meV, and 3.6 meV were also reported at liquid He temperatures by Robbins *et al.* [92R], Wachter *et al.* [92W], and Spitzer *et al.* [92Sa], respectively. In addition, the characteristic Boltzmann tail was confirmed to occur at high temperatures for the peak attributed to FE luminescence by Spitzer *et al.* [92Sa] and Dutartre *et al.* [91D]. However, as will be discussed in Section 5.3, <u>at liquid He temperatures</u> the FE feature probably does not arise from strictly 'free' excitons, but rather from excitons somewhat localized by potentials arising from Ge-rich regions in the lattice.

To further support the FE/BE assignment of these features, we have measured the photoluminescence excitation (PLE) spectrum of the TA-phonon replica of the SiGe BE as shown in Figure 4.3 (curve e). Recall that in PLE the PL signal is monitored at some particular fixed energy, in this case the peak of the TA replica, while the excitation source is scanned in wavelength. These measurements were taken on a multiple quantum well sample consisting of 50 periods of 23 Å $Si_{0.8}Ge_{0.2}$ /23 Å Si. However the quantum well nature of this structure should not affect the results discussed here. Unlike the case for direct-gap heterostructures, in indirect-gap systems such as this the PLE spectrum of the FE is not expected to show peaks, but rather an absorption edge below which the response is zero and above which the response climbs monotonically. This is because the indirect absorption process must involve the simultaneous emission or absorption of a phonon or scattering from alloy fluctuations. In direct gap materials the optical transitions resonantly create 'zero' momentum excitons. Note that there is a complete absence of any response when the laser is scanned over the position of the low temperature BE line in Figure 4.3 (curve e), in agreement with the fact that BE absorption is extremely weak in indirect-gap materials. The clearly defined absorption edge observed in the PLE data at 1047.3±1.5 meV corresponds well to the location of the FE PL edge at 1046.1 meV in Figure 4.3 (curve d).
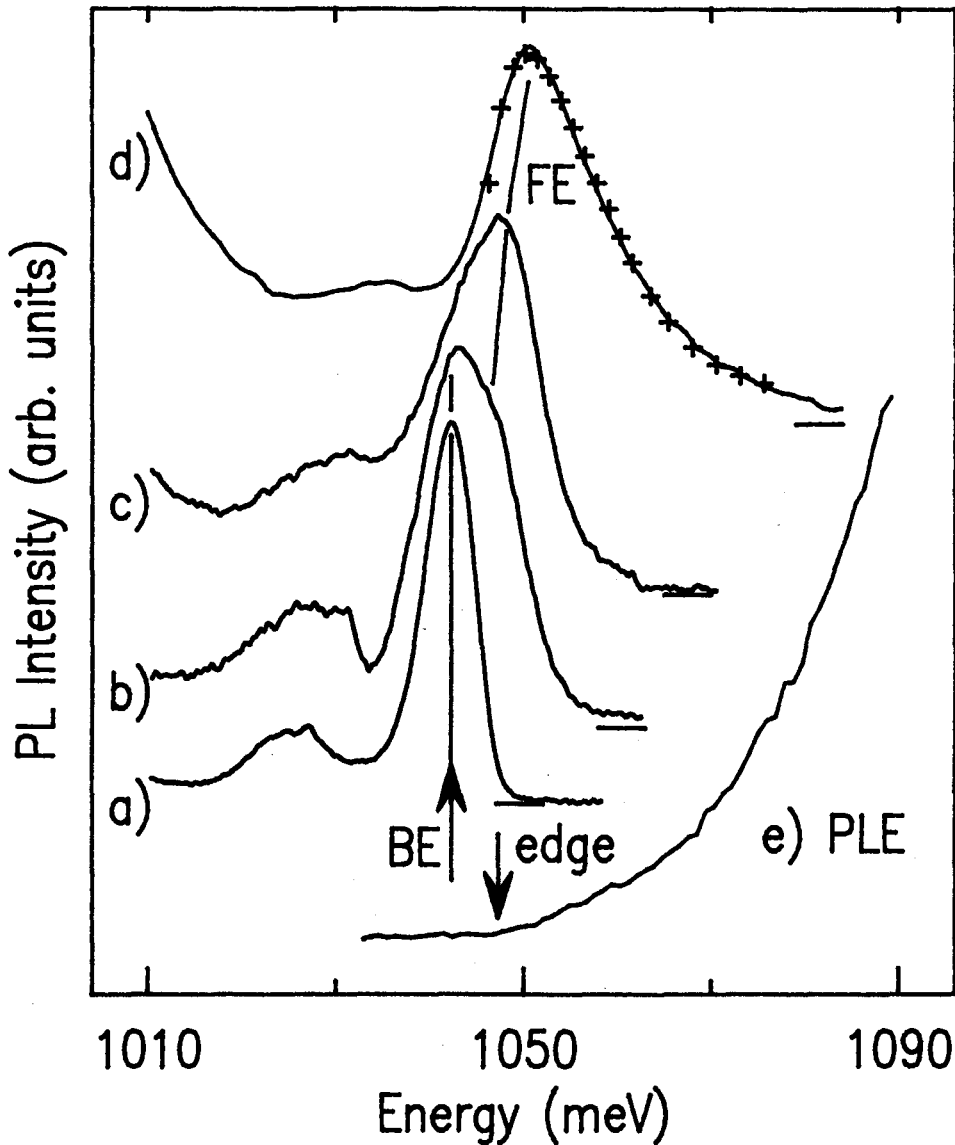
Figure 4.3 Curves (a-d) show the NP PL at T=4.2, 18, 24, and 60 K, respectively, for a MQW sample consisting of 50 periods of 23 Å $Si_{0.8}Ge_{0.2}$ /23 Å Si. The crosses are the best fit to the expected asymmetrical Maxwell-Boltzmann line shape for the FE. Curve (e) shows the PL excitation spectrum of the TA replica of the BE PL. The observed absorption edge in the PLE spectrum agrees within experimental uncertainty with the FE edge obtained from a fit to the PL (crosses). The PL spectra were taken under identical excitation conditions and were scaled to give equal peak intensities.

The PL time decay in the SiGe samples at low temperature is also similar to that of known shallow BE recombination processes in Si or Ge. Figure 4.4 compares luminescence decay curves for two different SiGe samples, with those for BE PL associated with B and P in the Si substrate. The decay curves yield PL lifetimes of 1.0 μs and 375 ns for a 200 Å $Si_{0.86}Ge_{0.14}$ quantum well sample and for the $Si_{0.8}Ge_{0.2}$ MQW sample (see Figure 4.3 for complete sample description), respectively. These values are similar to the shallow BE lifetimes in pure Si, such as the 1 μs lifetime for boron BE and 325 ns for phosphorus BE. From the similarity in the decay curves it is tempting to conclude that the SiGe PL also originates from boron BE in the $Si_{0.86}Ge_{0.14}$ sample and from phosphorus BE in the $Si_{0.8}Ge_{0.2}$ MQW. However, at present there is no other evidence available to support this supposition. Further experiments in which the SiGe will be intentionally doped with impurities are planned.

An indication that the situation may in fact be more complicated than Figure 4.4 leads us to believe, is the observation of decay curves from other SiGe samples which are non-exponential and excitation power dependent. This suggests the presence of more than one component in the BE spectrum. However, the measured lifetimes in all of the samples are consistently in the range of ~ 1 μs, implying that even though it is difficult to interpret these decay curves precisely, the recombination processes are such that nonradiative channels compete with radiative ones. This might include the presence of different BE, or possibly biexcitons in addition to the BE.

Figure 4.5 compares the SiGe features in three samples having SiGe layers with nominal Ge fractions of a) x= 0.14, b) 0.2, and c) 0.35. As expected, the PL shifts to lower energy (i.e. towards the transition energies for pure Ge) with increasing Ge fraction. Comparing the relative phonon peak intensities there is also an increase in intensity of the PL associated with Si-Ge and Ge-Ge TO modes relative to the Si-Si TO peak with increasing Ge fraction. The ratios of the Si-Si to the Si-Ge peak intensities are plotted versus Ge fraction for the three samples in the inset of Figure 4.5. (The Ge-Ge peak

52
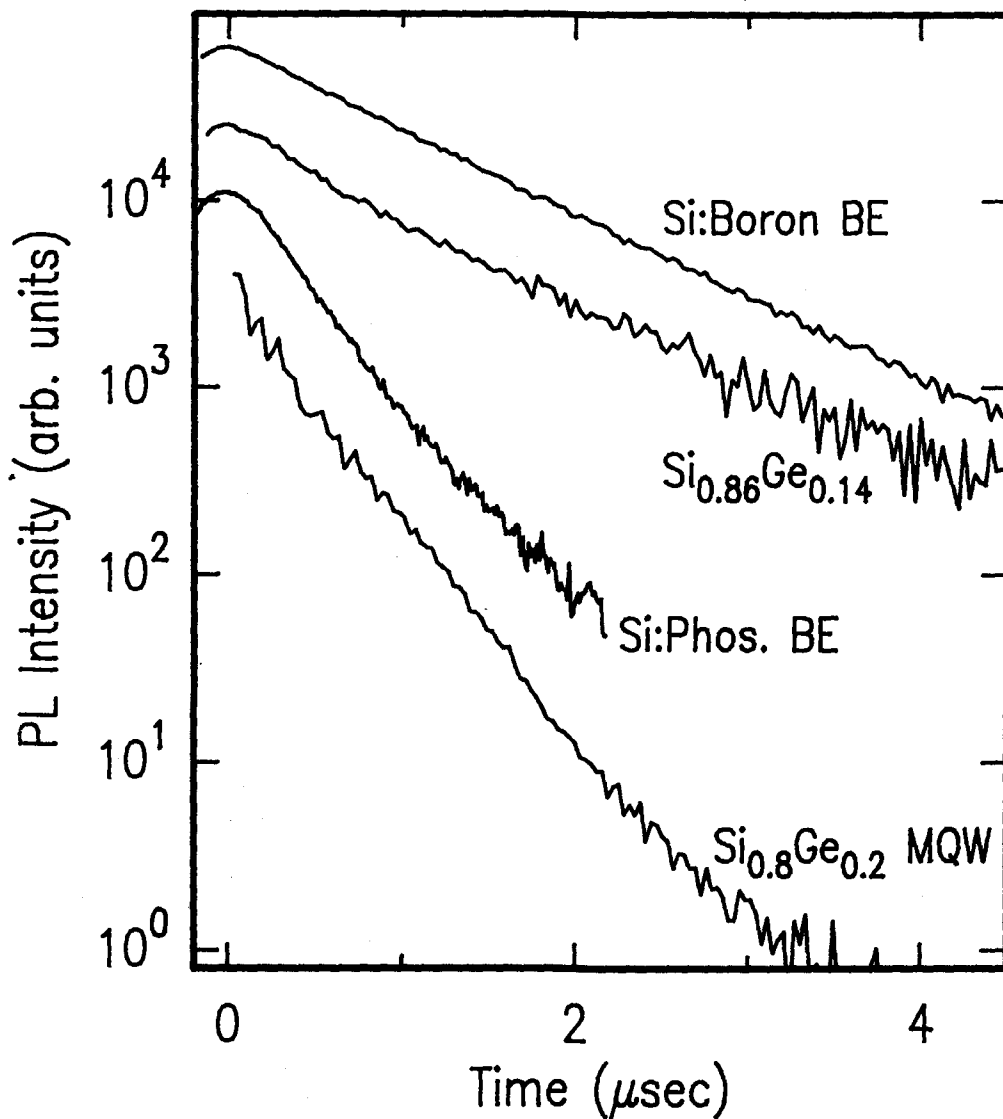
Figure 4.4 Time decay of the PL intensity at liquid He temperatures for BE luminescence as indicated from boron doped and phosphorus doped Si substrates, from a 200 Å $Si_{0.86}Ge_{0.14}$ layer, and from the $Si_{0.8}Ge_{0.2}$ MQW sample of Figure 4.3. The curves have been shifted vertically for clarity.
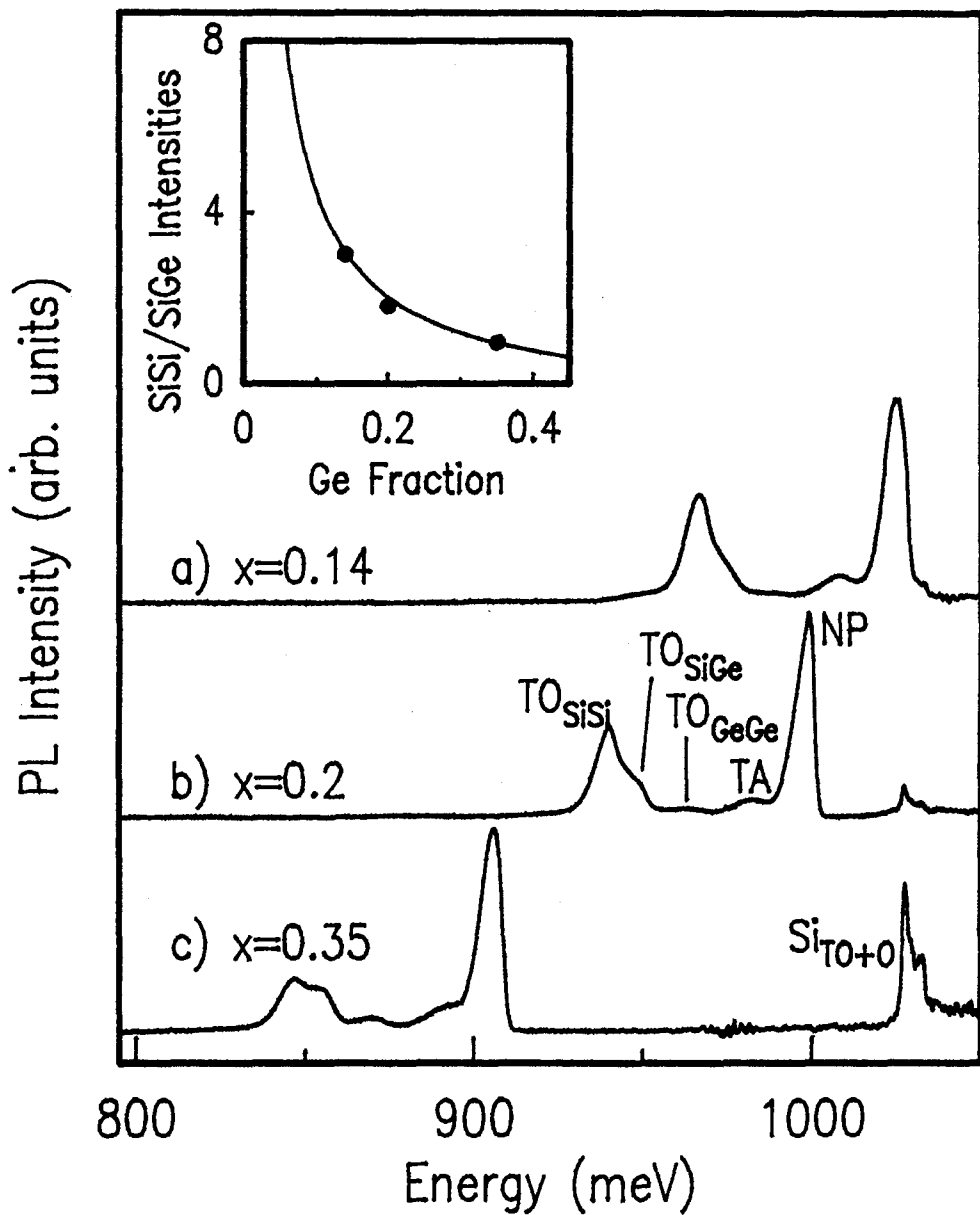
Figure 4.5 Band edge PL spectra at 2 K for SiGe layers with nominal Ge fractions of x = a) 0.14, b) 0.2 and c) 0.35. The PL intensities have been scaled to give equal SiGe NP peak heights. The spectra shift towards lower energy with increasing x, consistent with the expected decrease in the SiGe band gap. The intensities of the Si-Si peaks relative to the Si-Ge peaks are compared with the predicted ratios for a random lattice (equation 2.2) in the inset.

intensities are not shown since the features were too weak to obtain reliable estimates.)
There is good agreement with the prediction of equation 2.2, as shown by the solid line.
In other words, the relative phonon intensities are proportional to the probability of Si-Si
or Si-Ge pairs for a random distribution of Ge in the lattice. The NP intensity is also
observed to increase relative to the phonon replicas with increasing x, consistent with the
expected increase in scattering by alloy fluctuations.

The ability to observe band edge photoluminescence in this material is important
since it provides us with a convenient means of finding the strained alloy band gap.
Similar measurements were used by Weber and Alonso [89Wb] for unstrained SiGe (see
Figure 1.2). The excitonic band gap can be determined from the energy of the no-phonon
BE peak in the PL data by adding the BE binding energy. The BE binding energy is
assumed here to be the same as for shallow impurites in Si (~4 meV). Note that this gives
the 'excitonic' band gap, which is shifted to lower energy relative to the actual band gap by
the ~ 15 meV FE binding energy. The results for a number of our RTCVD samples are
shown as a function of the Ge fraction in Figure 4.6 (solid circles). Our values compare
favourably with the PL data of several other research groups, as shown for Arbet-Engels
et al. [92A], Robbins et al. [92R], Spitzer et al. [92Sa], Zollner et al. [92Z], Dutartre et
al. [91D], and Terashima et al. [90Tb]. The estimated uncertainty in our sample
compositions from the nominal values of $\pm$ 10% (i.e. Ge fraction is $x_{nominal} \pm 0.1$
$x_{nominal}$) is shown by the error bars in the figure for a couple of our data points. In all the
other cited studies each sample composition was confirmed individually by Rutherford
backscattering and/or double crystal X-ray diffraction, so the expected error in
composition is smaller. The energy error bars show an uncertainty in the band gap
energies of $\pm$ 5 meV. This uncertainty accounts for an ambiguity of a few meV which
arises from the interpretation of the NP peak as due either to BE or to FE recombination.
We took at face value the claim of some other research groups that they are observing FE
directly and not BE recombination, even at low temperatures. In addition, some of our

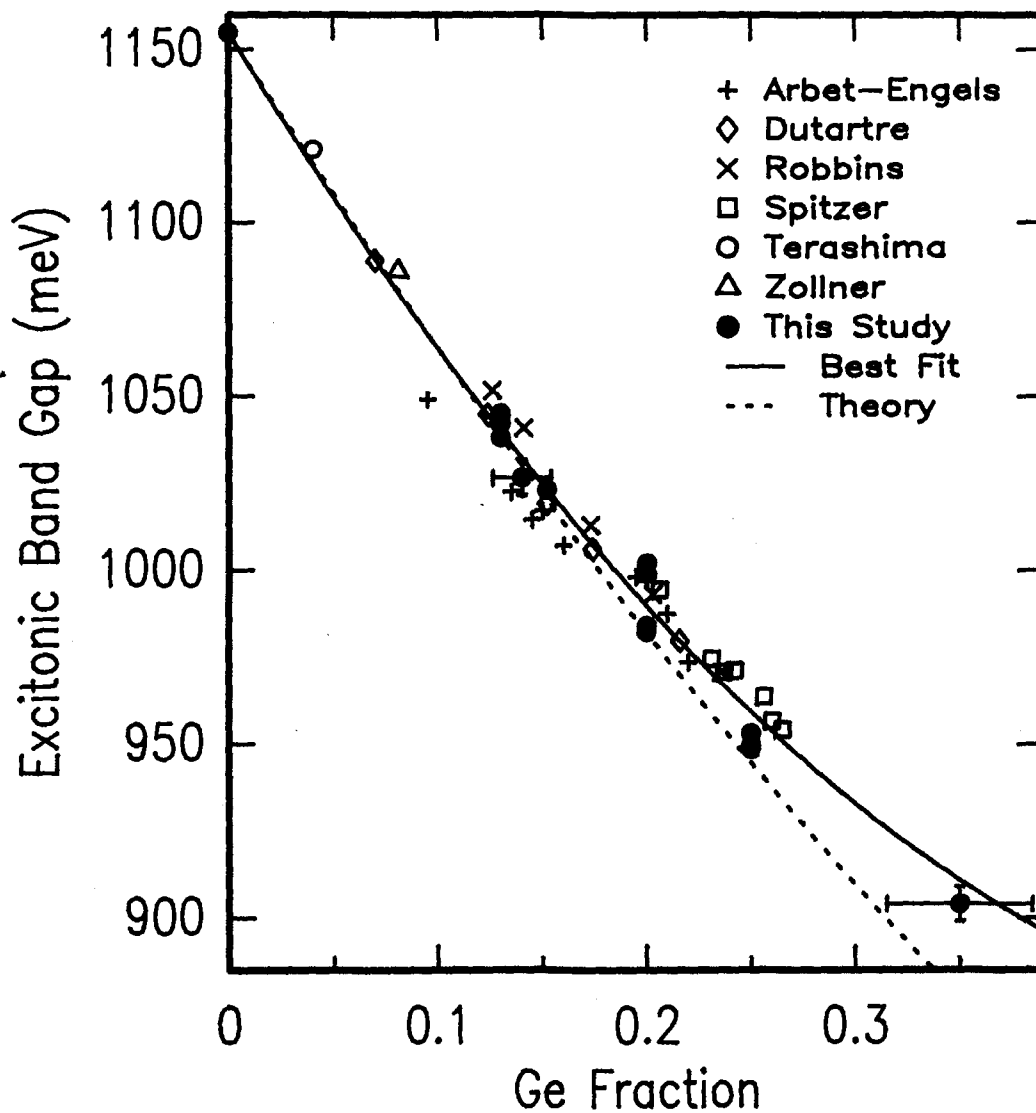**Figure 4.6** Excitonic band gap at liquid He temperatures as a function of Ge fraction. Obtained by adding the estimated BE binding energy (4 meV) to the BE NP energy observed in the PL. The solid line shows the best polynomial fit to the data, including data points from various other research groups, as indicated. The dashed line shows the results of the deformation potential theory calculation described in section 1.2 [85L].

data was taken from relatively thin (100 Å) SiGe layers and therefore had to be shifted by 5 meV to account for quantum confinement effects (see next chapter).

The solid curve shows a best fit to all the experimental data points simply using a polynomial:

$$E_x(x) = 1155 - 965x + 840x^2 \qquad \text{(in meV)} \qquad (4.2)$$

This equation provides a convenient means of either predicting the excitonic band gap for a given composition (and hence inferring the actual band gap by adding the FE binding energy) or conversely of extracting the sample composition simply from a PL spectrum. The experimental curve agrees well with the theoretical curve (dashed line) which was calculated using the deformation potential theory described in section 1.2 [85L]. The better agreement at low x is not surprising since any errors in the parameters of the theoretical calculation becoming increasingly important with increasing strain. The departure from the theoretical curve at high x may also originate in the non-linear effects expected at very high strain.

The broadening of the BE peaks in SiGe compared to Si can be accounted for by following the procedure discussed in section 2.2 for bulk SiGe. Most of the broadening is assumed to occur due to smearing of the band-edges, while variations in the exciton binding energies are neglected. Then the random variation in x leads to equation 2.3 for the PL linewidths with the appropriate substitution of dE_g/dx for strained SiGe from equation 4.2. Rather than using the Bohr radius as a fitting parameter (as in Weber and Alonso [89Wb]), an estimate can be obtained from the usual expression:

$$a_b = \frac{\varepsilon_r \hbar^2}{\mu_0 e^2} \qquad (4.3)$$

where a linear interpolation between Si and Ge values can be used for the dielectric constant ε_r. For the exciton effective mass μ_0 we use the expression given by Robbins *et al.*, $m_0/\mu_0 = (2/m_t + 1/m_l + 3\gamma_1)/3$, where Si values are used for the electronic masses and the Luttinger parameter γ_1 is given by a linear interpolation between Si ($\gamma_1 = 4.22$) and Ge (γ_1

= 13.35) [92R]. The predicted Bohr radius values (from equation 4.3) and corresponding PL linewidths (from equation 2.3) are contrasted with the observed values in Table 4.1. The predicted Bohr radius increases from 59 Å, to 64 Å, and 76 Å, for x increasing from 0.14, to 0.2 and 0.35, respectively. Substituting into equation 2.3, gives expected alloy broadened PL linewidths of 2.8 meV, 2.5 meV, and 1.4 meV for Ge fractions of 0.14, 0.2, and 0.35 respectively. Our observed NP linewidths (i.e. FWHM) for the three RTCVD samples of Figure 4.5 are 7.8 meV for x=0.14, 6.3 meV for x=0.2, and 6.5 meV for x=0.35. Other authors have observed slightly narrower linewidths (i.e. 3 meV for x=0.15 [92R] and 3.5 meV for x=0.24 [92Sa]), and we also have observed FWHM as small as 1.8 meV in several MBE MQW SiGe samples.

While the predicted linewidths are clearly smaller than the observed values for the RTCVD material, the alloying effects account for most of the PL line broadening in comparison to the very narrow μeV Si BE linewidths. The linewidth calculation is

Table 4.1 BE PL Linewidths

	Predicted a_b	Predicted FWHM	Observed FWHM	"Observed" a_b
200 Å $Si_{0.86}Ge_{0.14}$	59	2.8	7.8	31
200 Å $Si_{0.8}Ge_{0.2}$	64	2.5	6.3	35
100 Å $Si_{0.65}Ge_{0.35}$	76	1.4	6.5	28
77 Å $Si_{0.85}Ge_{0.15}$ MBE	60	2.8	1.8	82
500 Å $Si_{0.85}Ge_{0.15}$	60	2.8	3[a]	58
500 nm $Si_{0.76}Ge_{0.24}$	67	2.2	3.5[b]	51

Bohr radius values in Å, linewidths in meV. "Observed" Bohr radius values were found using equation 2.3 and the observed linewidth values.

a From Robbins *et al.* [92R]

b From Spitzer *et al.* [92Sa]

sensitive to the estimate of the Bohr radius, for example a value of 35 Å instead of 64 Å gives agreement between the predicted and the observed linewidth of 6.3 meV for x=0.2. Although this is nearly a factor of two difference, both values are reasonable in comparison to $a_b \sim 49$ Å for Si and $a_b \sim 140$ Å for Ge. The calculation of a_b described above might need to be examined more carefully. There is also a great deal of scatter in the experimental values themselves. This may be due to some broadening introduced by inhomogeneity in the Ge concentration though the SiGe layer. Evidence that this may in fact be the case, is the observed broadening of the BE peaks for the RTCVD material to higher energy under conditions of high excitation, which is consistent with the expectation that the excitons first fill the regions of small band gap (i.e. Ge-rich regions) and as their number increases begin occupying regions of larger band gap.

4.3. Excitons Localized by Alloy Fluctuations

Studies in the epitaxial Si-Ge alloy system have been partly motivated by the possibility of Si based optoelectronics through the quasi-direct band gap predicted for atomic layer superlattices. However, our PL studies on SiGe alloys have inadvertently led to the discovery of a highly efficient luminescence process (> 10% quantum efficiency) which suggests an alternative means of achieving good optical properties in a Si based technology. Under low excitation power density the near band gap BE and FE PL described in the previous section decreased in intensity to reveal this new PL mechanism. We attribute this highly efficient PL to an intrinsic process in which FE become localized on random fluctuations of the alloy composition which are purely statistical in nature.

The random nature of the SiGe alloy manifests itself in the band edge PL of both bulk [82M, 89Wb] and strained layers as a broadening of the PL peaks, and a relaxation of

the usual wave vector conservation rules to give strong NP transitions despite the indirect band gap. Another consequence of the statistical fluctuation in Ge concentration is the formation of regions rich in Ge, which can act as potential wells for holes. This can be described within the framework of Anderson localization, which occurs for a random distribution of potentials (here due to Si or Ge atoms) on fixed lattice sites [58A]. The disorder leads to a tail in the density of states that extends into the forbidden gap (see Figure 4.7). The density of states tail has been shown to take the form of an exponential dependence on energy (see for example the review on band tailing in the book by Böer [90B] or the localized state references given below). A characteristic energy known as the mobility edge distinguishes between localized states and the extended states of the crystal. If the radiative rate of the localized excitons is slow, then before recombining they can tunnel or thermally hop to other lower energy localized states. At low temperatures, where the mobility edge is high in energy, the excitons can therefore become immobilized many kT below the mobility edge. Note that the conduction band edge in SiGe remains at
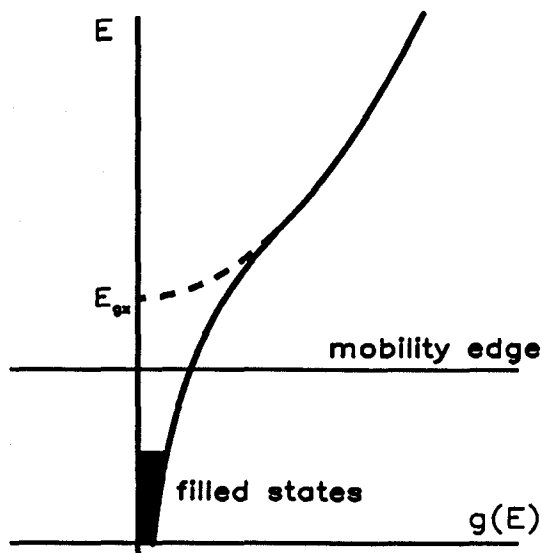

Figure 4.7 Density of states tail for free excitons due to alloy disorder. The excitons can tunnel or thermally hop to the deepest localization centers, as shown by the shaded region. At low temperatures the highest occupied state can lie far below the mobility edge.

nearly the same level as in pure Si , so we expect that the electron does not directly feel the localization potential, but is bound to the localized hole by Coulomb attraction.

Localized states have been experimentally observed in other semiconductor alloys, including $GaAs_xP_{1-x}$ [89F, 86G, 85O, 84L, 84S], CdS_xSe_{1-x} [82C], and $Ga_{1-x}Al_xAs$ [83S], however it was not recognized that such localization can lead to high radiative efficiency despite an indirect band gap or low oscillator strengths. While Permogorov *et al.* [82P] mention the possibility of improved efficiency due to localization in CdS_xSe_{1-x}, they neglect to provide any direct measurements to support this supposition. In this section, evidence will be presented to demonstrate that the new PL process in our SiGe/Si samples is consistent with localization by alloy fluctuations, and that this leads to the observed high quantum efficiency.

We observed the new PL process in a wide variety of single and multiple quantum wells of RTCVD SiGe on Si. While many samples were studied and found to show similar PL features, the work reported here concentrates on the sample whose spectrum was shown as a function of temperature in Figure 4.2. Recall that it consists of a single 100 Å $Si_{0.75}Ge_{0.25}$ layer, with 500 Å thick linearly graded ramps on either side decreasing from $x = 0.13$ at the well edges to $x = 0$ in the Si cap and substrate. Figure 4.8 shows five PL spectra of this sample at different excitation levels. At high pump power, 3.2 W cm^{-2} (Figure 4.8 a), the SiGe PL features are identical to those discussed earlier, with a strong BE no-phonon peak, a TA replica, and three TO replicas corresponding to Si-Si, Si-Ge and, Ge-Ge phonons. As the power density is reduced, a new broader and more asymmetrical PL system appears, whose NP peak emerges from beneath the BE TA replica. At very low excitation levels the SiGe BE lines vanish (as do the Si substrate PL lines), leaving only the NP and TO replica of the new process, which is labelled LE_{NP} and LE_{TO} for 'localized exciton'. The peak of the LE_{NP} line at relatively low excitation lies about 14 meV below the BE_{NP} line position. In other samples, covering $x = 0.14$ to $x = 0.25$, the LE - BE separation was found to vary from 12 to 25 meV. It is difficult to find

61
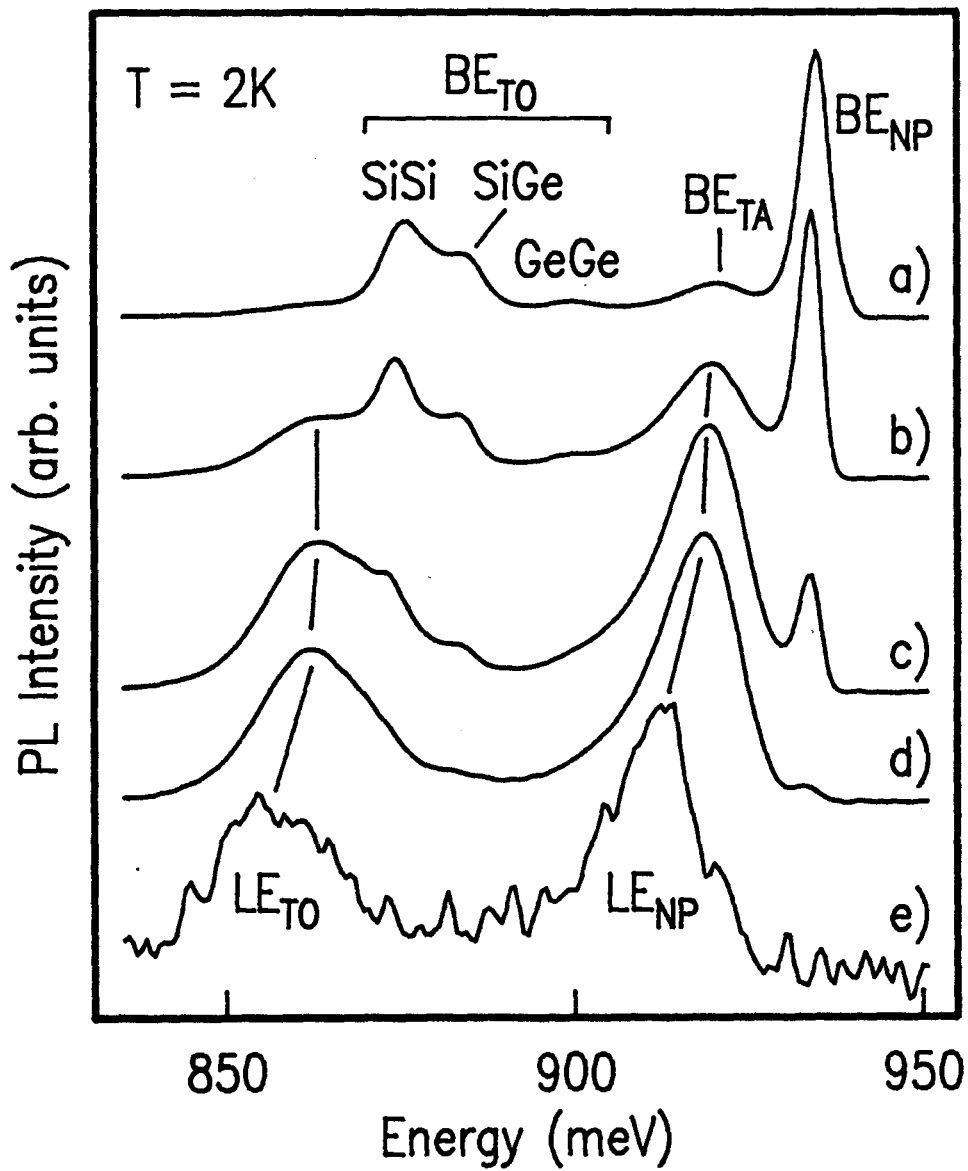
Figure 4.8 Emergence of LE NP and phonon replica PL from beneath the BE features under conditions of low excitation power density. PL spectra taken at excitation power densities of a) 3.2 W cm^{-2}, b) 0.32 W cm^{-2}, c) 30 mW cm^{-2}, d) 2.3 mW cm^{-2}, and e) 2.4 μW cm^{-2}. The PL intensities have been scaled to the BE peak in a), b), and to the LE peak in c), d), and e).

any systematic relationships among these peak positions since, as discussed below, the LE peak shifts by as much as 6 meV with excitation density. However, there does appear to be a dependence of the LE binding energy on SiGe thickness, which will be discussed in the next chapter.

The similar ratio of the NP peak intensity to the phonon replica intensities for the LE in comparison to the BE PL suggests that the LE NP process also results mainly from alloy scattering. This is consistent with the diffuse, shallow nature of potential wells expected for localization due to concentration fluctuations. A binding energy similar to that of the LE but resulting from a shorter range potential, for example an impurity central cell potential, would lead to a much stronger no-phonon intensity than is seen for the shallow BE PL.

The LE PL lineshape is asymmetric, having a low energy exponential tail and relatively sharp high energy cutoff which shifts to higher energy with increasing excitation density. This is shown more clearly in Figure 4.9, where the PL signals have been normalized to give equal intensity in the low energy tail, and a semi-log plot is used to emphasize the exponential lineshape having a 1/e slope of $E_0 = 9.1$ meV as indicated. The sharp high energy cut-off has been found to be characteristic of LE PL in other systems [89F, 85O, 84L, 84S, 82C]. The shift in the LE high energy edge with increasing excitation density is consistent with a gradual filling of potential wells with excitons, beginning with deep but relatively scarce wells at very low power, to shallower more abundant wells at higher power. This filling occurs, as described above, as localized excitons tunnel or hop to nearby localization centers until they reach the lowest available center. The exponential tail to low energy is also typical of the LE PL described for other alloys in the literature. It is thought to reflect the approximately exponential dependence (shown in Figure 4.7) of the density of states tail on energy [89F, 85O, 82C].

The strong excitation dependence of the PL intensities evident in Figure 4.8 is shown in more detail in Figure 4.10, which compares total integrated PL intensity as a
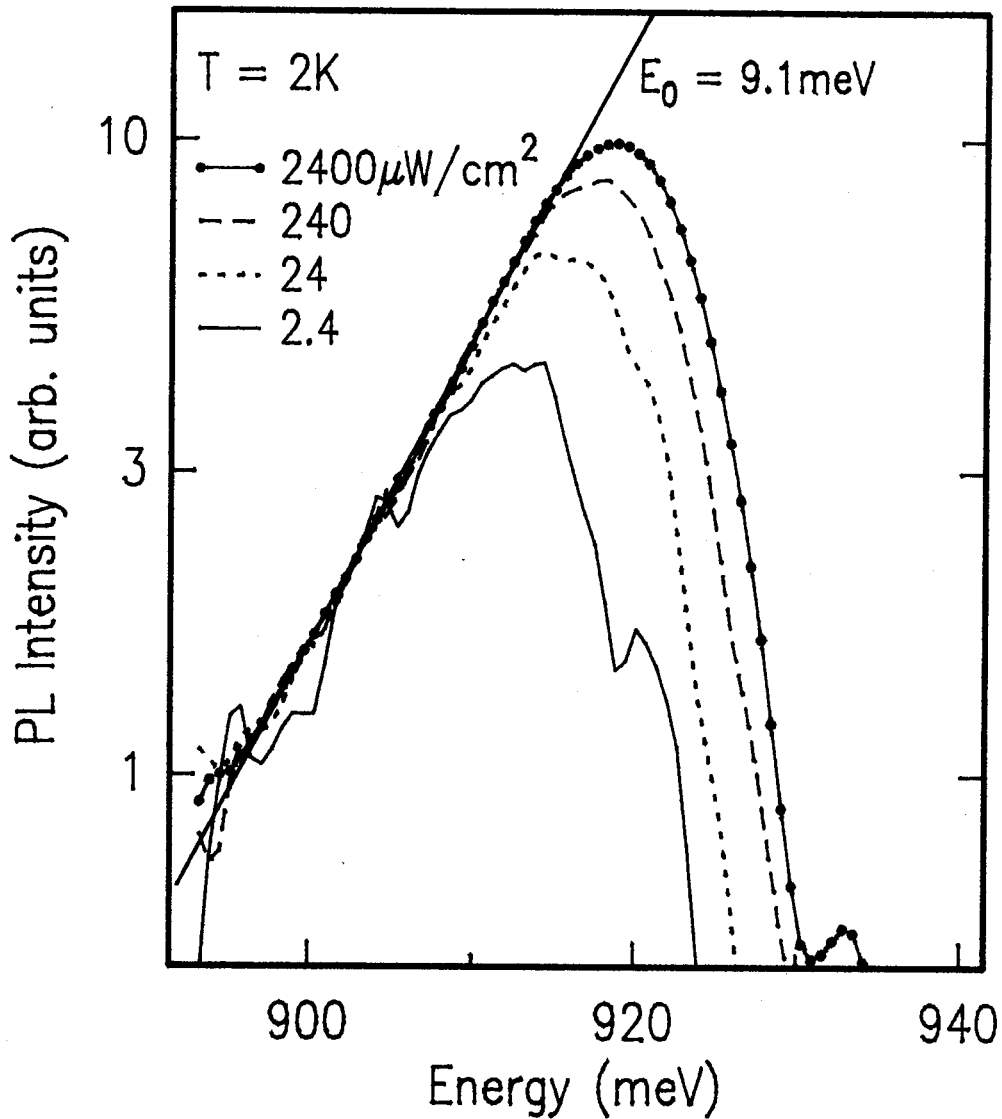
Figure 4.9 SiGe LE lineshape dependence on excitation power density. The low energy side is found to decrease exponentially as a function of energy, with a 1/e slope of 9.1 meV, as indicated. The high energy edge shifts to higher energy with increasing excitation. The PL spectra have been normalized to give equal intensity in the low energy tail.

function of excitation density for the SiGe LE, SiGe BE and Si substrate BE. At power densities between 10 and 500 mW cm^{-2}, where the SiGe LE and BE peaks overlap, the integrated intensities were estimated using peak heights. Both the SiGe BE and substrate BE PL show a nearly linear dependence, PL intensity $\propto$ [excitation density] ^{m}, with m ~ 0.95 for the Si BE and m ~ 0.84 for the SiGe BE, which is expected for a bound exciton process. The LE intensity on the other hand shows strong saturation at very low excitation densities, and only approaches a linear dependence at the very lowest excitation levels we could investigate, < 10 μW cm^{-2}. This is consistent with the LE model, since at low excitation levels each potential fluctuation contains at most one exciton, and the recombination is expected to be radiative. However, as the excitation density is increased, the chances of having more than one exciton in a fluctuation (i.e. biexcitons) increases, so that Auger recombination will be favoured relative to radiative recombination. In this process, the energy from the exciton recombination is taken up by one of the remaining carriers, which is thus left in a highly excited state. This saturation behaviour has been observed in other alloy LE PL studies [85O, 84L, 84S, 83S, 82P]. A similar effect has also been observed for an isoelectronic impurity BE in Si which can bind one or more excitons [86Tb].

It is evident from Figure 4.10 that the LE PL intensity is about 1000 times stronger than that obtained by extrapolating the Si BE or SiGe BE PL intensities down to a μW cm^{-2} excitation level, where only the LE is still experimentally observable. To investigate this interesting possibility, the external PL quantum efficiency of the sample was measured using the gold-coated integrating sphere as outlined in Chapter 3. We found a SiGe LE quantum efficiency at an unsaturated excitation density (12 μW cm^{-2}) of 11.5 ± 2 %, several orders of magnitude higher than is typically seen in Si.

This high quantum efficiency is consistent with an LE model, while being very difficult to reconcile with typical impurity or defect related processes. The high quantum efficiency of this process directly follows from the exciton confinement. Due to the

65
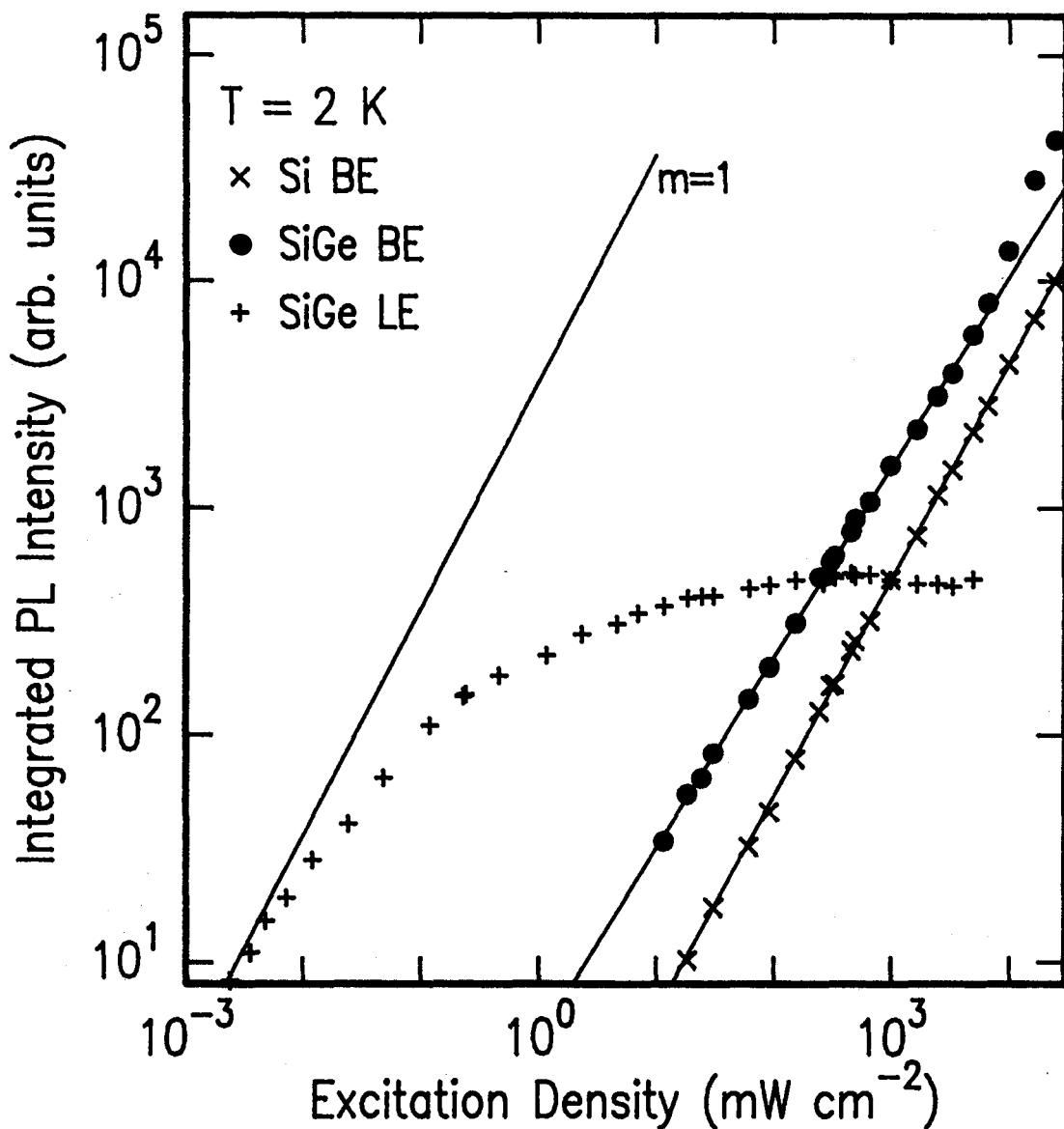
Figure 4.10 Integrated PL intensity as a function of excitation power density for the Si substrate BE (x), SiGe BE (●), and SiGe LE (+). Between 10 and 500 mW cm^{-2} the NP peak intensities were used to approximate the SiGe BE and LE integrated intensities. Nearly linear power dependences, $I \propto P^m$, m ~ 0.95 and m ~ 0.84 are obtained for the Si BE and SiGe BE, respectively. The LE PL follows the indicated m=1 line at very low powers, but begins saturating at about 10 μW cm^{-2}.

indirect band gap the free exciton has a long radiative lifetime in Si (~ 1 ms, [80H]) or SiGe. This means that the free excitons migrating through the crystal are likely at some time to encounter an impurity, so that nonradiative channels normally dominate over intrinsic recombination even in the highest purity Si. Comparing the 1 ms radiative lifetime with a typical nonradiative lifetime of 1 μs, a free exciton is 1000 times more likely to undergo a nonradiative transition than a radiative one. On the other hand, the likelihood of an LE being in the vicinity of an impurity, and thereby undergoing a nonradiative Auger transition is almost negligible. For example, if we assume a reasonable localization radius of 50 Å and typical doping level of 10^{16} cm^{-3}, the probability of finding an impurity within the LE volume is only 0.5 %. Thus the majority of the LE are expected to decay radiatively, albeit with a very slow transition rate.

Time-resolved measurements support the identification of the new process as due to free excitons localized by alloy fluctuations. The decay in PL intensity was measured under conditions of different excitation density, as shown in Figure 4.11. These curves represent the total LE PL intensity, with no attempt as yet to study the lifetime behaviour at different spectral positions on the peak. The LE PL was found to decay on an extremely long time scale, with an initial 1/e decay of about 3 ms, stretching to tens of ms at later times. This compares well with the estimated radiative lifetime of 1 ms for unlocalized FE [80H], and not with the fast decays (~ 1 μs) typically associated with the Auger transitions of impurity related centers. This long lifetime together with a relative scarcity of localization centers would account for the very low excitation density at which saturation sets in. In agreement with studies in GaAs$_{1-x}$P$_x$ and Ga$_{1-x}$Al$_x$As, the LE are not only long lived, but the decay curves are nonexponential [85O, 84L, 84S, 83S] and power dependent [85O, 84L, 83S]. This nonexponential behaviour is thought to arise from a distribution of the probability of scattering by the random potential, which is needed for an allowed no-phonon transition [85O, 84L, 83S]. The power dependence also follows from an increase in the fast component of the decay curves at higher
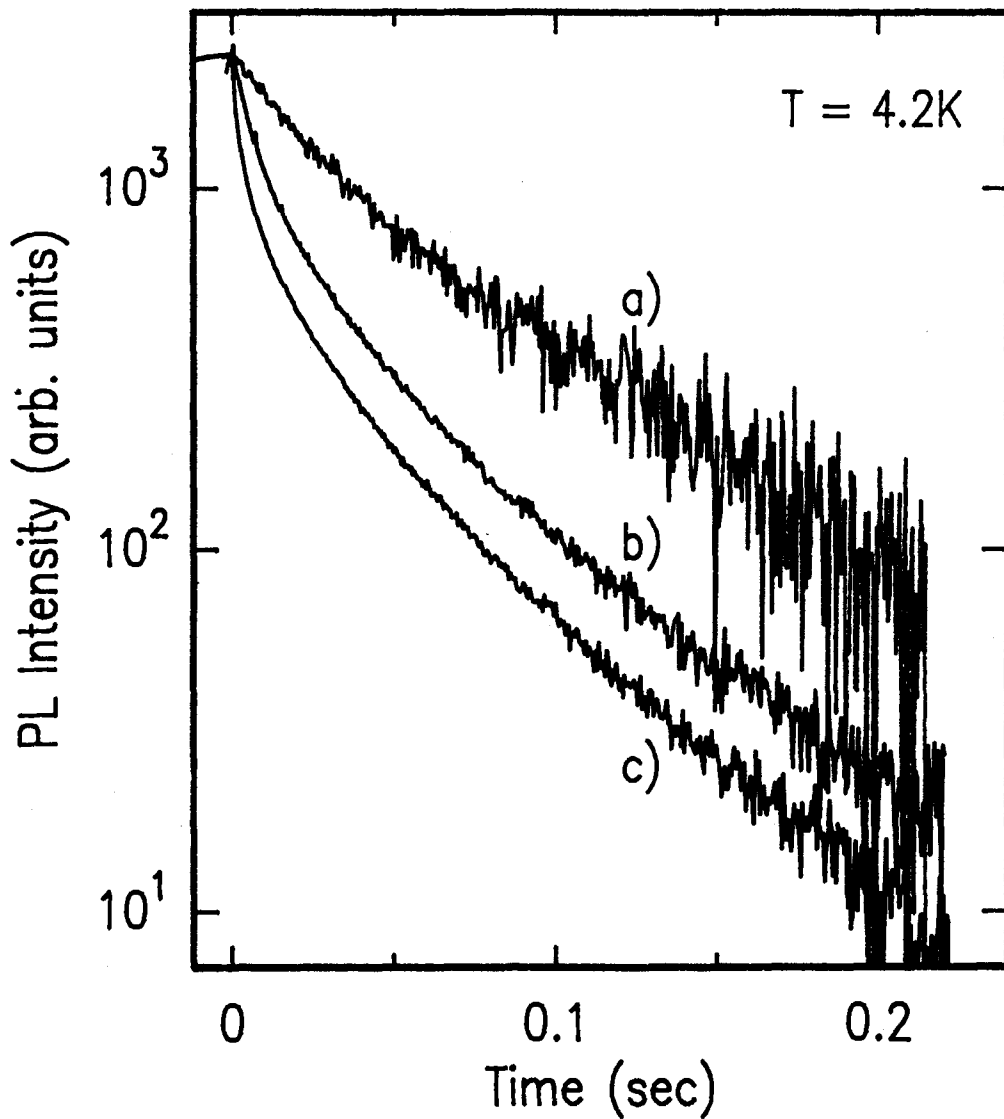
Figure 4.11 Intensity of the LE PL as a function of time for excitation densities of a) 1 , b) 3.5 and c) 35 μW cm^{-2}. The decay curves are nonexponential, with a faster decay occuring at high excitation density. The curves have been shifted to give equal intensity at t=0.

excitation density given the increase in Auger transitions.

The assignment of the LE PL features to an intrinsic process, such as localization by alloy fluctuations, is further supported by persistence of the LE PL band despite annealing at temperatures up to $958^{\circ}C$ (i.e. $333^{\circ}C$ higher than the growth temperature). The RTCVD epitaxial layers are initially metastable since the rapid thermal processing effectively freezes the atoms into place as the temperature is quickly ramped down. Any non-random clustering of the Ge atoms, vacancies, etc. might then be expected to be eliminated by annealing. Figure 4.12 compares PL spectra of a) and d) an as-grown 83 Å $Si_{0.8}Ge_{0.2}$ single quantum well sample, with those after a 20 min anneal at b), e) $907^{\circ}C$ and c), f) $958^{\circ}C$. Note that the initial SiGe thickness is below the equilibrium critical value (~100Å, People and Bean [85Pa]), so that the layers should remain fully strained even after annealing. The upper three curves (d, e, f) were taken with a high excitation density (6.5 W cm^{-2}) and thus show the SiGe BE features, while the lower three spectra (a, b, c) correspond to low excitation density (25 mW cm^{-2}) at which the LE PL dominates. The SiGe spectral features for the annealed samples actually lie to higher energy than shown on the energy scale in Figure 4.12, since they were shifted to align the SiGe BE_{NP} peaks. The length of the arrows under curves b), c), e),and f) indicate the shift for each curve needed to put it at the correct energy. The observed shift in the SiGe BE PL with annealing is consistent with a lowering of the Ge fraction as the Ge atoms diffuse into the Si substrate and cap. Despite the migration of the Si and Ge atoms during annealing, the LE peaks do not disappear and shift roughly as expected with the BE luminescence (i.e. with the effective band gap). This confirms that the LE PL features in the as-grown spectrum are due to fluctuations in Ge concentration which are entirely random in nature and therefore are maintained even after sample annealing. The LE PL is somewhat closer to the BE in the annealed samples, perhaps indicating that with the lower Ge fraction the deep localization centers are scarcer and therefore the density of states tail fills up to a higher energy level. However, it is difficult to draw any quantitative
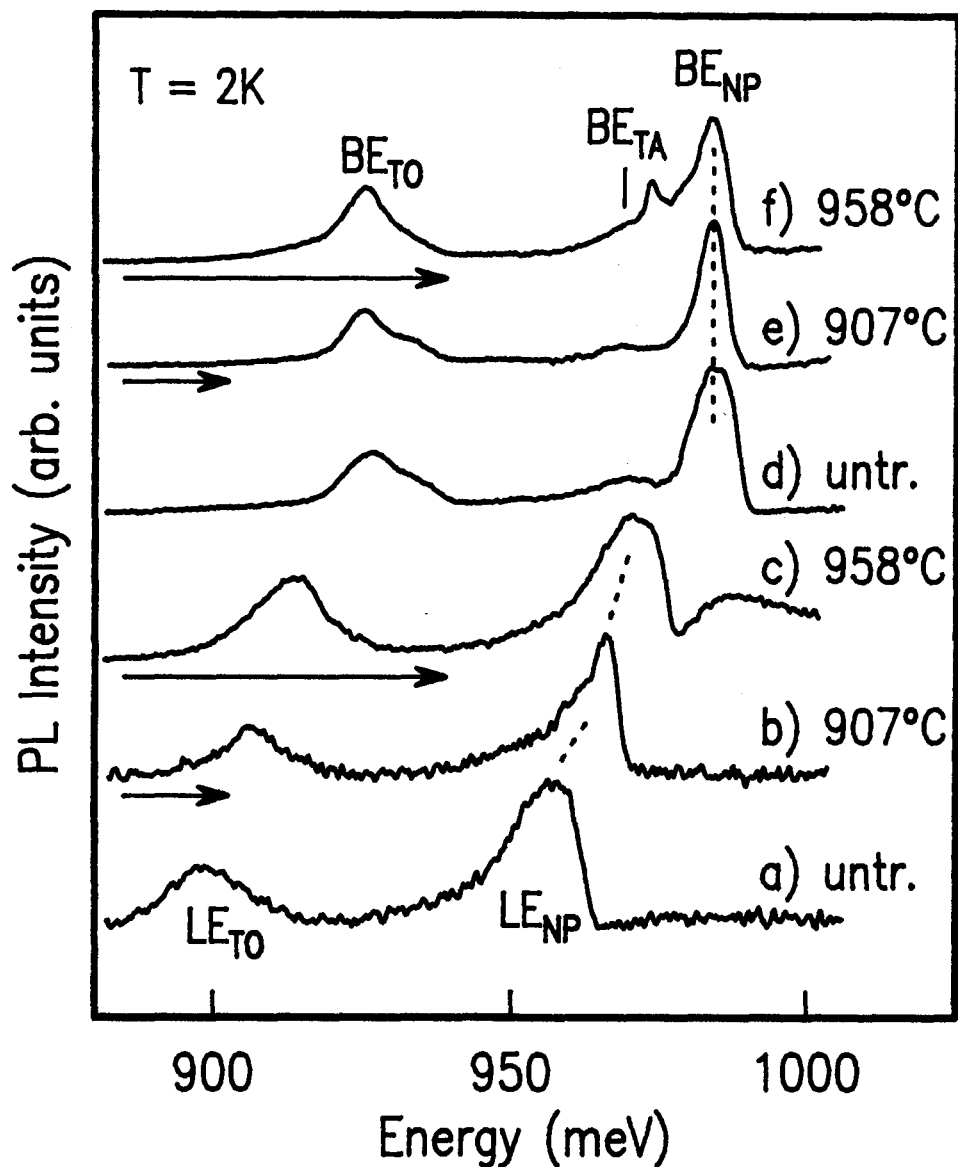
Figure 4.12 PL spectra of 83 Å $Si_{0.8}Ge_{0.2}$ quantum well samples with anneal treatments of a),d) untreated, b),e) 20 min at 907°C and c),f) 20 min at 958°C. The top three curves, taken with high excitation density (6.5 W cm^{-2}), show the usual SiGe BE PL features. The bottom three curves were at low excitation density (25 mW cm^{-2}), at which the LE PL clearly dominates. Spectra b), e) and c), f) were shifted to lower energy by 17.5 meV and 54 meV respectively to line up the SiGe BE peaks. The sharp feature above the BE_{TA} in f) and broad band above the LE in c) originate from the Si substrate.

70

conclusions about the LE-BE separation based on this particular set of samples, since the initial SiGe thickness of only 83 Å suggests that situation may be complicated by quantum confinement effects.

The LE PL features were observed in many RTCVD samples, including several thicknesses and Ge concentrations in single SiGe layers, as well as multiple quantum well and superlattice structures. In all cases the epitaxial layers were below the critical thickness for strain relaxation, so misfit dislocations are not thought to play any role. In MBE SiGe, Denzel *et al.* [92D] also very recently observed a broad no-phonon line and its TO replica (which they labelled A1 and A2) at low excitation power density. Although these transitions have not been studied in any great detail as yet, their appearance only at low power densities and their energy relative to the the band-edge PL suggests that these peaks are also due to LE recombination. This supports the identification of the PL process as intrinsic to the SiGe alloy rather than resulting from some growth specific defect. The broad band often observed 100 meV below the band gap in MBE material (see next section) may in fact originate from a related process. There also may be some connection between the LE PL and the L-band identified in the bulk relaxed SiGe alloys [82M, 89Wb].

4.4. The Deep Band in Molecular Beam Epitaxy $Si_{1-x}Ge_x$

SiGe grown by conventional MBE has been plagued with a strong broad PL feature, centered roughly 120 meV below the expected SiGe band-edge, which occurs more strongly in layers with weak or no observable band-edge luminescence [92D, 92Na, 92Sa, 92Sb, 92T, 90T]. This especially seems to pose a problem in SiGe layers thicker than 40 to 100 Å (depending on x) [92Na], although so far the PL process which gives

rise to this band is not clear. Recombination of excitons bound to a strain field created by Ge platelets have been suggested by Noël *et al.* [92Na], while Glaser *et al.* [93G] maintain that a donor-acceptor pair process is responsible, and Terashima *et al.* [92T] consider it due to defects in the SiGe layer or at the interface. On the other hand, one research group has in fact been successful in growing thick SiGe layers by conventional MBE which show near band gap PL features identified as BE or FE. However, the differences in growth conditions which select between the near band gap or deeper PL for the thick MBE layers are not yet understood [92W].

The PL spectrum of a relatively thick (1300 Å) layer of MBE $Si_{0.82} Ge_{0.12}$ which has only the broad deep PL band is shown together with its PLE spectrum in Figure 4.13. The PL spectrum is dominated by a feature with a ~ 83 meV FWHM linewidth that peaks 108 meV below the expected SiGe band gap. Both the broad linewidth and the peak position of this sample are typical for this PL band. In the PLE spectrum the PL intensity was monitored at the low energy tail of the PL band (855 meV, see the arrow labelled 'PLE'), with similar results obtained at other wavelengths along the band. As discussed earlier, in an indirect gap material such as SiGe the PLE spectrum does not show peaks, but rather a gradual increase in intensity above some absorption edge. The onset of the PLE here coincides within experimental error (about ± 15 meV) with the high energy edge of the PL band. This indicates that the PL process responsible for the broad band is no-phonon in nature. The strong no-phonon character of this band contrasts observations of comparable no-phonon and phonon replica intensities for the shallow BE PL and for the localized exciton PL.

Time decay curves of the PL intensity are shown in Figure 4.14 for a) the deep broad band PL and b), c) shallow SiGe BE PL in the MBE SiGe, with the upper time scale as indicated for a) and the lower scale for b), c). Curve a) was taken from the same sample as in the PL and PLE spectra of Figure 4.13, with the PL intensity monitored as a function of time at the high energy side of the peak in the PL band (988 meV, see the
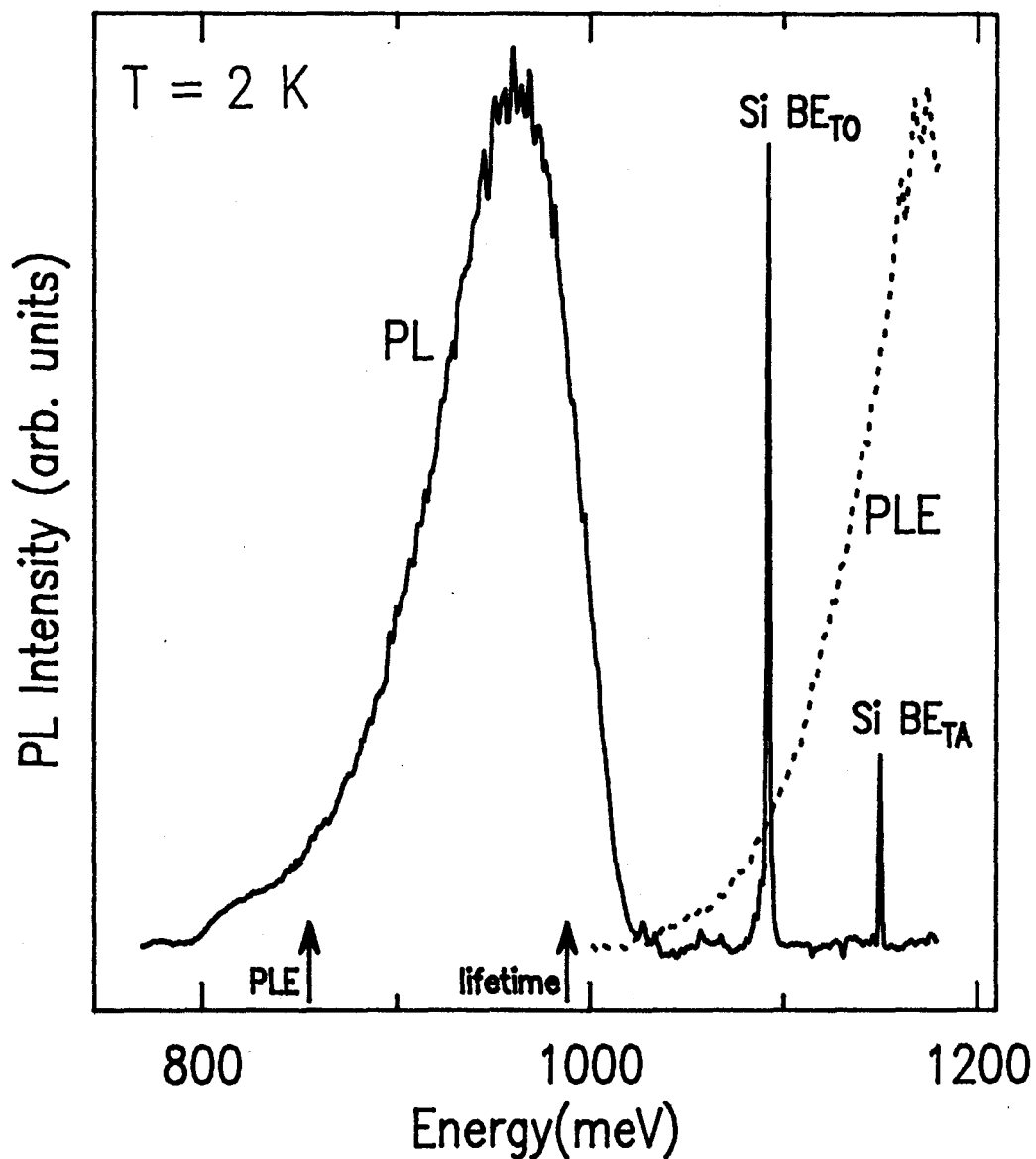
Figure 4.13 PLE spectrum (dashed line) for a 1300 Å $Si_{0.88}Ge_{0.12}$ MBE sample which had only the deep broad band PL feature as shown (solid line). For the PLE, the PL intensity was monitored at the low energy tail (855 meV), with similar results obtained at other wavelengths along the band. The onset of the PLE spectrum corresponds approximately with the high energy edge of the PL, indicating that the PL process does not involve the participation of phonons.
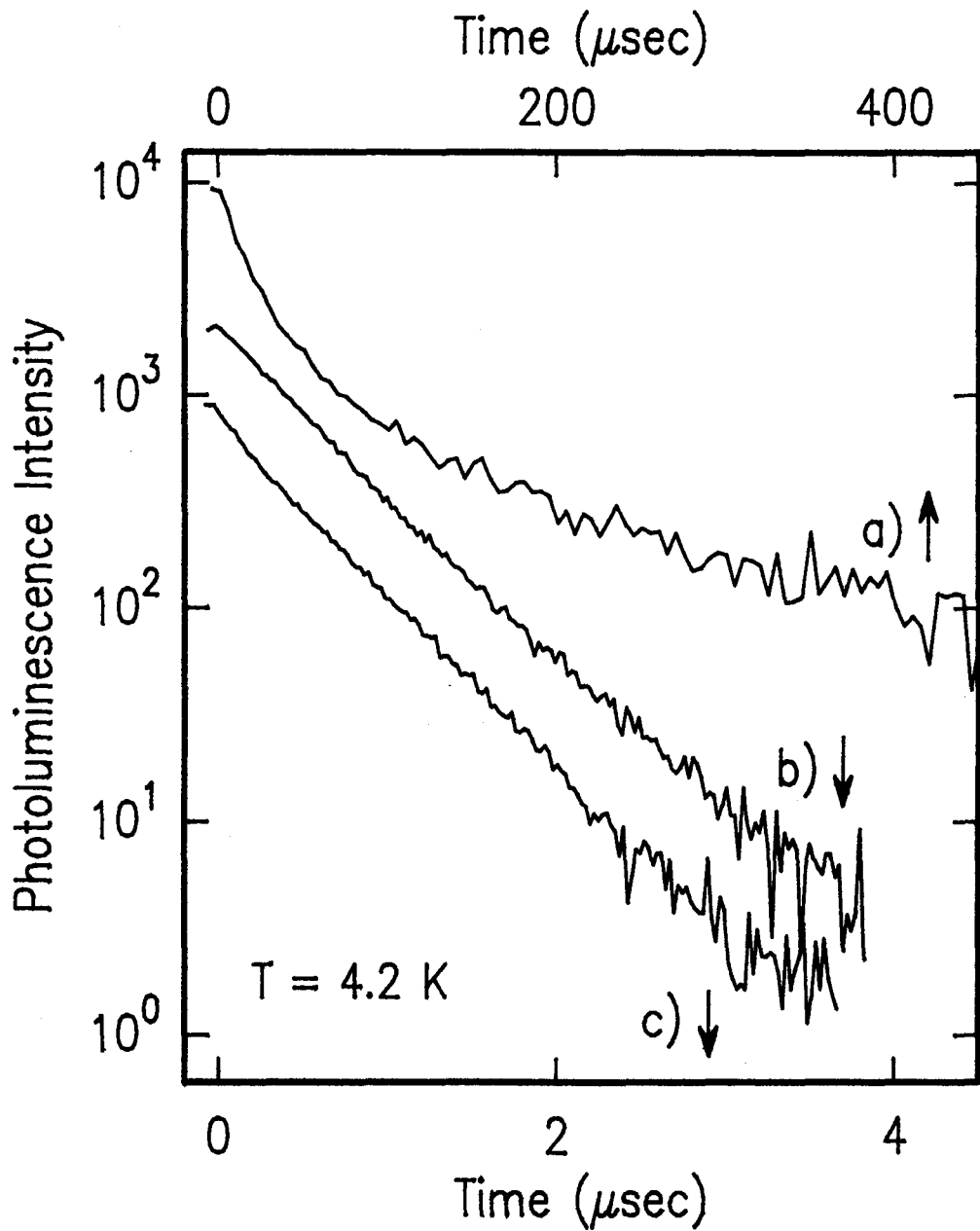
Figure 4.14 In a) the PL decay curve of the deep broad band of the sample in Figure 4.13 was measured on the high energy side of the PL band (988 meV). The decay curves of two shallow SiGe no-phonon BE lines of a MQW MBE sample are shown in b) and c). Note that the time scale for a) is 100 times slower than for b) and c).The curves have been shifted vertically for clarity.

arrow labelled 'lifetime' in Figure 4.13). The decay is nonexponential with a fast component of roughly 25 μs extending to a long lived component of 145 μs. Similar results were obtained for the broad PL band in other MBE samples, one consisting of a 15 period MQW of 68 Å $Si_{0.83} Ge_{0.17}$/ 200 Å Si and the other a 20 period MQW of 50 Å $Si_{0.85} Ge_{0.15}$/ 200 Å Si. Note that this is several orders of magnitude faster than the millisecond lifetimes found for the localized exciton luminescence in the RTCVD SiGe, supporting the observation that a somewhat different sort of process is at work in the deep band PL.

However, there may actually be a connection between this broad deep band PL and the LE PL observed in the RTCVD material. We have directly measured a PL quantum efficiency of 1.9 ± 0.35 % for the broad MBE band, which however represents a lower bound since the sample appeared to have degraded somewhat over time. Despite the lower quantum efficiency, the MBE sample can emit much more PL than the RTCVD material since it does not saturate at low power density. The MBE band is associated with a much deeper potential that also appears to have a shorter range than that of the RTCVD LE PL. This leads to the predominantly no-phonon PL spectrum and shorter PL lifetime. These characteristics are consistent with an LE model in which the Ge concentration fluctuations are much larger than those produced by random statistics. There is already evidence that the emission process involved in the MBE band can be correlated with the appearance of platelets, which might in fact be regions rich in Ge, in transmission electron micrographs [92Na]. There is also a large body of literature describing Ge islanding phenomena in MBE growth in the Si-Ge system [91L, 90E, 91J, 91Sc].

Shallow BE PL was also observed in the MBE material but only in relatively thin (< 100 Å) layers, as described by Noël et al. [92Na]. The decay curves for the shallow SiGe BE PL in the MBE material are found to be about 100 times faster than the deep broad band PL, as indicated by the different time scales in Figure 4.14. Again, this supports the observation that the deep PL band is distinct from the shallow transitions. Curves b) and

c) were measured at the BE_{NP} peaks of two quantum wells of a MQW sample (at 1102 meV and 1108 meV). (The top 18 wells of this 20 period 27 Å $Si_{0.85}Ge_{0.15}$/ 200 Å Si MQW sample were removed by etching at NRC.) The lifetimes of 561 ns and 536 ns are in good agreement with those reported for shallow BE in Si, and for the shallow BE in the RTCVD SiGe. However, under different excitation densities the time decays of the PL signals became nonexponential with long-lived ($\sim 1\mu s$) PL becoming more dominant with decreasing excitation. Similar effects were noted in several other MQW samples. The origin of this long lived component is not clear, however it may result from the release of localized excitons from alloy fluctuations and subsequent recombination as BE, which is expected to become increasingly important at low excitation.

4.5. Summary and Discussion

Well resolved band edge photoluminescence has been observed in strained SiGe grown by RTCVD and MBE. This PL was shown to evolve from BE emission at low temperatures to FE peaks above about 12 K. The energy of the BE no-phonon peak provides a convenient measure of the SiGe band gap as a function of Ge composition. Good agreement was found between these band gap measurements and the simple deformation potential theory prediction of Lang *et al.* [85L].

We have also demonstrated that high quantum efficiency (> 10 %) can be achieved in SiGe through the elimination of nonradiative channels, rather than by increasing the radiative rate. This contrasts the usual approach to improving quantum efficiency which is to increase the radiative transition rate, for example by creating a direct gap, so that the excitons simply recombine before having a chance to be lost to the nonradiative processes.

This highly efficient PL process is identified with excitons localized by random fluctuations in Ge concentration. This conclusion is based on the observation of:

- an exponential low energy tail and sharp high energy cut-off,
- shift in the high energy edge with increasing excitation power density,
- a long lifetime, with power dependent, nonexponential decay curves,
- saturation at low excitation power levels,
- presence in many different sample structures, including annealed, and
- high quantum efficiency.

Although the 11.5 % quantum efficiency of the LE band is impressive, to be of practical use several problems must be addressed. Firstly, the saturation power must be increased, by increasing both the number of localization centers and the radiative rate. Also, the LE binding energy due to statistical fluctuations alone is too small, so that thermal quenching occurs at only a few tens of K. Conditions for Anderson localization in indirect gap AlGaAs have been artificially created using a disordered superlattice structure. For SiGe this might instead be accomplished by development of a growth process in which the compositional fluctuations are no longer statistical but rather driven by some other means, producing in the limit a 'suspension' of pure Ge particles a few tens of Ångstroms in radius and separated by an average > 100 Å. As well as increasing the number of binding centers, this might also increase the radiative rate by confining the holes in much deeper and more abrupt potential wells, thus increasing the likelihood of no-phonon processes. The greater well depth would also stabilize the LE emission up to much higher temperatures.

The deep, broad, relatively efficient PL band observed in the MBE material may be due to a related process and therefore might give some clues for an MBE growth process from which practical applications might evolve. While the MBE growth may inherently favour Ge clustering, similar effects might be developed in CVD material with careful consideration of growth parameters.

Chapter 5.

Results for $Si_{1-x}Ge_x$/Si Quantum Well Structures

5.1. Introduction

In the previous chapter, the PL from strained SiGe layers was shown to be due to recombination of free excitons, excitons bound to shallow impurities, and/or excitons bound to fluctuations in Ge content. In this chapter, PL spectroscopy is used to determine the effect on the excitons of decreasing the SiGe layer thickness to less than 100 Å. Because the SiGe layers are thin, the band offsets at the interface with the Si play an important role. The excitons migrate from the Si to the smaller band gap region of the epitaxial SiGe layers where they become trapped and eventually recombine. The effect of confinement of the exciton on the band edge PL energies is described in section 5.2. In section 5.3, the origin of the PL features in thin quantum wells is studied in more detail. Although the PL at low power density differs in some ways with the LE PL of the thicker layers of Chapter 4, close examination of the excitation power dependence and the PL decay times shows that the underlying PL mechanism is in fact similar in nature. The chapter is completed with a look at some more complicated quantum well structures consisting of stepped quantum wells (section 5.4) and tunneling structures (section 5.5).

5.2. Quantum Confinement Shifts

When a thin SiGe layer is sandwiched between two larger band gap regions of Si, then we have the quantum well potential described in section 1.4. The PL emitted from such a structure at low temperatures will consist of recombination of an electron and hole bound together by their Coulomb attraction i.e. an exciton, but where the exciton wavefunction is modified due to the quantum confinement. To determine the effects of quantum confinement, we look here at a series of PL spectra for SQW samples with nominally identical Ge fractions of x=0.2 and decreasing SiGe well thicknesses of $L_z = 83$, 67, 58, 50, 46, 42 and 33 Å. Figure 5.1 shows the PL spectra for three of these samples with the SiGe well thicknesses of $L_z = 83$ to 50 Å, and 33 Å. The SiGe thicknesses were confirmed by transmission electron microscopy to be within ±5 Å for several samples of this series. The Ge fraction was measured on a thick sample using X-ray diffraction and found to be 0.2 ± 0.02. In addition, we included in the sample set four multiple quantum well samples from an earlier study [91Sa]. The Si barriers in these MQW's were thick enough that no coupling between the quantum wells is expected. These samples were also grown with nominal Ge fraction 0.2, which was determined by X-ray diffraction analysis on each sample to actually be 0.18 ± 0.02. The SiGe well thicknesses for the four MQW samples were nominally identical, although transmission electron microscopy indicated sample thicknesses of 23, 25, 29, and 34 Å (± 3 Å) due to the wafer non-uniformity. The transmission electron microscopy values are therefore used below for the four MQW samples, while the nominal well thicknesses are used for the seven SQW's.

For each sample we observe the NP and phonon replica features found, in the previous chapter, to be characteristic of BE recombination. The LE PL feature is also observed, however the focus of this section is the shift in the BE PL spectra to higher energy with decreasing well thickness. The positions of the BE_{NP} peaks are plotted versus the SiGe quantum well thickness in Figure 5.2, and are compared with the
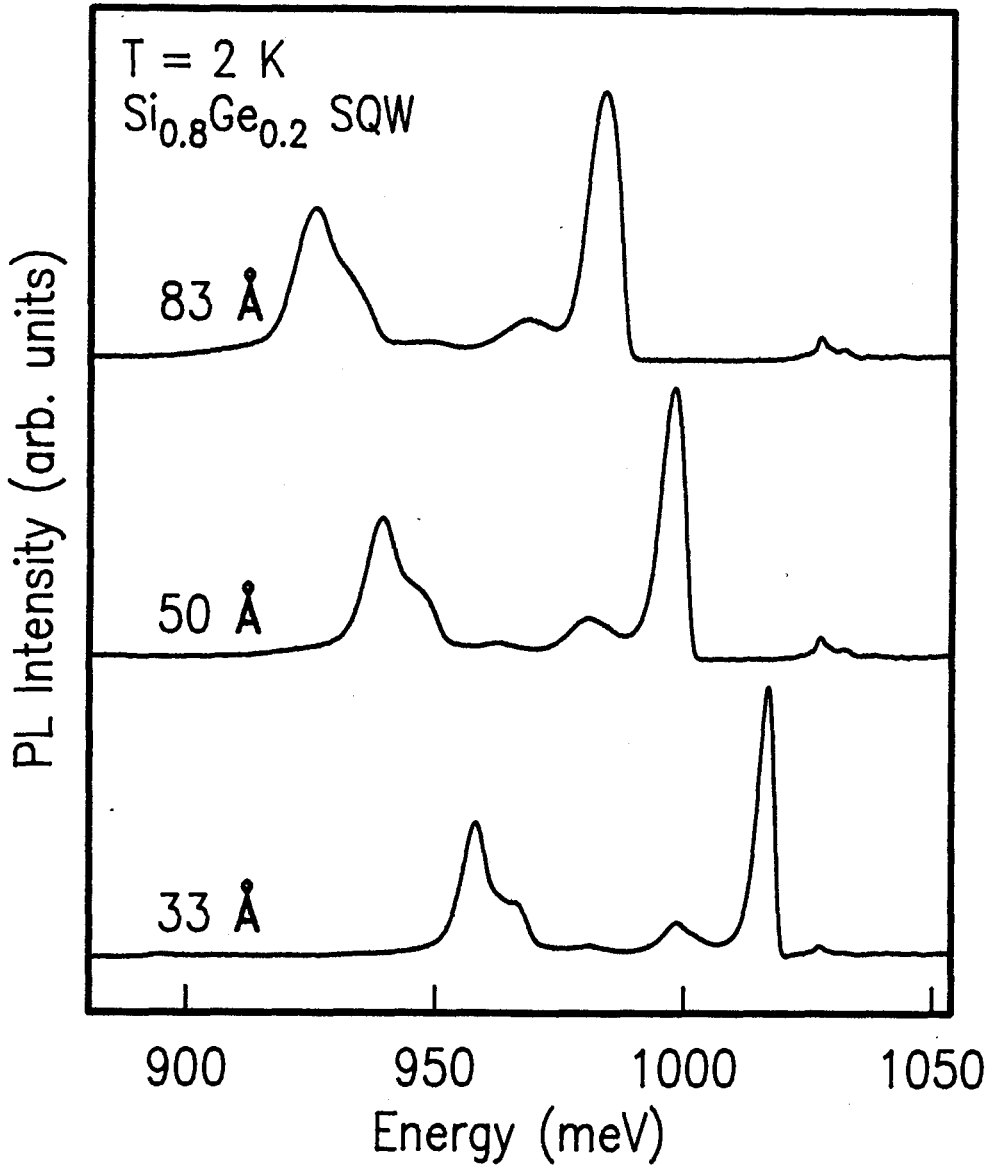
Figure 5.1 BE PL spectra for $Si_{0.8}Ge_{0.2}$ quantum wells with nominal thicknesses of 83, 50, and 33 Å, as indicated. The PL features shift to higher energy with decreasing well width due to quantum confinement. The PL intensities have been scaled to give equal BE_{NP} peak heights.

the predictions of the envelope function scheme, as described below. The uncertainty in the data points is ± 5 Å for the well thicknesses and ± 1 meV for the measured PL energies. As well there is some uncertainty introduced because the actual sample compositions may differ from the nominal x=0.2 value. The uncertainty in the X-ray diffraction analysis of the Ge content corresponds to roughly ± 13 meV (i.e. $\Delta x = \pm 0.02$). However, clearly from the scatter in the data the control over x during the growth must be considerably better than ± 0.02.

When both the electron and hole are confined together in the quantum well, then as the well thickness is decreased to less than the exciton Bohr radius, the character of the quantum confined exciton becomes more 2-dimensional. Quantum confined exciton binding energies have been shown to increase by up to a factor of four compared to 3D values (see for example the review by Singh [93Sb]). Similarily, impurity ionization energies (and BE binding energies) are also affected because the carrier is held closer to the impurity by the quantum well potential. In very thin quantum wells this 2D character is eventually lost as the confinement energy of either the electron or hole approaches the height of the barrier and the exciton wave function leaks out of the well region. For $Si_{0.8}Ge_{0.2}$ on Si most of the band discontinuity occurs in the valence band (see discussion in section 1.3). According to the calculations of Van de Walle and Martin [86V], the band alignment is type I with $|\Delta E_v| \sim 170$ meV and $|\Delta E_c| < 30$ meV. The quantum confinement of the electrons can therefore be neglected for all well thicknesses. Because the electron is not confined (or only weakly confined), the exciton in this case is not expected to become strictly 2D. For the purposes of this study, we therefore neglect the variations in the binding energies due to the confinement and simply consider the observed shift in the BE PL energies to be a consequence of quantum confinement of only the hole part of the exciton.

Since the PL measurements are conducted at low temperature, the photogenerated carriers quickly lose energy and the holes populate only the deepest of the quantum well
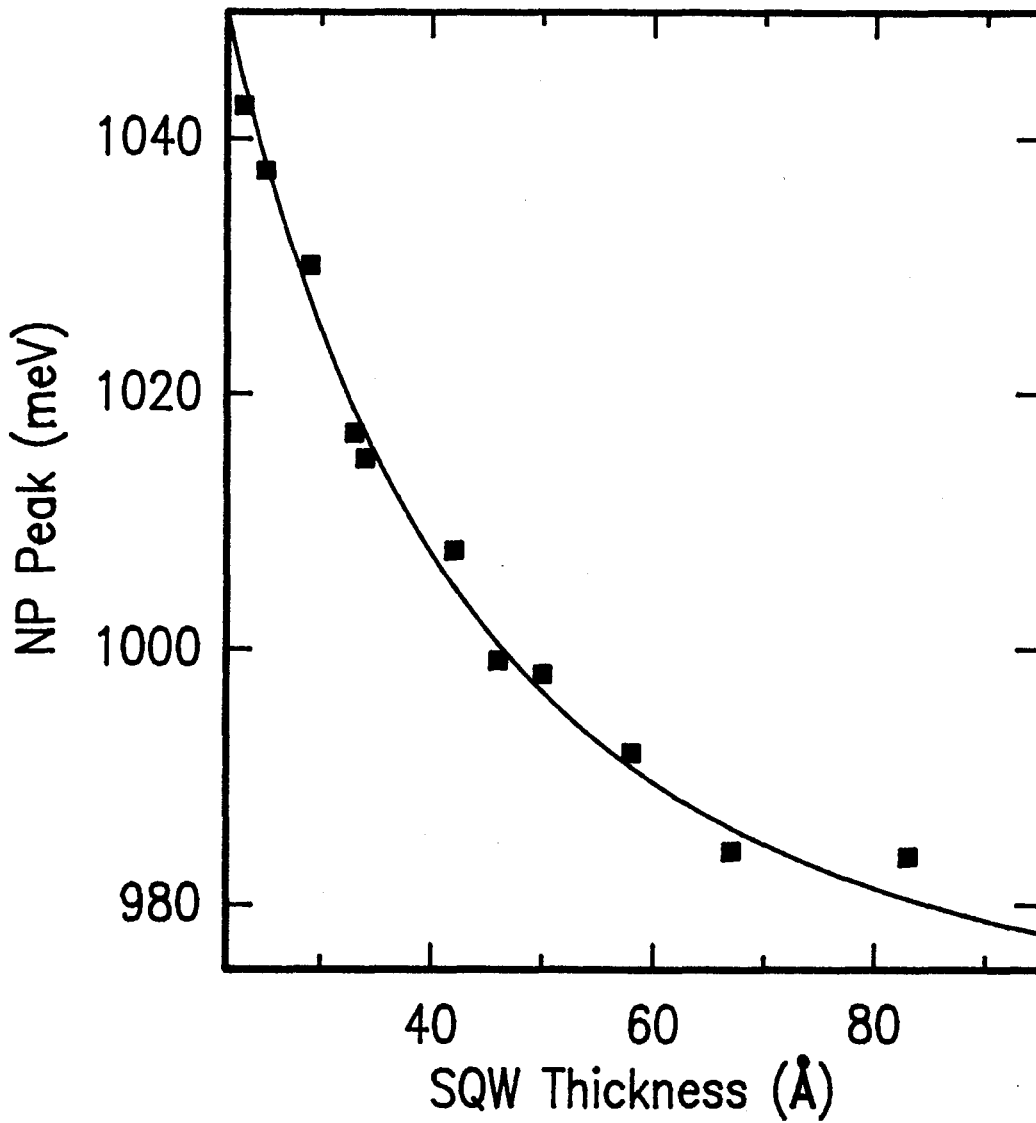
Figure 5.2 Position of the BE_{NP} line as a function of $Si_{0.8}Ge_{0.2}$ well width. The solid line shows the result of the single band envelope function calculation described in the text.

states under typical excitation conditions. Because of the large splitting of the heavy and light hole valence bands by the strain (section 1.2) the light hole levels lie to higher hole energy and hence are unoccupied. We are therefore interested in the increase in the zero point energy, which separates the ground state of the heavy holes and the bottom of the potential well (i.e. the heavy hole valence band edge), with decreasing well thickness. The PL associated with these quantum confined holes is then expected to be shifted to higher energy by this same amount relative to that from the thick strained SiGe layers (see Figure 5.3).

The quantum confinement shift can be determined using the envelope function scheme reviewed in section 1.4. We treat the case of zero in-plane wave vector ($k_\perp$) only, for which the heavy hole band decouples from the light hole and split-off bands, as described in the Appendix. The in-plane wave vector is associated with motion of the excitons in the plane of the quantum well. Since we are dealing here with BE recombination, it is reasonable to assume $k_\perp = 0$. Note that non-zero k_z does not imply kinetic energy in the z-direction since k_z in the description of eigenstates for the quantum
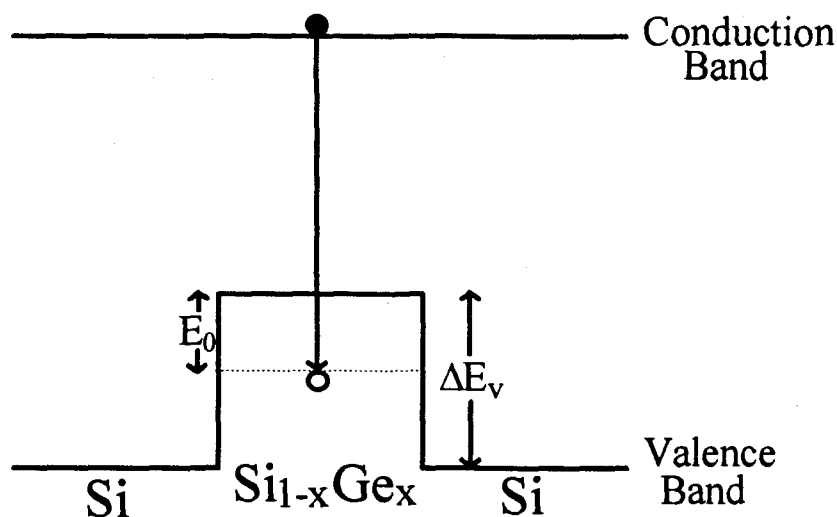

Figure 5.3 Schematic of a single SiGe quantum well with Si barriers. As the well thickness is decreased the magnitude of the zero point energy (E_0) increases. This causes a corresponding shift to higher energy in the emitted PL energy.

well is not associated in the usual way with Bloch functions, but rather describes only the envelope function, $\phi(z)$. Because the heavy hole band is not coupled to the other bands for $k_\perp = 0$, the heavy hole energy eigenvalues relative to the band edge are given by the solutions to the transcendental equations of the square well potential (see equations 1.4 and 1.5). For the barrier and well effective masses we use the heavy hole values in the z-direction, as given by the Luttinger parameters:

$$\frac{m_0}{m_{hh}} = \gamma_1 - 2\gamma_2 \qquad (5.1)$$

with the values of γ_1 and γ_2 for Si and Ge listed in the Appendix. For SiGe a linear interpolation between pure Si and pure Ge is used. This gives effective masses of 0.291 m_0 for Si and 0.268 m_0 for $Si_{0.8}Ge_{0.2}$. The valence band offset is treated as a fitting parameter. A value of $\Delta E_v = 188.2$ meV gives the best least squares fit between the experimentally observed (squares in Figure 5.2) and calculated PL energies (solid curve in Figure 5.2). The predicted confinement energy increases from 13.6 meV for a well of width 83 Å to 77.8 meV for a width of 23 Å, which corresponds to predicted PL energies of $E_{PL} = E_g(Si) - \Delta E_v + E_{conf} = 980.4$ meV and 1044.6 meV, respectively. The valence band offset obtained from the fit to the PL energies (188.2 meV) is roughly in agreement with the difference between the Si and $Si_{0.8}Ge_{0.2}$ band gaps, $\Delta E_g = 159$ meV, calculated from the equation for the SiGe band gap as a function of x (equation 4.2).

Confinement shifts in PL energies for SiGe quantum wells have been observed by several other research groups [92Fa, 92R, 92V, 92W, 92Z]. In particular, series of quantum wells of different thicknesses were studied for nominal Ge fractions of x=0.16 by Fukatsu et al. [92Fa], x=0.24 by Wachter et al. [92W], and x=0.08 by Zollner et al. [92Z]. They also found good agreement between their observed confinement energies and values predicted by analyses similar to that described above. Notice that the strain couples the light hole band and split-off bands, even for $k_\perp = 0$, so that one needs to use the full Luttinger-Kohn Hamiltonian (see Appendix) to describe any light hole level in the SiGe.

The most obvious difference in the PL spectra with decreasing well thickness is the shift in the PL energies, however as the zero point energy increases there is also more leakage of the exciton wave function into the Si barriers. The effect of this can be seen experimentally in the relative intensities of the Si-Si, Si-Ge, and Ge-Ge phonon replicas. In Chapter 4, the ratio of the Si-Si PL peak height to the Si-Ge peak height was shown to agree with the ratio of probabilities of Si-Si to Si-Ge nearest neighbours in a random lattice (equation 2.2). As the SiGe well width is decreased to much less than the spatial extent of the exciton, the probability of generating a Ge-related phonon also decreases. The increase in the Si-Si relative to the Si-Ge phonon intensity with decreasing well width is obvious in Figure 5.4 for a 15 Å $Si_{0.65}Ge_{0.35}$ quantum well in comparison to a 200 Å layer of the same nominal Ge content. The same effect was also noted by Robbins et $al.$ [92R] in comparing two samples of $x=0.17$ with SiGe thicknesses of 570 Å versus 63 Å. Table 5.1 lists the observed ratio of the Si-Si to Si-Ge phonon intensities for two pairs of samples consisting of either a thin SiGe layer or a thick SiGe layer with nominal Ge fractions of $x_{nom} = 0.2$ or $x_{nom} = 0.35$. An "observed" x value (labeled x_{ph}) corresponding to the phonon peak heights can be obtained using equation 2.2. As expected, for the thick layers $x_{ph} \sim x_{nom}$, while for the thin SiGe quantum wells $x_{ph} < x_{nom}$.

Table 5.1 Effective Ge Fraction in SiGe Quantum Wells

x_{nom}	Thickness (Å)	I_{Si-Si}/I_{Si-Ge}	x_{ph}	x_{eff}
0.18 ± 0.03	23 ± 3	3.3	0.13	0.14
0.20 ± 0.02	200 ± 10	1.8	0.22	0.20
0.35 ± 0.04	15 ± 10	1.6	0.24	0.23
0.35 ± 0.04	100 ± 10	0.95	0.34	0.35
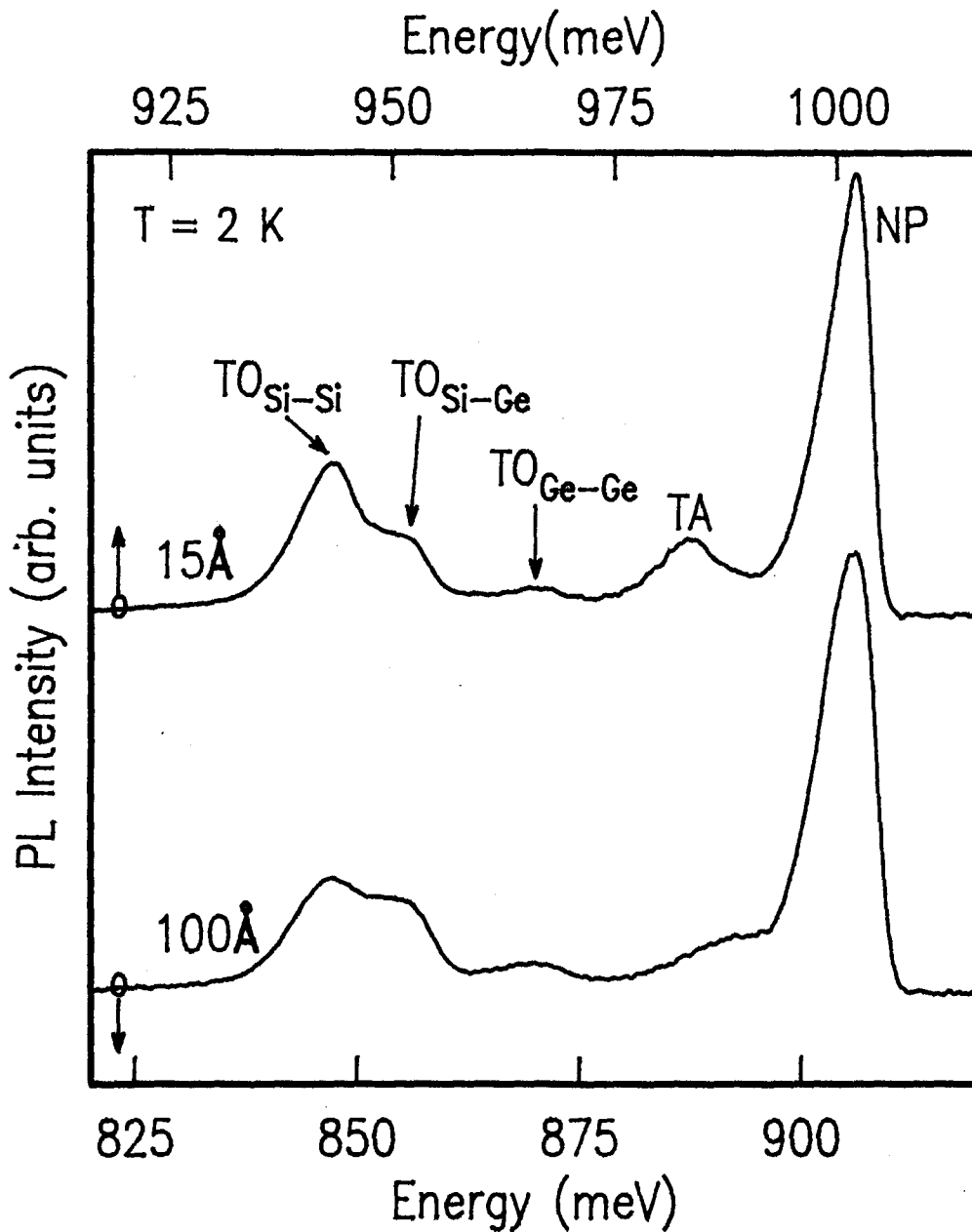
Figure 5.4 Comparison of PL spectra for $Si_{0.65}Ge_{0.35}$ quantum wells with nominal thicknesses of 15 Å (top) and 100 Å (bottom). The bottom energy scale corresponds to the 100 Å sample and the top energy scale to the 15 Å sample, as indicated by the arrows at the left. The PL in the narrow quantum well is shifted to higher energy due to quantum confinement. As well, the relative intensity of the Si-Si TO replica to the Si-Ge and Ge-Ge TO replicas is observed to increase. The spectra have been normalized to give equal BE_{NP} peak heights.

A theoretical prediction of x_{ph} as a function of well width can be determined by calculating the effective x seen by the exciton. The effective Ge fraction, x_{eff}, is approximated in Table 5.1 by taking the values of x in the well and barrier and weighting them by the probability, as given by the envelope function, of finding the hole in the corresponding region:

$$x_{eff} = x_{well} \int_{z \in well} \phi^*(z) \, \phi(z) dz + x_{barrier} \int_{z \in barrier} \phi^*(z) \, \phi(z) dz \qquad (5.2)$$

This is based on the assumption that the electron-hole overlap of the exciton within the quantum well versus that in the barriers is determined only by the hole wave function. The valence band offset of 188.2 meV, obtained above, can be used in calculating the extent of the hole wave function for the two x=0.2 samples. For the x=0.35 samples the band offset ($\Delta E_v \sim 235$ meV) is estimated using the predicted difference in E_g (equation 4.2) and assuming zero conduction band offset. As shown in Table 5.1, equation 5.2 gives good agreement with the observed x_{ph} values for all four SiGe samples. For the thick SiGe layers (i.e. 200 Å $Si_{0.8}Ge_{0.2}$, 100 Å $Si_{0.65}Ge_{0.35}$) the nominal and effective x values are the same since the leakage of the hole wave function outside of the well is negligible.

5.3. Quantum Confined Excitons Localized by Alloy Fluctuations

In this section, the mechanisms behind the quantum well band edge PL features are studied in more detail by looking at the excitation power dependence and the PL lifetimes. In addition to the series of x=0.2 RTCVD samples used in the previous section, we also study several very thin (≤ 15 Å) quantum wells. The first is the single quantum well sample of Figure 5.4 with Ge fraction of x=0.35 and nominal thicknesses of 15 Å. In

addition, several very thin MBE samples were found to give similar results to the 15 Å RTCVD sample, as discussed below. The data presented here concentrates on a 10 period nominal 10 Å $Si_{0.6}Ge_{0.4}$/ 200 Å Si MBE multiple quantum well. X-ray diffraction and transmission electron microscopy measurements indicated that the quantum wells were actually 12 Å thick and had x=0.38.

Figure 5.5 compares sets of PL spectra taken with high (I_0) and low excitation power density ($10^{-3} I_0$) for each of the CVD and MBE samples. The top three pairs of spectra are from the $Si_{0.8}Ge_{0.2}$ CVD single well samples of intermediate well thicknesses a) 83, b) 58, and c) 33 Å, while the PL of the very thin quantum wells are shown in d) 15 Å $Si_{0.65}Ge_{0.35}$ CVD sample and e) 12 Å $Si_{0.65}Ge_{0.38}$ MBE sample. In each sample at high power (dashed curves) we observe the NP peak and phonon replicas (TO and TA) which are normally attributed to the SiGe BE recombination. The band-edge PL has shifted as expected to higher energy with decreasing well thickness from a) through c) due to quantum confinement effects. The value for I_0 was chosen to minimize the broadening of the features which occurs at very high excitation, and was of the order of a few W cm^{-2} in each case. At $10^{-3} I_0$ the BE PL in the intermediate thickness CVD samples (a-c) drops in intensity to reveal the broad NP and phonon replica features of the localized exciton process discussed in section 4.3. The LE and BE_{NP} transitions were simultaneously present in the spectra of the 83 Å and 58 Å wells at intermediate powers (not shown). The low power spectra in curves (a-c) show the broad asymmetric lineshape, with a long exponential tail to low energy, which is characteristic of the LE transitions. Although the spectra of the thin quantum well samples (curves d,e) do not show a change in lineshape at low power, other evidence as outlined below suggests that the features are also due to LE.

The energy separation between the LE and BE peaks in Figure 5.5 (a-c) is observed to decrease with decreasing well thickness from about 20 meV for L_z = 83 Å to 12 meV for L_z = 33 Å. The LE-BE separation is reduced in the thin (15 Å) CVD sample to only 7 meV. Further, in the 12 Å sample (Fig. 5.5e) there was, to within 0.5 meV, no
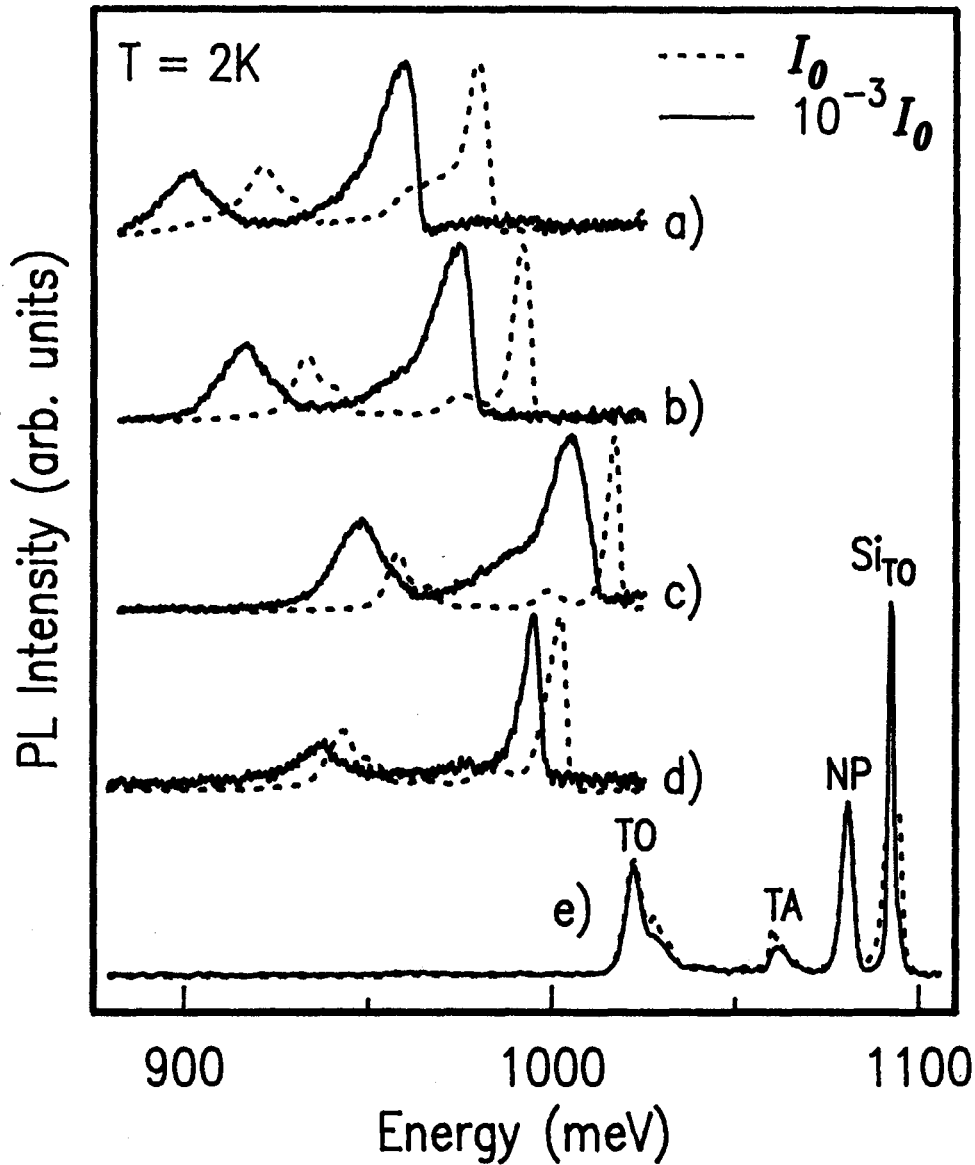
Figure 5.5 PL spectra for CVD $Si_{0.8}Ge_{0.2}$ single quantum wells with thicknesses of a) 83, b) 58, and c) 33 Å, and for very thin quantum wells, d) CVD 15 Å $Si_{0.65}Ge_{0.35}$ and e) MBE 12 Å $Si_{0.62}Ge_{0.38}$. Spectra are shown under conditions of high (I_0) and low (I_0^{-3}) excitation density, where I_0 is of the order of a few W cm^{-2}. The spectra have been scaled to give equal intensity for the SiGe NP peaks. The line labeled Si_{TO} is due to the Si substrate.

observable shift or broadening of the spectral features over six orders of magnitude change in the excitation power density. Since, as will be shown later, the LE process still exists in this sample, the LE binding energy relative to the other near band gap PL must by close to zero.

The decrease in the LE binding energy with decreasing well thickness may be a consequence of the exciton confinement. As the exciton is increasingly constrained to move in two dimensions (i.e. in the plane of the quantum well) rather than in three, the likelihood of it hopping or tunneling to the deeper alloy fluctuations within its finite lifetime is reduced. Instead the exciton becomes trapped at whichever localization center is nearby. Since shallow localization centers are much more abundant than deep ones (the density of states decreases exponentially with energy, see section 4.3), the excitons occupy predominantly shallow localization centers. The LE PL band in the thin quantum wells peaks therefore is expected to peak at higher energy than in the thicker layers. In the thin wells there is also the increased likelihood of the hole being further localized due to short range fluctuations in well thickness. However, control in well interfaces to monolayer resolution, as in III-V heterostructures (see for example the review by Herman *et al.* [91H]), would be needed to separate the effects due to the alloy disorder and the well thickness fluctuations. Note also that the situation in most other systems, such as AlGaAs/GaAs, is simpler because the alloy material makes up the barrier and not the well region. For the present study we simply consider the localized exciton recombination, without specifying which mechanism (Ge fraction or well width fluctuations) is responsible for this localization.

Despite the difference in the spectral dependence of the thin quantum well PL on excitation power density, the variation in the overall PL intensity is quite similar to the thick well case. This is shown in Figure 5.6 where the PL intensity is plotted over nearly seven orders of magnitude in power density. At extremely low powers there is an approximately linear increase in PL intensity with increasing power for both the MBE and
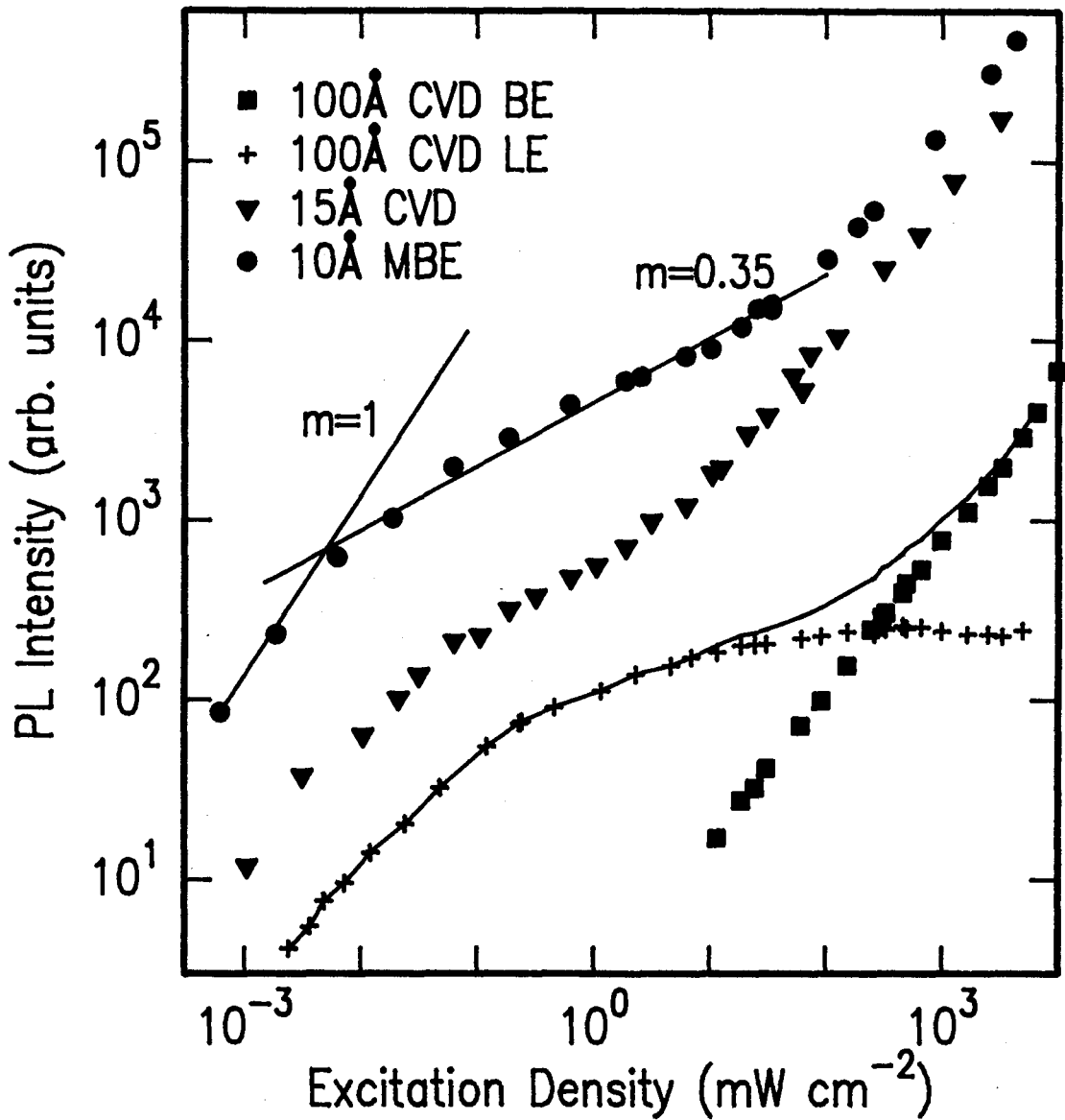
Figure 5.6 Dependence of PL intensity on excitation density for the MBE 12 Å $Si_{0.62}Ge_{0.38}$ sample (●) and the CVD 15 Å $Si_{0.65}Ge_{0.35}$ single quantum well (▼) is compared to the separate LE (+) and BE (■) intensities of the CVD 100 Å $Si_{0.75}Ge_{0.25}$ sample. The linear (m=1) power dependence observed at extremely low power densities becomes sublinear (m=0.35) at a power density comparable with that leading to saturation of the LE PL in the thick CVD quantum well. The curves for the three samples have been shifted vertically for clarity.

CVD thin quantum wells, and for the LE PL of the relatively thick (100 Å) CVD well studied in the previous chapter. The thin well PL intensities become sublinear at a very low excitation density, which is in agreement with the onset of saturation ($\sim 10 \ \mu W \ cm^{-2}$) of the LE PL in the thick CVD samples. After this sublinear region, the PL intensity again approaches a linear dependence on power level at high excitation densities. For the thick CVD well, in which the power dependence of the LE and BE features were tracked separately, this would correspond to a linear increase in the BE intensity with the LE remaining constant at its saturated value. The sum of the intensities of the LE and BE PL in the thick well (shown by the solid curve) shows a power dependence very similar to that in the thin wells, suggesting that the LE PL is present but is not resolved from the BE simply due to its small binding energy. Extrapolating between low and high power densities, the low excitation PL process in the thin wells has a PL efficiency several orders of magnitude higher than that of the high excitation process, consistent with the high quantum efficiency of the LE process observed in the thicker layers (see section 4.3). Similar power dependence curves were observed by Wachter *et al.* [92W] for their MBE quantum wells, although measurements were not taken to low enough power density to observe the return to linear power dependence below the LE saturation.

Further evidence that the PL in the thin quantum wells arises from similar processes to those in the thicker wells is provided by transient PL decay curves. Figure 5.7 shows a series of PL decay curves for the MBE 12 Å $Si_{0.62}Ge_{0.38}$ quantum well sample. Under conditions of low excitation density (bottom curve) the near band gap PL is found to decrease with a single exponential decay of 750 μsec. This is several orders of magnitude longer than typical BE or FE lifetimes for Si, which for the FE case are limited by capture onto impurities. Instead, it approaches the millisecond lifetimes which were measured for the LE PL in the thick CVD wells. The long LE lifetime is attributed to the elimination of fast nonradiative channels by the localization of the excitons, which prevents their capture by impurities. As the excitation density is increased, an additional fast component
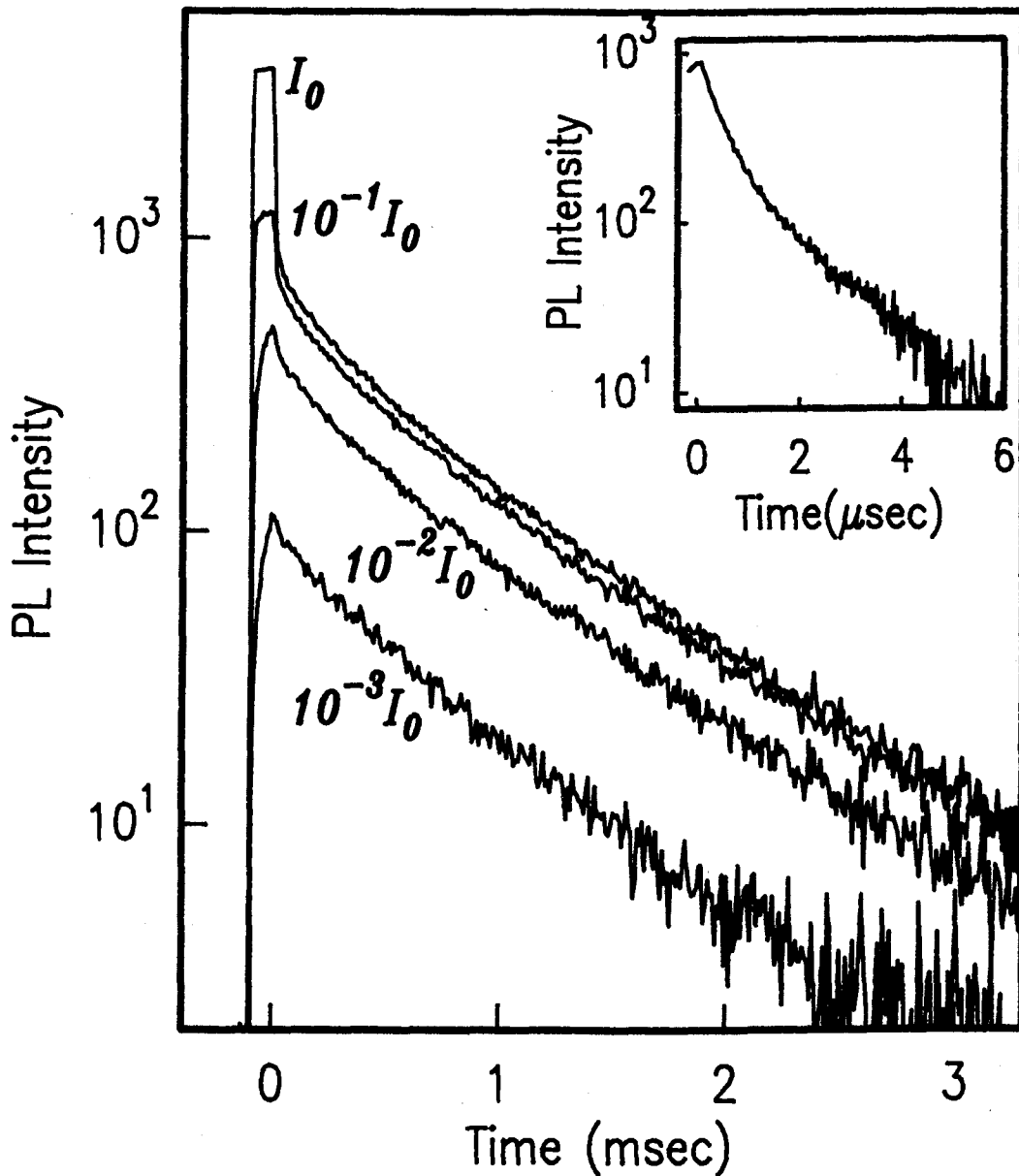
Figure 5.7 Time decay of the PL from the MBE 12 Å $Si_{0.62}Ge_{0.38}$ sample. As the excitation power density is increased by a factor of 1000 the contribution from the slow component ($\tau \sim 750$ μsec) is observed to saturate, while that from the fast component increases. The inset shows the double exponential dependence ($\tau \sim 350$ nsec, $\tau \sim 1.5$ μsec) of the fast component on an expanded time scale. The four decay curves have <u>not</u> been shifted vertically.

appears, whose intensity is observed to increase with increasing power, while that of the slow process saturates. As shown in an expanded time scale in the inset of Figure 5.7, the fast decay is described by a double exponential with lifetimes of about 350 nsec and 1.5 μsec. The relative intensities of these two components were also found to vary somewhat with excitation density. However, both lifetimes are consistent with recombination for which nonradiative channels compete with radiative ones, and so might include BE or biexcitons. These fast decay times are comparable to those of the band gap PL in thick CVD SiGe quantum wells which was attributed to BE. While the intensity of the fast PL increases steadily with increasing power, the contribution from the very slow (750 μsec) component is near saturation at the highest power level (top curve).

Thus, even though the PL spectrum does not appear to change, the near gap PL of the very thin QW samples is dominated by species which recombine via a long lifetime, highly efficient LE process at low excitation densities and by another species with a much less efficient, ~ 1 μs lifetime process at high excitation density.

5.4. Determination of Band Alignment

Having obtained a good understanding of the effect of confinement on the PL energies for single SiGe quantum wells, we now consider the question of the conduction band offset. To do this we take advantage of PL spectroscopy in determining very accurately the relative positions of the conduction and valence band edges (to within the BE + FE energy). Type I versus type II band alignment can be distinguished by comparing the BE PL energy of a single quantum well structure with that for a unique quantum well structure, which is termed a "stepped quantum well" (STQW) [93Sa]. This is depicted schematically in Figure 5.8. The stepped quantum well consists of a single

Type I hv(SQW) = hv(STQW)
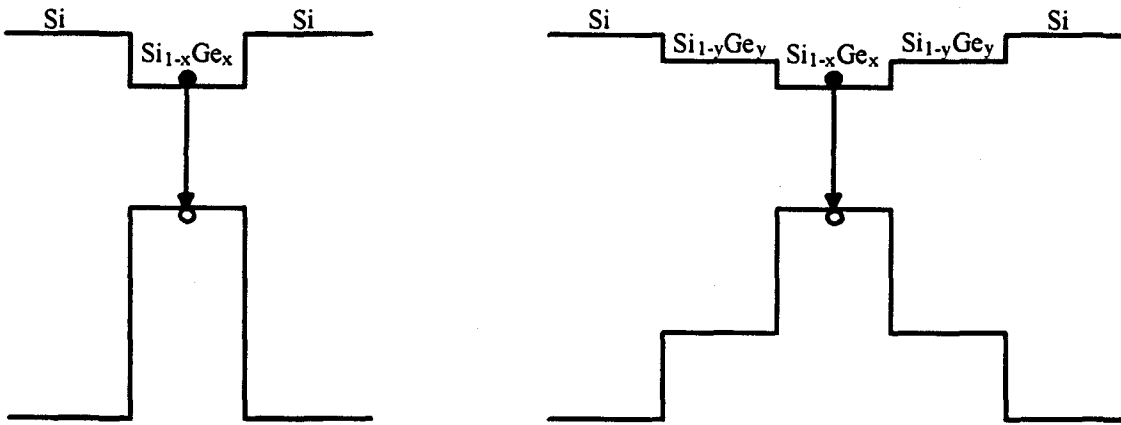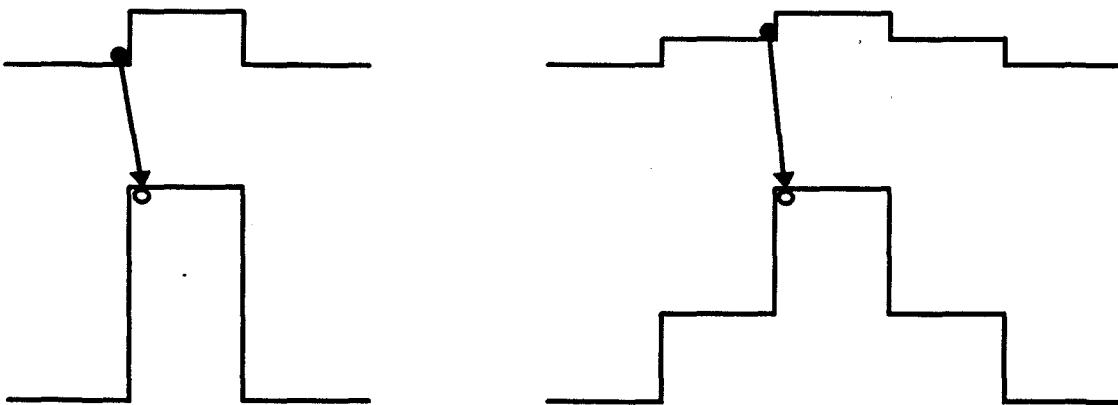
Type II hv(SQW) < hv(STQW)

Figure 5.8 Schematic depiction of type I and type II band offsets for single quantum wells (SQW) and stepped quantum well (STQW) structures.

$Si_{1-x}Ge_x$ quantum well which is surrounded on either side by "cladding" layers which have Ge composition (y) intermediate between that in the quantum well and in the Si barrier $(x > y > 0)$. Because the carriers proceed to the region of lowest energy, for type I band alignment both electrons and holes are confined to the central quantum well region $(Si_{1-x}Ge_x)$ and the PL energies of the SQW and STQW structures are identical. On the other hand, if the band alignment is type II, then for the SQW the holes confined in the quantum well $(Si_{1-x}Ge_x)$ recombine with the electrons in the <u>Si layers</u>, while for the STQW the holes confined in the central quantum well region $(Si_{1-x}Ge_x)$ recombine with electrons in the <u>cladding layers</u> $(Si_{1-y}Ge_y)$. Electrons in the Si layers are not expected to recombine with holes in the central quantum well region $(Si_{1-x}Ge_x)$ because they are spatially separated by the $Si_{1-y}Ge_y$ cladding layers of 100 Å thickness. This means that type II alignment is indicated if the BE PL energy for the SQW is different than that for the STQW. Note however if the conduction band offset between the cladding layer and the Si is very small, then type II alignment of the central quantum well cannot be distinguished from type I. The most that can be concluded for identical SQW and STQW PL energies is therefore that the alignment is either type I up to Ge fraction x <u>or</u> the band offset up to at least Ge fraction y is very small.

The two sets of SQW/STQW samples which were studied are summarized in Table 5.2. The first set consists of nominal Ge fractions of x=0.2 and y=0.14, and the second of x=0.35 and y=0.2. All quantum wells are greater than 100 Å in thickness, so that quantum confinement shifts can be neglected. Within consecutive crystal growth runs, the variation in the Ge fraction from wafer to wafer is typically less than 0.005, which corresponds to a band gap variation of less than 5 meV [93Sa]. This 5 meV variation therefore sets the limit on the uncertainty in the relative conduction to valence band energy. The uncertainty in the PL energies is about ± 1 meV. Typical well-resolved band edge BE PL was observed for all four samples. NP peaks at 994 meV and 997 meV were obtained for the x=0.2 SQW and STQW, respectively. The PL for the x=0.35 samples was slightly deeper

Table 5.2 Stepped quantum well PL energies

	x	y	PL Energy (meV)
SQW	0.2	-	994
STQW	0.2	0.14	997
SQW	0.35	-	906
STQW	0.35	0.2	904

at 906 mev for the SQW and 904 meV for the STQW. These energies agree well with the expected x=0.2 and x=0.35 strained SiGe excitonic band gap energies (see equation 4.2).

Each pair of SQW/STQW PL energies are identical within the 5 meV uncertainty expected for the wafer-to-wafer variations in x. From the x=0.35 SQW/STQW set we therefore conclude that the alignment is a) type I for x up to 0.35 or b) the alignment is type II for x=0.35 and there is negligible conduction band offset between the cladding layer (y=0.2) and the Si. Both of these possibilities are consistent with the identical PL energies observed for the x=0.2 SQW/STQW set. However, if x=0.35 is type II relative to Si then the spatial separation of the electron and hole should lead to a substantially different PL efficiency compared to the type I or zero band offset conditions in the x=0.2 SQW. Since no substantial difference in the PL efficiencies was observed, this leads us to suggest a type I alignment for Ge fraction up to x=0.35, or a type II offset of less than 5 meV (which cannot be ruled out due to the uncertainty introduced by the wafer-to-wafer variation in Ge fraction).

5.5. Tunneling through Si barriers

Given the importance of tunneling in device applications, a PL study of tunneling is the next objective. Similar measurements have proven invaluable in understanding tunneling phenomena in other materials systems. While p-type SiGe/Si resonant tunneling diodes have been demonstrated by several groups [92C, 92G, 89L], because of the complicated valence band structure for strained SiGe on Si, convincing identification of the observed resonance peaks with calculated bound state energies has not yet been made. Magneto-tunneling experiments have suggested the importance of band mixing and the strain induced splitting of the light and heavy hole states in these structures [92C, 92G, 89L]. Recently, hole band mixing has also been proposed to be essential in determining hole transfer in GaAs/(Ga)AlAs heterostructures[89B,89Wa]. In this section evidence obtained by PL spectroscopy of tunneling between SiGe quantum wells through Si barriers is presented. The measurements are carried out on asymmetric coupled quantum well structures. The wells couple only through some non-resonant process since the energy levels in the different wells are not in resonance (see section 1.4). The PL provides a direct measure of tunneling since most of the photogenerated carriers originate in the Si substrate and migrate to the nearest SiGe well where, in the absence of tunneling, they became trapped. At high temperatures thermal hopping of excitons over the Si barriers to reach the inner quantum well is also observed .

The tunneling structures were made up of three RTCVD SiGe quantum wells, each 100 Å in thickness, and consisting of two shallow wells with a nominal Ge fraction of $x \sim$ 0.13 on either side of a deep well having $x \sim 0.25$. The Si barriers between each of the wells were varied in thickness from 40 to 250 Å. An energy level diagram for hole states in the shallow and deep wells, assuming no coupling between them, is given in Figure 5.9. The heavy hole levels can be calculated as described earlier in this chapter. However, coupling of the bands must be taken into account for the light hole levels. These were
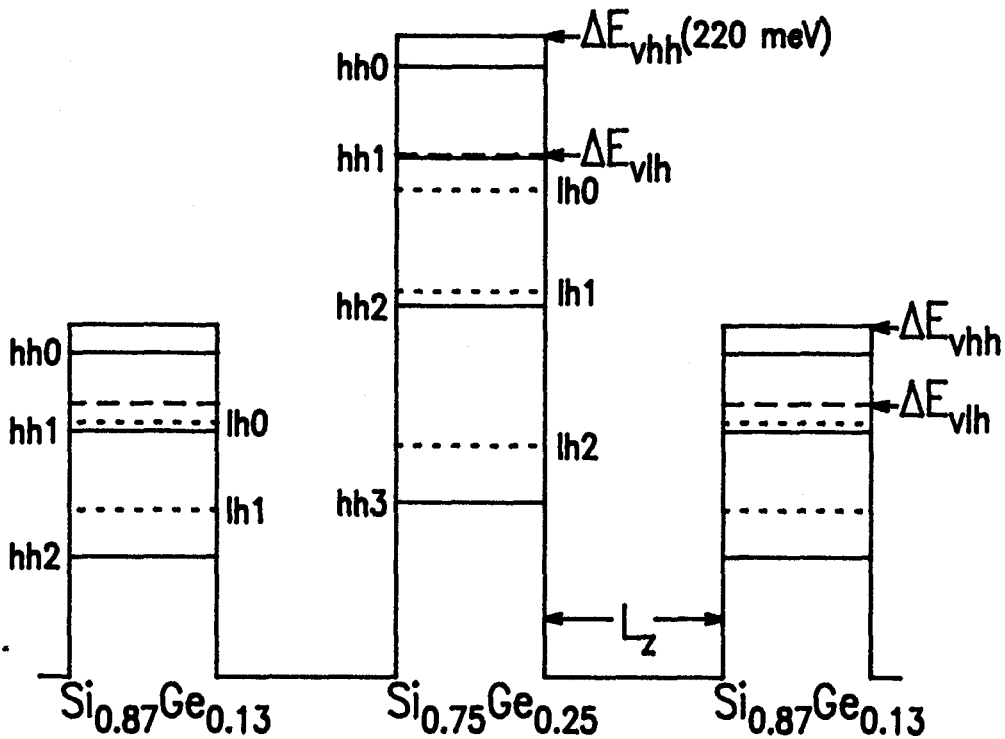
Figure 5.9 Energy level diagram for heavy hole (solid lines) and light hole (dashed lines) states relative to the excitonic band edges in the triple well structures, assuming no coupling between the wells. The Si barrier width is indicated by L_z.

calculated by X. Xiao at Princeton University using the 6x6 Luttinger-Kohn Hamiltonian described in our paper [92X]. The conduction band offsets were taken to be zero, while the valence band offsets were determined from the observed PL peaks, assuming recombination from the heavy hole ground state.

Figure 5.10 shows PL spectra for triple quantum well structures with Si barriers of a) 150, b) 120, c) 90, and d) 40 Å. The PL features can be identified with shallow bound exciton luminescence from excitons confined in either the deep ($x = 0.25$) or shallow ($x = 0.13$) quantum wells. The observed NP peaks at about 1044 meV and 946 meV agree with the excitonic band gaps expected for the shallow ($x = 0.13$) and deep ($x = 0.25$) quantum wells, respectively (see equation 4.2). Note that for barriers thicker than 90 Å there is no deep (center) well luminescence, while for barriers thinner than 90 Å there is no shallow (outer) well luminescence. Luminescence from both the deep and shallow wells

can be seen in the sample having 90 Å barriers.

These SiGe/Si structures consist of only three thin quantum wells, so very little of the Ar excitation is absorbed within the SiGe layers themselves. Instead, most of the photo-created carriers originate in the Si substrate and cap layers, and some of these carriers subsequently migrate to the SiGe well regions. The deep well PL in the spectra of Figure 5.10 (curves c and d) arises from carriers which have tunneled from the shallow wells through the Si barriers. Too few excitons are directly generated by the Ar excitation within the center SiGe well to expect a PL signal in the absence of transport from the outer wells. This contrasts with direct gap semiconductors where the stronger above gap absorption results in a large number of carriers created near the surface, within the wells themselves and in adjacent barrier regions. In such cases all the wells luminesce, so that usually a bias is needed to create conditions for resonant tunneling to enhance the PL signal from individual wells (see for example Bastard *et al*. [89B]). In our tunneling structures the carriers are expected to effectively equilibrate in the shallow outer wells, and any reaching the deep center well arrive there only by tunneling at low temperature or by thermal excitation over the Si barriers at higher temperatures. This means that the PL intensity of the deep well is a direct indication of the tunneling or thermal hopping rate. Note that at low temperatures the photo-excited carriers quickly relax to the band edges, eliminating the possibility of resonant scattering by the outer wells.

The presence of the deep well in the samples having barriers too thick to allow tunneling can be investigated by thermally exciting carriers out of the shallow wells. Figure 5.11 shows the evolution from shallow to deep well PL as the temperature is raised from 77 to 120 K for a sample having no observed tunneling (Si barriers of 250 Å). Here the excitons trapped in the shallow wells acquire enough energy to thermally hop into the Si barriers and subsequently become captured by the deep well. The Arrhenius plot in the inset indicates an activation energy of the deep well PL of 145 meV, where the variation in the density of states with temperature was negected. This corresponds roughly to the
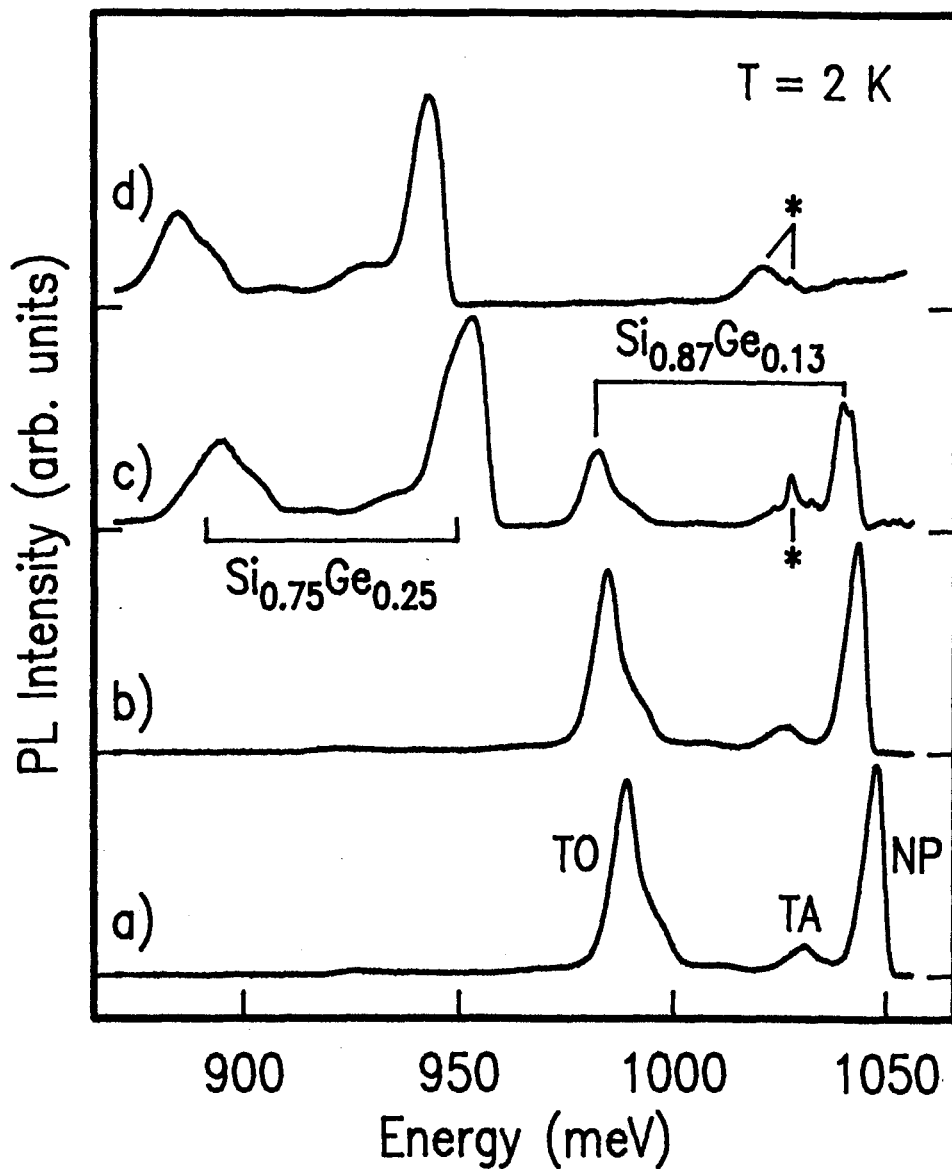
Figure 5.10 Shift from outer well to center well luminescence with variation in Si barrier width. The outer well PL, labelled $Si_{0.87}Ge_{0.13}$, is seen for a) 15, b) 12 and c) 9 nm. In d) 4 and c) 9 nm, the barriers are thin enough to allow tunneling so that the center well PL (labelled $Si_{0.75}Ge_{0.25}$) is observed. The starred features originate from the Si substrate.
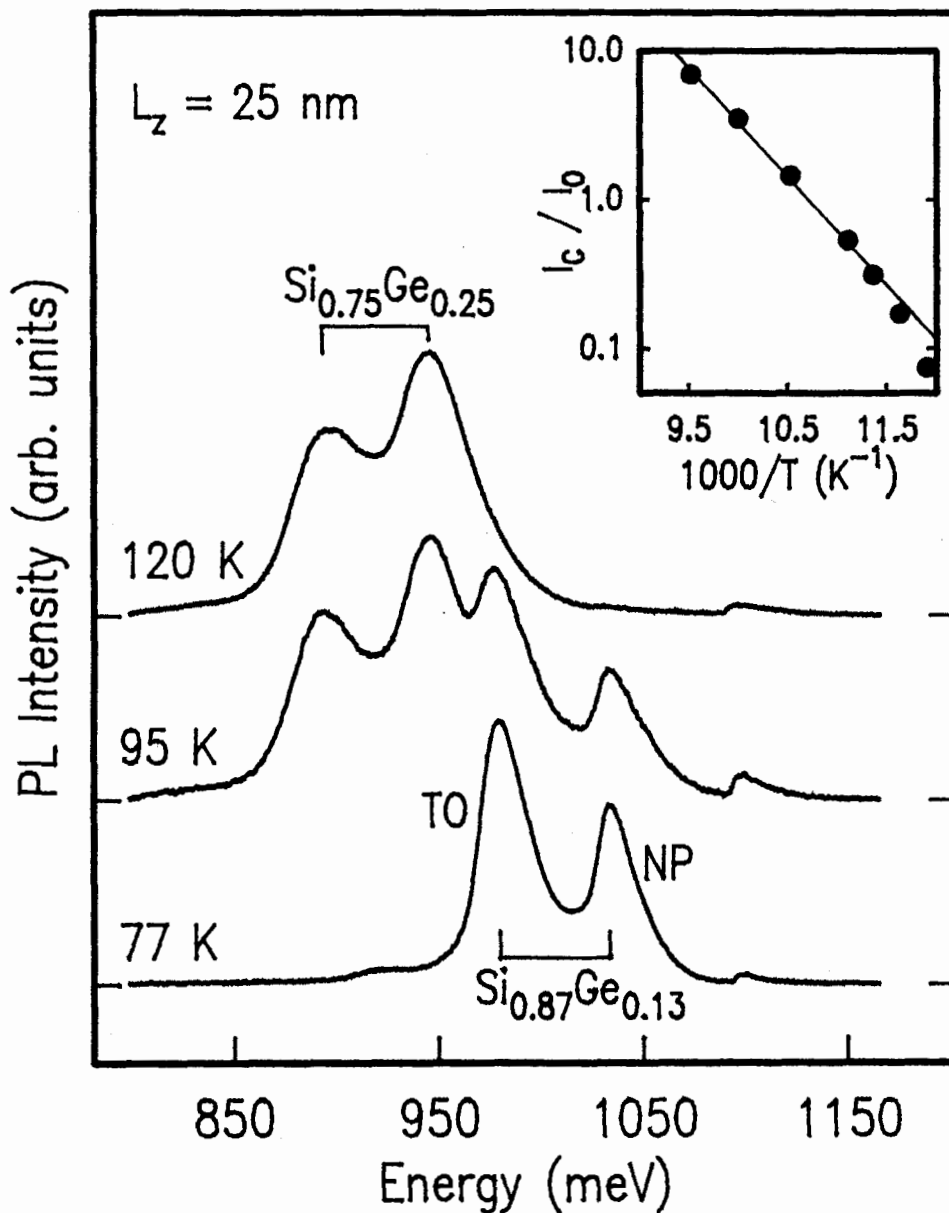
Figure 5.11 Evolution of center well ($Si_{0.75}Ge_{0.25}$) PL as the outer well ($Si_{0.87}Ge_{0.13}$) is depopulated by increasing the temperature from 77 to 95 K, then 120 K in a sample with no observed tunneling (25 nm Si barriers). The inset shows an Arrhenius plot of the center well TO intensity (I_{TO}) normalized by the outer well NP peak (I_{NP}). A fit to the data gives an activation energy of 145 meV, roughly in agreement with depth of the outer well as observed in the PL (132 meV).

depth of the heavy hole ground state in the shallow well relative to the Si barriers, as measured by the PL shift of 132 meV for this sample. (This particular sample had somewhat deeper PL from the outer wells than those shown in Figure 5.10, likely due to an increased Ge fraction from the nominal 13% value.) This temperature dependence confirms that the photo-excited carriers are initially trapped in the shallow outer wells at low temperatures.

The time decay of the shallow well luminescence at low temperatures was faster in structures having narrow Si barriers, since in addition to radiative and nonradiative channels, carriers escape the wells by tunneling. Lifetimes of $\tau_{90Å}$~210 ± 40 ns and $\tau_{120Å}$ ~600 ± 100 ns were obtained as shown in Figure 5.12 for samples at 4.2 K with nominal Si barriers of a) 90 and b) 120 Å, which correspond to the cases discussed above of some tunneling (Fig. 5.10 c) and no observed tunneling (Fig. 5.10 b), respectively. The errors in the lifetime values reflect variations in the decay curves with excitation power. The PL decay from the sample with the 150 Å barriers (Fig. 5.10 a) was comparable to that observed for the 120 Å barriers.

As evident by the less than 50 ns rise times in Figure 5.12, the transport of carriers from the Si into the outer well occurs on a much faster time scale than the outer well PL decay. This is expected, given that in Si the free exciton capture rate by impurities is very fast at liquid He temperatures, on the order of ns even in relatively pure samples. In addition, the Si free exciton lifetime is further reduced in our structures by their capture by the SiGe wells. Very quickly after the laser pulse the free excitons either successfully diffuse the short distance to the SiGe wells or become trapped in the substrate as bound excitons. The observed lifetime for the samples with the thick barriers (600 ns) is therefore associated only with the dynamics of nonradiative and radiative processes intrinsic to the outer wells. Assuming that these same processes occur in the outer wells of the 90 Å barrier samples, the outer well PL decay time is simply reduced by the

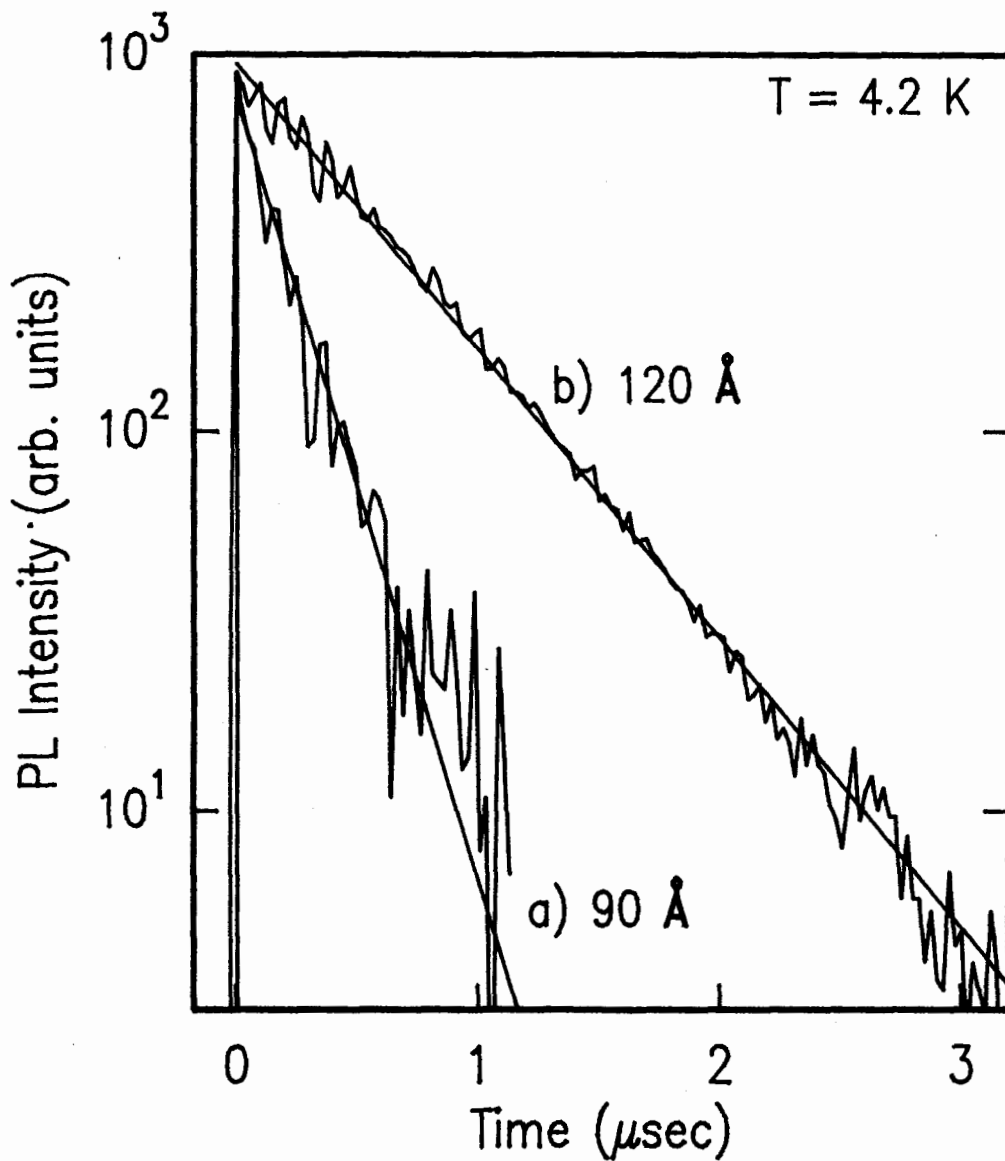**Figure 5.12** Time decay of the outer well PL ($Si_{0.87}Ge_{0.13}$) for a) 90 Å Si barriers is faster than for b) 120 Å Si barriers, consistent with the evidence of tunneling in the PL spectral features (Fig. 5.10). The solid lines show fits to the data which correspond to lifetimes of a) 210 ns and b) 575 ns. The PL intensities have been scaled to give equal values at t=0.

tunneling through the barrier:

$$\frac{1}{\tau_{90A}} = \frac{1}{\tau_{tun}} + \frac{1}{\tau_{120A}} \qquad\qquad (5.3)$$

Substituting our measured values we get a tunneling escape rate from the shallow wells of $\tau_{tun} \sim 325 \pm 100$ ns for the 90 Å Si barriers. These rates suggest that approximately twice as many excitons escape to the center well by tunneling ($\tau_{tun} \sim 325$ ns) as remain in the outer well ($\tau_{120A} \sim 600$ ns). This is roughly in agreement with the observed relative intensities of the outer and center well PL (Figure 5.10, curve c), assuming that the radiative efficiencies of the wells are similar. Note that the tunneling escape rate is related simply to the tunneling attempt frequency and the probability of tunneling. This should not be confused with the actual tunneling time (i.e. the time to traverse the barrier in the case of successful tunneling), which is a fundamental quantum mechanical concept. Such slow tunneling rates have not been measured in quantum wells of direct gap semiconductors [89B,92Fb] due to the much shorter radiative lifetimes. The long exciton lifetime in SiGe/Si allows for a larger number of tunneling attempts so that tunneling is observed despite conditions, as discussed below, of very low transmission probability.

It is unlikely that the limiting tunneling process is due to electrons since the conduction band offset is known to be very small (≤ 50 meV, see section 1.3) for $x < 0.25$. While time-resolved PL spectroscopy might prove useful in detecting whether any of the recombining excitons having spatially separated electrons and holes, for this preliminary study we simply pressume that the presence of the deep PL is determined by either hole or exciton tunneling. The question of whether the excitons tunnel as a whole or each particle arrives separately is still under study even in GaAs/AlGaAs [92Fb]and we will not attempt any discussion here.

Another issue is whether the tunneling occurs by a resonant or a non-resonant process. Without the added degree of freedom of an applied bias, it is unlikely that occupied eigenstates in the shallow well will be coincidentally resonant in energy with

levels in the deep well. The tunneling probability can in principle be calculated by solving the Schrödinger equation for the coupled well eigenstates. However, this is very sensitive to the energy levels in the two isolated wells (i.e. the effective masses and band offsets). The tunneling probability can change by orders of magnitude when the energy levels move only slightly off-resonance so that, unless the eigenstates are accurately known, we can get misleading results. Instead the expected coupling between the wells can be predicted by calculating the transfer integrals for the two isolated well eigenstates with energy separation ΔE, to determine the strength of the well coupling constant λ_c. This is defined by $\lambda_c = (\lambda_1 \lambda_2)^{1/2}$, where the transfer integrals λ_1 and λ_2 are the inner products of the isolated x=0.25 and x=0.13 eigenstates integrated over the center and outer well regions respectively and weighted by the depth of the well [89B]:

$$\lambda_1 = V_{0.25} \langle \psi_{0.25} | \psi_{0.13} \rangle_{\text{center well}}$$

$$\lambda_2 = V_{0.13} \langle \psi_{0.13} | \psi_{0.25} \rangle_{\text{outer well}} \quad\quad\quad (5.4)$$

The coupling constant accounts qualitatively for the size of the carrier effective mass, the barrier width and the height of the eigenstates relative to the barrier. The condition for appreciable resonant tunneling is that $2\lambda_c \gg \Delta E$ [89B]. For simplicity we assume that the light holes states in the shallow quantum well (initial state) are unoccupied and neglect any coupling between the hole bands. This is consistent with the observation of Figure 5.11 that the deep well PL activation energy corresponds roughly to the shallow well depth for heavy holes. For heavy hole tunneling between the shallow well heavy hole ground state and the two nearest deep well heavy hole states, n = 2 and 3, we obtain $2\lambda_c$ ~ 0.003 meV and 0.012 meV respectively for Si barriers of 90 Å. Since it is unlikely that the eigenenergies of the two wells are accidentally tuned to within this amount, we speculate that the tunneling occurs by some non-resonant scattering process. However as discussed at the beginning of this section, the situation is considerably more complicated than outlined above, with the likelihood of there also being some enhanced hole tunneling due to mixing between the light and heavy hole bands.

5.6. Summary and Discussion

Quantum confinement shifts in the BE PL spectra were observed for single $Si_{0.8}Ge_{0.2}$ quantum wells on Si and found to agree with calculations based on the envelope function scheme. The confinement shift was assumed to be due to the shift in only the heavy hole valence band edge, which for the relevant k values (i.e. $k_\perp = 0$) decouples from the other valence bands. The problem reduced to solving the Schrödinger equation, with a good fit to the data obtained for a valence band offset of 188.2 meV (for x=0.2). The relative heights of the Si-Si and Si-Ge phonon replicas were also found to be related simply to the leakage of the envelope functions into the barrier regions.

• Besides the shift in the BE PL spectra with confinement, we observed somewhat different behaviour for the LE PL in these samples than in the thicker layers of Chapter 4. Although the near band gap PL spectral features of the thin SiGe quantum wells did not change in an obvious way from a BE peak to a LE peak with decreasing excitation density (as for the thick layers), two physically different processes are at work at low and high excitation levels. Based on the behaviour of the PL intensity with excitation power density and the PL lifetime, the spectra at moderate to low excitation levels were shown to still be consistent with the localized exciton model of Chapter 4.

The typical near band gap PL of SiGe quantum wells at liquid He temperatures has been assigned to BE (see Chapter 4) and/or FE [92R, 92Sa, 91D]. However, it is questionable whether free excitons exist in these systems at $T \leq 4.2$ K even in the absence of impurities. The half-width of the band gap fluctuations due to alloy disorder, averaged over an excitonic volume, are at least a few meV, or in other words much larger than kT (~ 0.5 meV). Thus in pure material at $T \leq 4.2$ K, and at low excitation density we should have LE rather than FE. The presence of donors and/or acceptors can result in BE as well. This is clearly observed in the double NP peak shown in Figure 4.2 (with similar spectral features seen by Robbins *et al.* [92R], Spitzer *et al.* [92Sa], and Wachter *et al.*

[92W]). One peak therefore arises from BE, and the other from LE at liquid He temperature or FE at slightly elevated temperatures. On the other hand, a purely LE line at low T would evolve smoothly into the Maxwell-Boltmann lineshape typical of FE as the temperature is increased, without ever producing a double-peaked structure.

In fact, the 12 Å MBE sample studied here did not show a double-peaked NP line anywhere from 2 K to 60 K, independent of excitation density. This raises the possibility that the high excitation PL is not predominantly due to BE, yet it is clearly different from the LE PL. Another possibility might be (localized) biexcitons, which would still be stable in the strained alloy and would have a ~ 1 meV binding energy [84T] relative to the LE, explaining the lack of an observable spectral shift between low and high excitation. The biexciton, unlike the LE, does have a nonradiative Auger decay channel, and thus would have the necessary shorter lifetime and lower PL quantum efficiency. Both biexcitons and BE are possible explanations for the high excitation process, and the ratio of the two species will depend on the impurity concentrations. It is tempting to ascribe the two different fast decay times observed in the thin MBE sample (inset of Figure 5.7, $\tau \sim$ 350 ns and 1.5 μs) to BE and biexcitons, but further study is necessary. A spectroscopic method [84T] which is specifically sensitive to multi-exciton species such as the biexciton is currently underway.

Having observed the effects of confinement on the PL spectra, we also considered whether both the electron and hole of the exciton are confined together in the SiGe layer. Comparing the PL energies of single quantum wells with special stepped quantum well structures we obtained direct evidence that within 5 meV the band alignment is type I (i.e. both carriers are confined to the SiGe) for $x \leq 0.35$. Finally, PL spectroscopy was used to observe tunneling between SiGe quantum wells through Si barriers. Because most of the photo-generated carriers originated in the Si substrate, the PL intensities from the different quantum wells provided a direct measure of the tunneling. Despite the unlikelihood of resonance due to the asymmetry in these structures, the tunneling occured through

remarkably thick (90 Å) Si barriers. This may be due to the very long exciton lifetime and suggests SiGe/Si is an ideal system in which to further study non-resonant tunneling processes and hole band mixing.

In conclusion, PL spectroscopy has been used in this thesis to gain insight into SiGe/Si heterostructures. As is already the case for other semiconductor heterostructure systems, the ability to observe well-resolved band edge luminescence will undoubtedly prove to be an important tool in developing SiGe/Si devices.

Appendix

Hamiltonian for $Si_{1-x}Ge_x$ Quantum Wells

The Hamiltonian for a single strained SiGe quantum well with Si barriers is described below. For $\mathbf{k}_\perp = 0$ the heavy hole band is shown to decouple from the other bands so that the one band effective mass model (equation 1.3) applies. This equation is used in Chapter 5 to obtain the energy eigenvalues for a series of SiGe SQWs.

The valence band states in Si and Ge can be described by p_x, p_y, and p_z atomic orbitals plus the spin degrees of freedom (i.e. spin up $\uparrow$ or spin down $\downarrow$). At the top of the valence band we therefore have 6-fold degeneracy. However as discussed in section 1.2, this degeneracy is split by spin-orbit coupling to give the fourfold degenerate (at k=0) heavy and light hole bands and the two-fold degenerate split-off band. Because of the mixing of p states by the spin-orbit coupling it becomes more convenient to describe the states in terms of the total angular momentum basis, rather than the $p_x \uparrow$, $p_x \downarrow$, $p_y \uparrow$, $p_y \downarrow$, $p_z \uparrow$, and $p_z \downarrow$ basis. The total angular momentum basis is denoted by $|j, m>$ where j is the quantum number for the operator $\mathbf{J} = \mathbf{L} + \mathbf{S}$, and m is the projection of $\mathbf{J}$ along the z-axis. The six valence band states are written $|3/2, +3/2>$, $|3/2, -3/2>$, $|3/2, +1/2>$, $|3/2, -1/2>$, $|1/2, +1/2>$, and $|1/2, -1/2>$. The heavy hole states correspond to $|3/2, \pm3/2>$, the light hole to $|3/2, \pm1/2>$, and the split off band to $|1/2, \pm1/2>$. It is important to realize that this description of j and m for the hole states only applies at k=0. For k≠0 the m=3/2 and m=1/2 states mix strongly. This is obvious if we take a look at the $\mathbf{k \cdot p}$ Hamiltonian.

The Hamiltonian for the valence band states in Si and Ge (and also SiGe) is best described in the form given by Luttinger and Kohn [55L], where the effect of the two conduction band states is incorporated in the fitting parameters (i.e. the Luttinger parameters) and we retain only the six valence band states:

$$H_{k\cdot p} = -\begin{array}{cccccc}
\left|\tfrac{3}{2}\tfrac{3}{2}\right\rangle & \left|\tfrac{3}{2}\tfrac{1}{2}\right\rangle & \left|\tfrac{3}{2}\tfrac{-1}{2}\right\rangle & \left|\tfrac{3}{2}\tfrac{-3}{2}\right\rangle & \left|\tfrac{1}{2}\tfrac{1}{2}\right\rangle & \left|\tfrac{1}{2}\tfrac{-1}{2}\right\rangle
\end{array}$$

$$H_{k\cdot p} = -\begin{bmatrix}
H_{hh} & b & c & 0 & \dfrac{ib}{\sqrt{2}} & -i\sqrt{2}c \\[2mm]
b^* & H_{lh} & 0 & c & -iq & \dfrac{i\sqrt{3}b}{\sqrt{2}} \\[2mm]
c^* & 0 & H_{lh} & -b & -\dfrac{i\sqrt{3}b^*}{\sqrt{2}} & -iq \\[2mm]
0 & c^* & -b^* & H_{hh} & -i\sqrt{2}c^* & -\dfrac{ib^*}{\sqrt{2}} \\[2mm]
-\dfrac{ib^*}{\sqrt{2}} & iq & \dfrac{i\sqrt{3}b}{\sqrt{2}} & i\sqrt{2}c & H_{so} & 0 \\[2mm]
i\sqrt{2}c^* & -\dfrac{i\sqrt{3}b^*}{\sqrt{2}} & iq & \dfrac{ib}{\sqrt{2}} & 0 & H_{so}
\end{bmatrix} \quad\text{(A.1)}$$

The elements in the Hamiltonian are given by:

$$H_{hh} = \frac{\hbar^2}{2m_0}\left[(\gamma_1 + \gamma_2)(k_x^2 + k_y^2) + (\gamma_1 - 2\gamma_2)k_z^2\right]$$

$$H_{lh} = \frac{\hbar^2}{2m_0}\left[(\gamma_1 - \gamma_2)(k_x^2 + k_y^2) + (\gamma_1 + 2\gamma_2)k_z^2\right]$$

$$H_{so} = \frac{H_{hh} + H_{lh}}{2} + \Delta_0 \qquad\qquad q = \frac{H_{hh} - H_{lh}}{\sqrt{2}}$$

$$b = \frac{-\sqrt{3}i\hbar^2}{m_0}\gamma_3(k_x - ik_y)k_z \qquad\qquad c = \frac{\sqrt{3}\hbar^2}{2m_0}\left[\gamma_2(k_x^2 - k_y^2) - 2i\gamma_3 k_x k_y\right]$$

where γ_1, γ_2, γ_3 are the Luttinger valence band parameters and Δ_0 is the spin-orbit splitting, as listed below for Si and Ge.

Table A.1 Valence Band Parameters for Si and Ge (from Robbins et al. [92R])

	γ_1	γ_2	γ_3	Δ_0
Si	4.22	0.39	1.44	44 meV
Ge	13.35	4.25	5.69	290 meV

The values for these parameters can be approximated for the $Si_{1-x}Ge_x$ alloy simply using a linear interpolation between the pure Si and pure Ge values. When the spin-orbit coupling is small, as in Si, then the terms in the Hamiltonian which couple the j=3/2 states to the j=1/2 states are neglected. The problem then reduces to two separate matrices, the upper left 4x4 matrix and the lower right 2x2 matrix of equation A.1.

For the case of a SiGe quantum well, the strain introduced in the SiGe layer by growing it epitaxially on the Si substrate must also be taken into account. We are primarily concerned with the uniaxial stress since it mixes the light hole and split-off bands, as described by the strain Hamiltonian [63H, 85Pa]:

$$H_u = \begin{array}{c} \begin{array}{cccccc} \left|\tfrac{3}{2}\tfrac{3}{2}\right\rangle & \left|\tfrac{3}{2}\tfrac{1}{2}\right\rangle & \left|\tfrac{3}{2}\tfrac{-1}{2}\right\rangle & \left|\tfrac{3}{2}\tfrac{-3}{2}\right\rangle & \left|\tfrac{1}{2}\tfrac{1}{2}\right\rangle & \left|\tfrac{1}{2}\tfrac{-1}{2}\right\rangle \end{array} \\ \begin{bmatrix} \varepsilon(x) & 0 & 0 & 0 & 0 & 0 \\ 0 & -\varepsilon(x) & 0 & 0 & -\sqrt{2}\varepsilon(x) & 0 \\ 0 & 0 & -\varepsilon(x) & 0 & 0 & \sqrt{2}\varepsilon(x) \\ 0 & 0 & 0 & \varepsilon(x) & 0 & 0 \\ 0 & -\sqrt{2}\varepsilon(x) & 0 & 0 & -\Delta_0(x) & 0 \\ 0 & 0 & \sqrt{2}\varepsilon(x) & 0 & 0 & -\Delta_0(x) \end{bmatrix} \end{array} \qquad (A.2)$$

where the matrix elements are: $\varepsilon(x) = \tfrac{2}{3}D_u(x)[e_{zz}(x) - e_{xx}(x)]$

$$e_{zz}(x) - e_{xx}(x) = \left(\frac{1 + \nu(x)}{1 - \nu(x)}\right)\left(\frac{a(x) - a_{Si}}{a_{Si}}\right)$$

with values for the deformation potential of $D_u = 2.04$ eV for Si and 3.81 for Ge, for Poisson's ratio of $\nu=0.280$ for Si and 0.273 for Ge, and the lattice constants, a, as given in Chapter 1. For SiGe these parameters are treated as linear functions of x. The hydrostatic strain in the SiGe layer simply shrinks the overall band gap, as described by People, without coupling the bands together, and therefore can be easily incorporated into the Hamiltonian as diagonal terms.

To convert the separate Hamiltonians for the SiGe layer and the Si substrate and cap layers into a single Hamiltonian which describes a SiGe/Si quantum well, the procedure of

the envelope function scheme as outlined by Bastard and Brum [86B] is followed. The bulk (i.e. unstrained) Hamiltonians are defined piecewise for the SiGe and the Si regions, to this is added the uniaxial stress Hamiltonian for the SiGe, then diagonal elements to account for the bulk band offsets (ΔE_v) and the hydrostatic strain terms (E_{hyd}), and finally as the last step k_z is replaced everywhere by $-i\dfrac{\partial}{\partial z}$. The resulting Hamiltonian is then:

$$H = \begin{cases} H_{k\cdot p}\,(Si),\ z \in \text{Si barrier} \\ H_{k\cdot p}\,(SiGe)\ +\ H_u\ +\ I\,E_{hyd}\ +\ I\,\Delta E_v,\ z \in \text{SiGe well} \end{cases} \tag{A.3}$$

where I is a 6x6 unit matrix and ΔE_v is the heavy hole valence band offset for bulk (i.e. unstrained SiGe) on Si. Solving this eigenvalue problem, subject to the boundary conditions discussed in section 1.4, then gives the desired eigenenergies relative to the valence band edges.

For the case of $\mathbf{k_\perp} = 0$ (i.e. $k_x = k_y = 0$) the $\mathbf{k \cdot p}$ Hamiltonian for the bulk materials reduces to:

$$H_{k\cdot p} = -\frac{h^2}{2\,m_0}
\begin{bmatrix}
(\gamma_1 - 2\gamma_2)\,k_z^2 & 0 & 0 & 0 & 0 & 0 \\
0 & (\gamma_1 + 2\gamma_2)\,k_z^2 & 0 & 0 & i\,2\sqrt{2}\,\gamma_2\,k_z^2 & 0 \\
0 & 0 & (\gamma_1 + 2\gamma_2)\,k_z^2 & 0 & 0 & i\,2\sqrt{2}\,\gamma_2\,k_z^2 \\
0 & 0 & 0 & (\gamma_1 - 2\gamma_2)\,k_z^2 & 0 & 0 \\
0 & -i\,2\sqrt{2}\,\gamma_2\,k_z^2 & 0 & 0 & \gamma_1\,k_z^2 + \Delta_0 & 0 \\
0 & 0 & -i\,2\sqrt{2}\,\gamma_2\,k_z^2 & 0 & 0 & \gamma_1\,k_z^2 + \Delta_0
\end{bmatrix}$$

with column headings $|\tfrac{3}{2}\tfrac{3}{2}\rangle\quad |\tfrac{3}{2}\tfrac{1}{2}\rangle\quad |\tfrac{3}{2}\tfrac{-1}{2}\rangle\quad |\tfrac{3}{2}\tfrac{-3}{2}\rangle\quad |\tfrac{1}{2}\tfrac{1}{2}\rangle\quad |\tfrac{1}{2}\tfrac{-1}{2}\rangle$

This matrix is diagonal for the $|3/2, \pm 3/2\rangle$ states, so that the Hamiltonian describing the heavy hole states for the SiGe quantum well is simply:

$$H = -\frac{h^2}{2m(z)}\frac{\partial^2}{\partial z^2} + \Delta E_{v,str}\,(z \in well) \tag{A.4}$$

where the uniaxial and hydrostatic strain terms have been incorporated into the valence band offset, and the effective mass is given by $m_0 /m(z) = (\gamma_1(z) - 2\,\gamma_2(z))$.

113

References

[93G] E.R. Glaser, T.A. Kennedy, D.J. Godbey, P.E. Thompson, K.L. Wang, and C.H. Chern, Phys. Rev. **B47**, 1305 (1993).

[93K] T.A. Kennedy, E.R. Glaser, D.J. Godbey, P.E. Thompson, C.H. Chern, K.L. Wang, X. Xiao, and J.C. Sturm, submitted to J. Vac. Sci. Technol.

[93M] J.F. Morar, P.E. Batson, and J. Tersoff, Phys. Rev. **B47**, 4107 (1993).

[93Sa] J.C. Sturm, X. Xiao, L.C. Lenchyshyn, and M.L.W. Thewalt, to be published.

[93Sb] Jasprit Singh, "Physics of Semiconductors and their Heterostructures", (McGraw-Hill Inc.) 1993.

[92A] V. Arbet-Engels, J.M.G. Tijero, A. Manissadjian, K.L. Wang, and V. Higgs, Appl. Phys. Lett. **61**, 2586 (1992).

[92B] M.G. Burt, J. Phys. Cond. Matter **4**, 6651 (1992).

[92C] C.H. Chern, J.M.G. Tijero, K.L. Wang, and S.J. Wang, J. Vac. Sci. Technol. **B10**, 937 (1992).

[92D] J. Denzel, K. Thonke, J. Spitzer, R. Sauer, H. Kibbel, H.-J. Herzog, and E. Kasper, Thin Solid Films **222**, 89 (1992).

[92Fa] S. Fukatsu, H. Yoshida, N. Usami, A. Fujiwara, Y. Takahashi, Y. Shiraki, and R. Ito, Jpn. J. Appl. Phys. **31**, L1319 (1992).

[92Fb] R. Ferreira, P. Rolland, Ph. Roussignol, C. Delalande, A. Vinattieri, L. Carraresi, M. Colocci, N. Roy, B. Sermage, J.F. Palmier, and B. Etienne, Phys. Rev. **B45**, 11782 (1992).

[92G] U. Gennser, V.P. Kesan, D.A. Syphers, J.A. Ott, T.P. Smith III, S.S. Iyer, and E.S. Yang, J. Vac. Sci. Technol. **B10**, 940 (1992).

[92Na] J.-P. Noël, N.L. Rowell, D.C. Houghton, A. Wang, and D.D. Perovic, Appl. Phys. Lett. **61**, 690 (1992).

[[92Nb] M.K. Nissen, Ph.D. Thesis, Simon Fraser University (1992).

[92Nc] K. Nauka, T.I. Kamins, J.E. Turner, C.A. King, J.L. Hoyt, and J.F. Gibbons, Appl. Phys. Lett. **60**, 195 (1992).

[92O] J. Olajos, J. Engvall, H.G. Grimmeiss, U. Menczigar, G. Abstreiter, H. Kibbel, E. Kasper, and H. Presting, Phys. Rev. **B46**, 12857 (1992).

[92R] D.J. Robbins, L.T. Canham, S.J. Barnett, A.D. Pitt, and P. Calcott, J. Appl. Phys. **71**, 1407 (1992).

[92Sa] J. Spitzer, K. Thonke, R. Sauer, H. Kibbel, H.-J. Herzog, and E. Kasper, Appl. Phys. Lett. **60**, 1729 (1992).

[92Sb] T.D. Steiner, R.L. Hengehold, Y.K. Yeo, D.J. Godbey, P.E. Thompson, and G.S. Pomrenke, J. Vac. Sci. Technol. **B10**, 924 (1992).

[92Sc] F. Schäffler, D. Többen, H.-J. Herzog, G. Abstreiter, and B. Holländer, Semicond. Sci. Technol. **7**, 260 (1992).

[92Sd] D.W. Smith, C.J. Emeleus, R.A. Kubiak, E.H.C. Parker, and T.E. Whall, Appl. Phys. Lett. **61**, 1453 (1992).

[92T] K. Terashima, M. Tajima, and T. Tatsumi, American Vacuum Society Meeting, Chicago, Fall 1992.

[92U] N. Usami, S. Fukatsu, and Y. Shiraki, Appl. Phys. Lett. **61**, 1706 (1992).

[92V] L. Vescan, A. Hartmann, K. Schmidt, Ch. Dieker, H. Lüth, and W. Jäger, Appl. Phys. Lett. **60**, 2183 (1992).

[92W] M Wachter, K. Thonke, R. Sauer, F. Schäffler, H.-J. Herzog, and E. Kasper, Thin Solid Films **222**, 10 (1992).

[92X] X. Xiao, C.W. Liu, J.C. Sturm, L.C. Lenchyshyn, M.L.W. Thewalt, R.B. Gregory, P. Fejes, Appl. Phys. Lett. **60**, 2135 (1992).

[92Z] S. Zollner, R.T. Collins, M.S. Goorsky, P.J. Wang, M.J. Tejwani, J.O. Chu, B.S. Meyerson, and P.K. LeGoues, SPIE Vol. **1678**, 81 (1992).

[91D] D. Dutartre, G. Brémond, A. Souifi, and T. Benyattou, Phys. Rev. **B44**, 11525, (1991).

[91H] M.A. Herman, D. Bimberg, and J. Christen, J. Appl. Phys. **70**, R1 (1991).

[91J] D. Jesson, S.J. Pennycook, and J.-M. Baribeau, Phys. Rev. Lett. **66**, 750 (1991).

[91K] E. Kasper and F. Schäffler, in Strained-Layer Superlattices: Materials Science and Technology, ed. by T.P. Pearsall, Semiconductors and Semimetals Vol. **33**, 1991.

[91L] F.K. LeGoues, V.P. Kesan, and S.S. Iyer, Phys. Rev. Lett. **66**, 750 (1991).

[91Sa] J.C Sturm, H. Manoharan, L.C. Lenchyshyn, M.L.W. Thewalt, N.L. Rowell, J.-P. Noël, and D.C. Houghton, Phys. Rev. Lett. **66**, 1362 (1991).

[91Sb] J.C. Sturm, P.V. Schwartz, E.J. Prinz, and H. Manoharan, J. Vac. Sci. Technol.

B9, 2011 (1991).

[91Sc] B.J. Spencer, P.W. Voorhees, and S.H. Davis, Phys. Rev. Lett. **67**, 3696 (1991).

[91T] K. Terashima, M. Tajima, N. Ikarashi, T. Niino, and T. Tasumi, Jap. J. Appl. Phys. **30**, 3601 (1991).

[90B] K.W. Böer, "Survey of Semiconductor Physics", (Van Nostrand Reinhold, N.Y.) 1990.

[90E] D.J. Eaglesham and M. Cerullo, Phys. Rev. Lett. **64**, 1943 (1990).

[90H] V. Higgs, E.C. Lightowlers, G.F.A. Van de Walle, D.J. Gravesteijn, E.A. Montie, Appl. Phys. Lett. **59**, 2579 (1991).

[90M] R.A. Modavis, D.G. Hall, J. Bevk, B.S. Freer, L.C. Feldman, and B.E. Weir, Appl. Phys. Lett. **57**, 954 (1990).

[90N] J.-P. Noël, N.L. Rowell, D.C. Houghton, and D.D. Perovic, Appl. Phys. Lett. **57**, 1037 (1990).

[90P] G.L. Patton, J.H. Comfort, B.S. Meyerson, E.F. Crabbé, G.J. Scilla, E. de Frésart, J.M.C. Stork, J.Y.-C. Sun, D.L. Harame, and J.N. Burghartz, IEEE Electron Device Lett. **11**, 171 (1990).

[90S] U. Schmid, N.E. Christensen, and M. Cardona, Phys. Rev. Lett. **65**, 2610 (1990).

[90Ta] M.L.W. Thewalt, M.K. Nissen, D.J.S. Beckett, and K.R. Lundgren, Mat. Res. Soc. Symp. Proc., **163**, 221 (1990).

[90Tb] K. Terashima, M. Tajima, and T. Tatsumi, Appl. Phys. Lett **57**, 1925 (1990).

[90Z] R. Zachai, K. Eberl, G. Abstreiter, E. Kasper, and H. Kibbel, Phys. Rev. Lett. **64**, 1055 (1990).

[89B] G. Bastard, C. Delalande, R. Ferreira, and H.W. Liu, J. Lumin. **44**, 247 (1989).

[89F] A. Fried, A. Ron, and E. Cohen, Phys. Rev. **B39**, 5913 (1989).

[89L] H.C. Liu, D. Landheer, M. Buchanan, D.C. Houghton, M. D'Iorio, and Song Kechang, Superlattices and Microstructures **5**, 213, (1989).

[89O] H. Okumura, K. Miki, S. Misawa, K. Sakamoto, T. Sakamoto, and S. Yoshida, Jap. J. Appl. Phys. **28**, L1893 (1989).

[89P] T.P. Pearsall, J. Lumin. **44**, 367 (1989).

[89Wa] R. Wessel and M. Altarelli, Phys. Rev. **B39**, 12802 (1989).

[89Wb] J. Weber and M.I. Alonso, Phys. Rev. **B40**, 5683 (1989).

[89Wc] S. Wang, "Fundamentals of Semiconductor Theory and Device Physics", (Prentice-Hall International) 1989.

[88L] S. Luryi and S.M. Sze, in "Silicon-Molecular Beam Epitaxy Vol. I" edited by E. Kasper and J.C. Bean, (CRC Press, USA, 1988), p. 181.

[88K] For a review of Si MBE see "Silicon-Molecular Beam Epitaxy Vol. I and Vol. II", edited by E. Kasper and J.C. Bean, (CRC Press, USA, 1988).

[88S] S. Satpathy, R.M. Martin, and C.G. Van de Walle, Phys. Rev. **B38**, 13237 (1988).

[88T] M.L.W. Thewalt and D.J.S. Beckett, Can. J. Phys. **66**, 868 (1988).

[87N] W.-X. Ni, J. Knall, and G.V. Hansson, Phys. Rev. **B36**, 7744 (1987).

[86B] G. Bastard and J.A. Brum, IEEE J. Electr. Devices **QE-22**, 1625 (1986).

[86G] D. Gershoni, E. Cohen and A. Ron, Phys. Rev. Lett. **56**, 2211 (1986).

[86S] T. Steiner, Ph.D. Thesis, Simon Fraser University, (1986).

[86Ta] H. Temkin, A. Antreasyan, N.A. Olsson, T.P. Pearsall, and J.C. Bean, Appl. Phys. Lett. **49**, 809 (1986).

[86Tb] M.L.W. Thewalt, A.G. Steele, S.P. Watkins, and E.C. Lightowlers, Phys. Rev. Lett. **57**, 1939 (1986).

[86V] C.G. Van de Walle and R.M. Martin, Phys. Rev. **B34**, 5621 (1986).

[85H] M.J. Howes and D.V. Morgan, eds, "Gallium Arsenide, Materials, Devices, and Circuits", (John Wiley and Sons Ltd., 1985).

[85L] P.V. Lang, R. People, J.C. Bean, and A.M. Sergent, Appl. Phys. Lett. **47**, 1333 (1985).

[85O] M. Oueslati, M. Zouaghi, M.E. Pistol, L.Samuelson, and H.G. Grimmeiss, Phys. Rev. **B32**, 8220 (1985).

[85Pa] R. People and J.C. Bean, Appl. Phys. Lett. **47**, 322 (1985).

[85Pb] R. People, J.C. Bean, and D.V. Lang, J. Vac. Sci. Technol. **A3**, 846 (1985).

[84L] Shui T. Lai and M.V. Klein, Phys. Rev. **B29**, 3217 (1984).

[84S] L. Samuelson and M-E. Pistol, Solid State Commun. **52**, 789 (1984).

[84T] M.L.W. Thewalt and W.G. McMullan, Phys. Rev. **B30**, 6232 (1984).

[83S] M.D. Sturge, E. Cohen, and R.A. Logan, Phys. Rev. **B27**, 2362 (1983).

[82C] E. Cohen and M.D. Sturge, Phys. Rev. **B25**, 3828 (1982).

[82M] G.S. Mitchard and T.C. McGill, Phys. Rev. **B25**, 5351 (1982).

[82P] S. Permogorov, A. Reznitskii, S. Verbin, G.O. Müller, P. Flogel, and, M. Nikiforova, Phys. Stat. Sol. **B113**, 589 (1982).

[82T] For a review of Si photoluminescence see M.L.W. Thewalt, in "Excitons", edited by E.I Rashba and M.D. Sturge (North-Holland, Amsterdam, 1982), p393.

[81R] A.K. Ramdas and S. Rodriguez, Rep. Prog. Phys. **44**, 1297 (1981).

[81S] S.M. Sze, "Physics of Semiconductor Devices", (John Wiley and Sons, USA) 1981.

[80H] R.B. Hammond and R.N. Silver, Appl. Phys. Lett. **36**, 68 (1980).

[78B] S.D. Barnovskii and A.L. Efros, Sov. Phys. Semicond. **12**, 1328, 1978.

[77K] G. Kirczenow, Solid State Comm. **21**,713 (1977).

[77R] T.M. Rice, Solid State Physics **32**, 1 (1977).

[74B] C. Benoit à la Guillaume and M. Voos, Phys. Rev. **B10**, 4995 (1974).

[74E] L. Esaki, Rev. Modern Phys. **46**, 237 (1974).

[74G] U. Gnutzmann and K. Clausecker, Appl. Phys. **3**, 9 (1974).

[73G] E.F. Gross, N.S. Sokolov, and A.N. Titkov, Sov. Phys.- Solid State **14**, 1732 (1973).

[69A] Zh.I. Alferov, E.L. Portnoi, and A.A. Rogachev, Soviet Physics - Semiconductors **2**, 1001 (1969).

[68B] A.S. Barker, in "Localized Excitations in Solids", edited by R.F. Wallis (Plenum, New York, 1968), p581.

[60H] J.R. Haynes, Phys. Rev. Lett. **4**, 361 (1960).

[58A] P.W. Anderson, Phys. Rev. **109**, 1492 (1958).

[55L] J.M. Luttinger and W. Kohn, Phys. Rev. **97**, 869 (1955).

[BM] Bomem Inc., Hartmann & Braun, 450 St.-Jean-Baptiste, Québec, Québec G2E 5S5.